Microkinetics Modeling of Automotive Three-Way Catalysts

by

Isabelle Pauwels

Submitted to the Department of Aeronautics and Astronautics
in partial fulfillment of the requirements for the degree of

Master of Science in Aeronautics and Astronautics

at the

MASSACHUSETTS INSTITUTE OF TECHNOLOGY
June 2003
May 2003

Author ....
Department of Aeronautics and Astronautics
May 16, 2003

Certified by. ....
Wai K. Cheng
Professor of Mechanical Engineering
Thesis Supervisor

Accepted by ....
Edward M. Greitzer
H.N. Slater Professor of Aeronautics and Astronautics
Chair, Committee on Graduate Students

Microkinetics Modeling of Automotive Three-Way Catalysts

by
Isabelle Pauwels

Submitted to the Department of Aeronautics and Astronautics
on May 16th, 2003 in partial fulfillment of the requirements
for the degree of Master of Science in Aeronautics and Astronautics

Abstract

This thesis reports the development of a one-dimensional fully transient microkinetics model for automotive monolithic three-way catalysts. The model was based on a comprehensive review of the catalyst to encompass the physical and chemical behaviors on the microscopic scale. In particular, the review explains the reactants attachment, the surface reactions, and the products desorption on the catalytic surface. It also details the role played by the catalytic support in the chemical processes.

The model accounts for the external and internal transport processes occurring inside non-adiabatic monoliths and for the detail of the reactions happening on the catalytic surface. It accounts for 7 chemical mechanisms -- the oxidation of CO, H_2, and C_3H_6, the reduction of NO by CO and H_2, the water-gas shift, and the steam reforming reactions. These mechanisms are represented by 22 elementary reactions. The model also includes an oxygen storage submodel, which comprises the oxidation of the ceria surface by oxygen and its reduction by carbon monoxide.

The main part of this work consisted of determining the elementary reactions to represent the catalyst activity, and of assembling the corresponding kinetic parameters from a combination of literature data, transition state estimations, and thermodynamic calculations. The comparison of the assembled chemical network with previously determined global rate expressions showed the ability of our model to represent the chemical activity of the catalytic converter. It also illustrated the necessity for a detailed chemical modeling to predict the behavior of the catalyst on its whole range of operating temperatures.

Thesis supervisor: Wai K. Cheng
Title: Professor, Department of Mechanical Engineering

Acknowledgements

First, I would like to thank my advisor, Professor Wai K. Cheng, for his ongoing support and guidance throughout the project. I consider myself extremely fortunate to have had Wai as my supervisor during my time here at MIT. He trusted me with the project and has always been approachable and willing to give up his time to help me deal with the various problems encountered along the way. Moreover, he taught me valuable modeling methods that will always be useful to me.

Further thanks are due to the members of the Engine and Fuels Research Consortium who have funded this project: DaimlerChrysler Corp., Ford Motor Co., General Motors Corp., Exxon Mobil Corporation, Volvo Car Corp., and Delphi Corp.

I would also like to thank my colleagues at the Sloan Lab for their help, but above all for making my time here enjoyable: Fiona McClure, Brian Hallgren, and GJ Lao.

Finally, I am very grateful to my boyfriend and my family for their continued encouragement and support.

Table of Contents

Abstract 3

Acknowledgements 4

Table of Contents 5

List of Figures 8

List of Tables 12

Nomenclature 13

1 Introduction 17

1.1 Background 17
1.2 Motivation and scope 20
  1.2.1 Previous work 20
  1.2.2 Limitations of the previous models 21
  1.2.3 Scope of this thesis 22
1.3 Organization of the thesis 22

2 Design of monolithic three-way catalytic converters 23

2.1 The monolith TWCC 23
  2.1.1 General aspect 23
  2.1.2 Performance of TWCC 24
2.2 Structural elements 27
  2.2.1 The substrate 28
  2.2.2 The washcoat 31
  2.2.3 The catalytic particles 36
2.3 Making the finished catalyst 41
  2.3.1 Depositing the uncatalyzed washcoat on the monolith substrate 41
  2.3.2 Dispersing the noble metals on the coated monolith 42
  2.3.3 Constraints 44

3 **Physical insight into the catalytic process in three-way catalytic converters** **45**
3.1 Overview of the catalytic action.......... 45
3.1.1 Initiating the reaction.......... 45
3.1.2 Stabilizing the intermediates.......... 46
3.1.3 Holding the reactants in close proximity.......... 47
3.1.4 Stretching the bonds.......... 47
3.2 Heterogeneous catalysis in catalytic converters.......... 47
3.2.1 Adsorption.......... 48
3.2.2 Surface reactions.......... 54
3.2.3 Desorption.......... 59
3.3 Enhancements and inhibitions of the catalytic activity in TWCC.......... 60
3.3.1 Enhancement by metals-washcoat components interactions.......... 60
3.3.2 Aging.......... 63

4 **Modeling of the monolithic catalyst** **69**
4.1 Main features of the model.......... 69
4.1.1 Assumptions.......... 69
4.1.2 Modeled processes.......... 71
4.2 Limiting processes.......... 72
4.3 Transport modeling.......... 79
4.3.1 Internal transport.......... 79
4.3.2 External transport.......... 84
4.4 Catalytic reactions.......... 94
4.4.1 Included species and chemical mechanisms.......... 94
4.4.2 Determination of the elementary steps in each mechanism.......... 95
4.4.3 Rate expressions.......... 103
4.4.4 Kinetic constants determination.......... 104
4.5 Oxygen storage process.......... 139
4.5.1 Modeling approach.......... 139
4.5.2 Kinetic constants.......... 140

5 Physical understanding of converters chemical processes 153

5.1 The chemical limiting process 153

5.2 Similar chemical behavior of the $CO-O_2$ and H_2-O_2 mechanisms 156

5.3 H_2-O_2 mechanism 158

6 Conclusions and future work 161

6.1 Conclusions 161

6.2 Future work 162

6.2.1 Model validation 162

6.2.2 Further improvements to the model 162

Bibliography 165

A Computation of the characteristic times of the transport and chemical processes for CO oxidation 171

A.1 External transport 171

A.2 Internal transport 171

A.2.1 Effective diffusivity 171

A.2.2 Time calculations 172

A.3 Catalytic reactions 174

A.3.1 Characteristic time for the adsorption of O_2 174

A.3.2 Time scale for the CO*-O* surface reaction 175

List of Figures

Fig. 1.1 Typical composition of the exhaust gas of a gasoline-powered SI internal combustion engine 18

Fig. 2.1 Monolithic converter 23

Fig. 2.2 Monolithic reactors 24

Fig. 2.3 Evolution of the CO, HC, and NOx conversion efficiencies with λ [14] 25

Fig. 2.4 The closed-loop control system 26

Fig. 2.5 Structure of a coated monolithic catalyst 27

Fig. 2.6 Monolithic supports [12]: (a) Extruded ceramic with triangular channels; (b) Extruded ceramic with square channels 28

Fig. 2.7 Design principle of a ceramic monolith based converter 30

Fig. 2.8 Closed-up view of a metallic monolithic substrate [11] 31

Fig. 2.9 Ceramic monolith coated with a catalyzed washcoat [12] 32

Fig. 2.10 Scanning Electron Microscope view of a washcoat layer [11] 33

Fig. 2.11 World supply of platinum, palladium, and rhodium (a) and share of its use in automotive catalysts (b) [11] 37

Fig. 2.12 Transmission Electron Micrograph of platinum crystallites on a γ-Al_2O_3 carrier 39

Fig. 2.13 Cluster of Pt atoms 39

Fig. 2.14 Segregated cluster of Pt and Rh atoms 40

Fig. 2.15 Double coat automotive catalyst [12] 44

Fig. 3.1 Potential energy diagram for the oxidation of CO at 800 K: (a) Homogeneous reaction; (b) Pt-catalyzed reaction 46

Fig. 3.2 Potential energy curve for the adsorption process [18] 48

Fig. 3.3 Dissociative adsorption of H_2 on platinum 51

Fig. 3.4 Four adsorbing configurations of CO [19] 52

Fig. 3.5 Alteration of the surface segregation by selective adsorption: (a) Surface before adsorption; (b) effect of adsorption 53

Fig. 3.6 Definition of the spillover phenomenon... 56

Fig. 3.7 Oxygen storage process... 58

Fig. 3.8 Comparison of the Temperature Programmed Reduction for several catalyst compositions: (a) γ-Al_2O_3; (b) Pt, Rh/ γ-Al_2O_3; (c) 6 wt % Ce/ γ-Al_2O_3; (d) Pt, Rh, 6 wt % Ce/ γ-Al_2O_3 (Pt loading=0.77 wt %; Rh loading=0.04 wt %).... 61

Fig. 3.9 Modes of ceria-noble metal interaction in the synergistic reduction of the surface: (a) Direct interaction; (b) Interaction through spillover...................62

Fig. 4.1 Flow representation in the modeled monolith channel.................................70

Fig. 4.2 Transport processes occurring in the monolith channels: (a) External transport; (b) Internal transport..71

Fig. 4.3 Possible kinetic regimes in a gas phase reaction occurring on a porous solid catalyst.. 72

Fig. 4.4 Concentration of an adsorbing reactant as a function of time...................... 75

Fig. 4.5 Characteristic times of O_2 adsorption and CO*-O* surface reaction versus temperature.. 77

Fig. 4.6 Characteristic times of the chemical and transport processes versus temperature.. 78

Fig. 4.7 Non-uniform concentration profile inside a pore under internal transport limitation..80

Fig. 4.8 Internal transport modeling principle..81

Fig. 4.9 Effectiveness factor versus solid temperature for the oxidations of propane and carbon monoxide...83

Fig. 4.10 Mass transport fluxes on a slice of monolith... 86

Fig. 4.11 Definition of the volumes and areas involved in the mass transport equations.. 88

Fig. 4.12 Energy transport fluxes on a slice of monolith..90

Fig. 4.13 Transition state theory estimates of pre-exponential factors [56].................109

Fig. 4.14 Variation of O_2 sticking coefficient with the surface temperature for: (a) Campbell's fitting model [46]; (b) Adaptation of Campbell's model to our model...112

Fig. 4.15 Batch reactor used in the chemical simulation.. 130

Fig. 4.16 (a) Evolution of the characteristic time with temperature for the global and detailed mechanisms (redox=0.786); (b) same on an expanded scale........... 132

Fig. 4.17 Evolution of the CO_2 concentration with time in the CO-O_2 mechanism for T=975 K and redox=0.786 133

Fig. 4.18 Evolution of the CO_2 concentration with time in the CO-O_2 mechanism for different redox ratios near stoichiometry (T=975 K) 134

Fig. 4.19 Evolution of the CO_2 concentration with time in the CO-O_2 mechanism for different redox ratios in the lean region (T=975 K) 135

Fig. 4.20 Evolution of the H_2O concentration with time in the H_2-O_2 mechanism at 840 K 136

Fig. 4.21 Evolution of the CO_2 concentration with time in the C_3H_6-O_2 mechanism (T=880 K, E_{Af3}=0 kJ/mol, E_{Ar3}=120 kJ/mol) 137

Fig. 4.22 Evolution of the CO_2 concentration with time in the C_3H_6-O_2 mechanism (T=880 K, E_{Af3}=0 kJ/mol, E_{Ar3}=40 kJ/mol) 138

Fig. 4.23 Evolution of the concentration of available storage sites with time for *Koltsakis et al*'s and the microkinetics ceria reduction at 850 K 144

Fig. 4.24 Evolution of the concentration of available storage sites with time for *Koltsakis et al*'s and the microkinetics ceria reduction at 500 K 145

Fig. 4.25 Relative importance of reactions 25 and 26 on the reduction of ceria at 850 K 146

Fig. 4.26 Evolution of the concentration of stored oxygen atoms with time at 800 K with $A_{23}=A_{25}$ and $A_{24}=5.10^6\ Pa^{-1}.s^{-1}$ 148

Fig. 4.27 Comparison of the oxidation and reduction rates of ceria at 770 K 149

Fig. 4.28 Evolution of the concentration of stored oxygen atoms with time at 600 K 150

Fig. 4.29 Relative importance of reactions 23 and 24 on the oxidation of ceria at 800 K 151

Fig. 5.1 CO_2 production and adsorbate coverages in the CO-O_2 reaction at 450 K... 154

Fig. 5.2 CO_2 production and adsorbate coverages in the CO-O_2 reaction at 900 K... 155

Fig. 5.3 Evolution of the CO_2 and H_2O concentrations with time in the CO-O_2 and H_2-O_2 mechanisms for two CO and H_2 levels: 1.1% and 0.55% (T=900 K)...... 157

Fig. 5.4 Evolution of the H_2O concentration and surface coverages with time in the H_2-O_2 mechanism at 840 K (H_2 level=0.37 %) 158

Fig. 5.5 Evolution of the H_2O concentration and surface coverages with time in the H_2-O_2 mechanism at 840 K with modified E_{Af16} (H_2 level=0.37%) 159

Fig. A.1 Assumed typical bimodal pore distribution........ 173

List of Tables

Table 1.1 Required automotive emission standards for 2004 (SULEV).................. 19

Table 3.1 Change in monohydrate alumina crystals as a function of temperature..... 64

Table 4.1 Time scales of the elementary steps in the CO-O_2 mechanism................. 77

Table 4.2 Time scales of the transport and chemical processes.................................78

Table 4.3 List of the elementary reactions included in the model............................. 102

Table 4.4 Enthalpies and free energies (chemical plus sensible) of the gaseous species at 800 K...114

Table 4.5 Mechanism for the CO-O_2 reaction.. 115

Table 4.6 Mechanism for the H_2-O_2 reaction...115

Table 4.7 Mechanism for the NO-CO reaction..116

Table 4.8 Mechanism for the NO-H_2 reaction.. 117

Table 4.9 Mechanism for the water-gas shift reaction..119

Table 4.10 Mechanism for the C_3H_6-O_2 reaction...121

Table 4.11 Mechanism for the steam reforming reaction... 123

Table 4.12 Kinetic parameters of the considered elementary reactions...................... 124

Table A.1 Characteristic times of the transport and chemical processes at different temperatures...176

Nomenclature

Variables

A	channel cross-section in m^2
A_{ap}	apparent surface area of the washcoat in m^2
A_{ext}	effective area of convective exchange with the ambient between positions in m^2
A_j	preexponential factor of reaction j
A_j'	groups the preexponential factor and the temperature dependence of k_j
a_m	internal surface area per unit monolith volume in m^{-1}
A^*	internal surface area between positions in m^2
BET_{ceria}	ceria surface area in m^2/kg
[i]	molar concentration of species i in mol/m^3 for gaseous species and mol/m^2 for adsorbed species
c_i	molar concentration of species i in mol/m^3 for gaseous species and mol/m^2 for adsorbed species
$\tilde{c}_i$	concentration of adsorbed species i in mol/m^2 catalytic area
$\tilde{c}_{s_0}$	total concentration of catalytic sites in mol/m^2 catalytic area
Cp	heat capacity in J/kg.K
d	channel diameter in m
d_h	hydraulic diameter in m
D	diffusion coefficient of species in m^2/s
Disp	noble metal dispersion
d_p	pore diameter in m
E_{Aj}	activation energy of reaction j in J/mol
ΔG	free energy change in J/mol
ΔH	heat of reaction in J/mol
h	massic enthalpy in J/kg
h_{amb}	external heat transfer coefficient in $J/m^2.K.s$
h_{gw}	internal convective heat transfer coefficient in $J/m^2.K.s$

h_P	Planck constant $h_P=6.626.10^{-34}$ J.s
I_0	noble metal perimeter in m/m^2
k_B	Boltzmann constant: $k_B = 1.38.10^{-23}$ J/K
k_g	mass transfer coefficient or mass transfer surface velocity in m/s
k_j	kinetic rate constant of reaction j
l	pore length in m
L	monolith length in m
M	molecular weight
$\dot{m}$	mass flow rate in kg/s
MFP	mean free path in m
n	number of monolith cells
N_A	Avogadro's number $N_A=6.02.10^{23}$
N_{s0}	number of catalytic sites per m^2 internal surface area
OSC	oxygen storage capacity or total concentration of atomic oxygen storage sites
P	pressure in Pa
P_0	standard pressure in Pa
q_i	molecular partition function of species i
R_g	universal gas constant in J/mol.K
R_j	rate of reaction j in $mol/m^2.s$
s_o	initial sticking coefficient
S	gas-solid interface area per unit volume in m^{-1}
S_{amb}	surface area of external convective exchange per unit monolith volume in m^{-1}
S_{ext}	monolith external peripheral area in m^2
$[S]_0$	total concentration of catalytic sites in mol/m^2
T	temperature in K
T_0	standard temperature in K
v	flow velocity in m/s
V	monolith volume in m^3
V'	washcoat volume in m^3
V^*	void volume in m^3
x_i	mole fraction of species i

x_{Pt}	noble metal loading

Greek letters

β_j	temperature dependence of k_j
ε	monolith void fraction or percentage open frontal area
ε_w	washcoat porosity
η	effectiveness factor
θ_i^*	partial coverage of adsorbate species i
λ	air-equivalence ratio
λ	heat conductivity in W/m.K
ρ	density in kg/m^3
σ	adsorption area per site in m^2
σ_j	stoichiometric number of reaction j
τ	characteristic time in s
τ	tortuosity factor
ψ	extent of oxidation of ceria or auxiliary number
ω	vibration frequency in cm^{-1}

Chemical representations

S	available catalytic site
< >	oxygen vacancy on ceria
<O>	stored oxygen atom on ceria

Dimensionless groups

Le	Lewis number $Le = \frac{\lambda_g}{\rho_g . Cp_g . D_i}$
Nu	Nusselt number $Nu = \frac{h_{gw} . D_h}{\lambda_g}$
Pe	Peclet number $Pe = \frac{v.L}{D_i}$

Sh	Sherwood number $Sh = \frac{k_g . D_h}{D_i}$

Subscripts and superscripts

amb	ambient
eff	effective
f	forward
g	exhaust gas
m	molecular
net	global reaction
ox	oxidation
r	reverse
red	reduction
s	solid
*	adsorbate

Operators

∇	gradient

Abbreviations

A/F	Air-fuel ratio
HC	Hydrocarbons
PGM	Platinum group metal
SI	Spark-ignition
SULEV	Super ultra-low emission vehicle
TWCC	Three-way catalytic converter

Chapter 1: Introduction

1.1 Background

Nowadays, automobiles constitute one of the major causes of environmental pollution. Spark-ignition (SI) engines are responsible for the release of five main types of exhaust pollutants:

- *Carbon monoxide (CO)*

  Carbon monoxide forms as a result of incomplete combustion of the fuel and the oxygen in the air. Its emission is more severe under fuel rich conditions.

- *Hydrocarbons (HC)*

  Emitted hydrocarbons are products of incomplete combustion or fuel that escapes the combustion process in the engine. Major mechanisms for their formation are the absorption and desorption of fuel in the oil layers and the storage and release of the fuel-air mixture in the crevices of the cylinder. We distinguish three types of emitted hydrocarbons in engine-out emissions: unsaturated HC such as propylene C_3H_6, saturated HC such as propane C_3H_8, and methane CH_4 and aromatics such as toluene. Because CH_4 does not interact with the atmosphere to form smog, it is often excluded in the measurement of exhaust HC (then the HC are referred to as the Non-Methane Hydrocarbons, NMHC). However, CH_4 is a strong IR absorber, so it is a significant component of the greenhouse gases.

- *Nitric oxides NOx (NO and NO_2)*

  The high temperatures encountered in combustion flames promote the formation of NOx via the oxidation of N_2 by O_2.

- *Sulfur compounds: SO_2, SO_3, H_2S*

  These emissions originate from the sulfur in the fuel.

- *Greenhouse gases: CO_2, CH_4, and N_2O*

CO_2 is one of the main emissions of automotive engines, being a major product of complete combustion. N_2O originates like NOx from the oxidation of N_2, and is usually present in very small amounts.

A typical SI engine shows the following engine-out emissions:

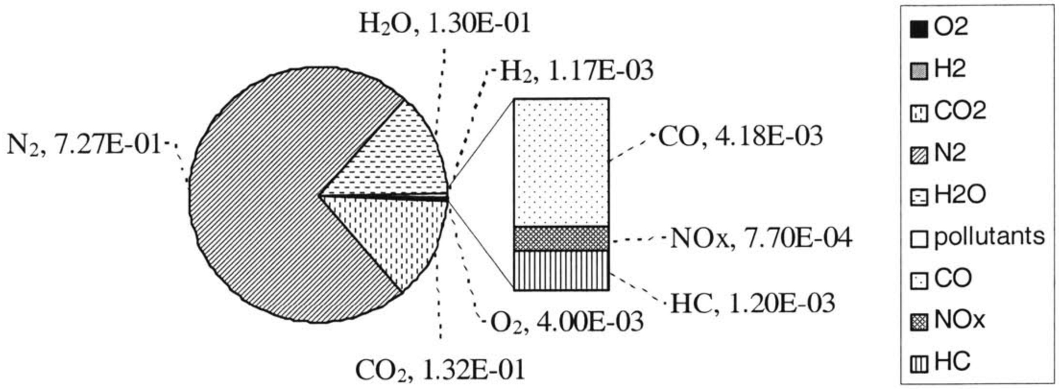

Fig. 1.1: *Typical composition of the exhaust gas of a gasoline-powered SI internal combustion engine (the numbers on the figure are mole fractions)*

These proportions depend on the air-fuel ratio of the engine: rich operation leads to more formation of CO and HC, whereas lean operation decreases their amount and increases the amount of O_2 in the exhaust. Modern engines moderate the air-fuel ratio from stoichiometry so that the air equivalence ratio $(\lambda)^1$ is $1 \pm \delta$ where δ is in the range of 0.005 to 0.02. Then, there is significant engine out CO when $\lambda<1$, and significant engine out O_2 when $\lambda>1$. The excess CO is oxidized by the O_2 stored in the catalyst.

The emissions CO, HC, and NOx are considered as harmful and are regulated. Indeed, CO is poisonous to human even in low concentrations; many HC are carcinogenic; and NOx contribute to acid rains, which damage forests and plants, and cause irritation to human. NOx and HC also undergo photochemical reactions that produce ozone and smog, which are unhealthy to human.

---

[1] The air equivalence ratio λ is defined by $\lambda = \frac{actual\ engine\ A/F}{stoichiometric\ engine\ A/F}$

In the United States, regulations were introduced in 1970 by the first Clean Air Act for CO and HC emissions, and in 1975 for NOx emissions. Since then, the reduction of automotive emissions has become a worldwide movement, and the emission standards have been drastically reduced. Thus, the California Air Resources Board regulations for new 2004 and subsequent SULEV models are:

Table 1.1: *Required automotive emission standards for 2004 (SULEV)*

	Non-methane HC	**CO**	**NOx**
Emissions in g/mile	0.01 *down from 0.41 in 1991*	1 *down from 3.4 in 1991*	0.02 *down from 1 in 1991*

Catalytic converters have been used since 1974 in the United States to reduce the harmful emissions. Between 1974 and 1979, oxidation catalysts were developed to convert HC and CO. Then, to answer the new regulation on NOx emissions, two new types of catalysts were commercialized:

- The dual bed catalyst made of two different types of catalysts: the first one is a reducing catalyst able to promote NOx reduction reactions, and the second one is an oxidation catalyst
- The three-way catalytic converter (TWCC) able to reduce the three regulated emissions simultaneously

Monolithic TWCC constitute nowadays the most widespread type of catalytic converter. They remove more than 90% of CO, HC, and NOx emissions near stoichiometry.

1.2 Motivation and scope

The objective of this thesis is to develop a fundamentally based kinetics and transport model for modern three-way catalytic converters (TWCC) with oxygen storage.

1.2.1 Previous work

Mathematical modeling of monolithic catalysts has been employed over the last thirty years to assist the design and development of automotive exhaust aftertreatment systems.

In the seventies and eighties, models of oxidation catalysts were developed and mostly applied to design-oriented studies. Thus, *Otto and LeGray* [1] studied the effect of converter properties and feed gas effects on the conversion efficiency of oxidation catalysts with a one-dimensional model. *Oh and Cavendish* [2] also developed a one-dimensional model; they performed a parametric analysis of light-off performance and studied the catalyst thermal response to a step decrease in exhaust temperature. The previous models consider adiabatic monoliths exposed to a uniform flow distribution at the front face. In fact, the flow distribution at the catalyst inlet is not uniform. *Chen et al* [3] accounted for this non-uniformity by extending *Oh et al*'s model to non-adiabatic monoliths and non-uniform flow distributions. They indeed developed a three-dimensional model for the analysis of thermal transients during warm-up, sustained heavy load, and engine misfiring.

The above oxidation catalysts models rely heavily on the kinetic expressions of *Voltz et al* [4]. These expressions account for the inhibition of CO, NO, and C_3H_6 on the oxidation of CO, H_2, and HC. In fact, most models kept the form of *Voltz*'s kinetic expressions and tuned the coefficients experimentally to their own case, thus lumping all elementary processes occurring close to the surface into one single expression.

The modeling of three-way catalytic converters began in the nineties. Unlike oxidation catalysts models, TWCC models have to account for the catalytic reactions close to stoichiometry and not just in lean environment. Moreover, they must include more chemical mechanisms and thus require the gathering of more chemical information. Gathering this kinetic information constitutes the most difficult part in TWCC modeling.

TWCC models can be classified according to two criteria: the number of catalytic reactions they include and the way they reproduce the transient operation of the monolithic catalyst. The review by *Shamim et al* [5] shows how these two factors affect the simulation of the converter's performance.

Regarding the chemistry, *Montreuil et al* [6] present so far the most inclusive scheme with 13 reactions. *Pattas, Stamatelos, Koltsakis et al* [7] developed a one-dimensional model accounting for the oxidations of CO, H_2, the two types of hydrocarbons C_3H_6 and C_3H_8, and NO reduction by CO. *Brinkmeir, Eigenberger et al* [8] added the reduction of NO by H_2 and HC and the water-gas-shift reaction. The two models, and the further refinement to a two-dimensional model by *Koltsakis et al* [9], reproduce the transient behavior of the catalyst by accounting for the catalyst oxygen storage. As demonstrated in [5], this oxygen storage capacity of the catalyst is mostly responsible for its good transient performance.

Not only did the complexity of the modeling increase, but the purpose of the simulations also shifted in the later work. Indeed, TWCC models aim at understanding the physical behavior of the catalyst apart from their application for catalyst design. For instance, *Pattas, Stamatelos, Koltsakis et al* [7] investigated the effect of aging on the performance of the catalytic converter, whereas *Brinkmeier, Eigenberger et al* [8] focused on the transient behavior of the catalyst, especially on its oxygen storage capacity.

1.2.2 Limitations of the previous models

All the above models correctly characterize the overall time averaged performance of catalytic converters. However, none of them captures and characterizes the detailed processes responsible for their behavior. In particular, they do not go into the details of the chemistry; they consider global chemical mechanisms by lumping all the detailed elementary reactions into one expression (see [5]) and match experimental data empirically by adjustment of a global rate.

Sriramulu et al [10] show the path towards a more detailed modeling of TWCC: they propose a microkinetics-based model that describes the reactions taking place on the surface of a catalytic converter. Microkinetics models have the ability to simulate the catalyst unsteady behavior, and thus the performance of TWCC, since the catalyst is never operated at steady state. Also, the effects of changing the catalyst parameters such as the noble metal loading level and the oxygen storage capacity can be examined.

The *Sriramulu et al* work did not consider another important process: the transport of species to the active sites of the catalyst. Indeed, they claimed that the transport processes did not change their chemical simulations, which should not be true for all temperatures. Moreover, their assumptions in establishing the set of elementary reactions did not always agree with physical observations. They also considered only one species of hydrocarbons.

1.2.3 Scope of this thesis

This project aims at developing a detailed model that includes all the important phenomena involved in the TWCC behavior. The model is capable of simulating transient operation. It considers: details of the surface catalytic reactions, transport of species to the wall of the catalyst, and oxygen storage. By including all these processes in the model, we intend to study the relative importance of each of them on the catalyst activity.

1.3 Organization of the thesis

We first reviewed the elements and working principles of TWCC. This review aims at drawing a representative microscopic picture of the surface of an operating catalyst. Chapters 2 and 3 report this review.

Based on this physical understanding, a fully-transient one-dimensional model of the catalyst was developed. This model uses microkinetics methods as in [10] to describe the chemical reactions on the catalytic surface; it includes a representative set of 22 elementary reactions. It also accounts for the external and internal diffusion inside the monolith as well as its oxygen storage capacity. In Chapter 4, the catalyst model is presented with a table of kinetic data for the elementary reactions considered. Chapter 5 discusses some trends of the chemical behavior of the catalytic surface.

Chapter 6 presents the conclusions of this thesis and gives perspectives for future work.

Chapter 2: Design of monolithic three-way catalytic converters

This chapter reviews the main physical characteristics of TWCC, and their main constituents. The material covered in this chapter is based on the work of *Ertl et al* [11], *Heck and Farrauto* [12], and *Cybulski and Moulijn* [13].

2.1 The monolith TWCC

2.1.1 General aspect

Figure 2.1 shows a typical catalytic converter, ready to be integrated to the engine. The system consists of the following parts:

1) The entrance piping linking the catalytic converter to the engine
2) A diffuser to expand the flow uniformly across the face of the catalytic reactor
3) The catalytic reactor itself, the monolith
4) The exit nozzle
5) The exit pipe

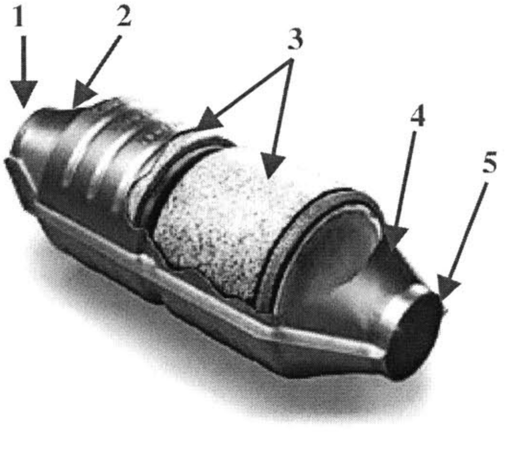

Fig. 2.1: *Monolithic converter*

Monolithic reactors are cylinders comprising a multitude of parallel channels on the walls of which the catalyst active materials are deposited, as illustrated on Figure 2.2. Their different components will be detailed in section 2.2.

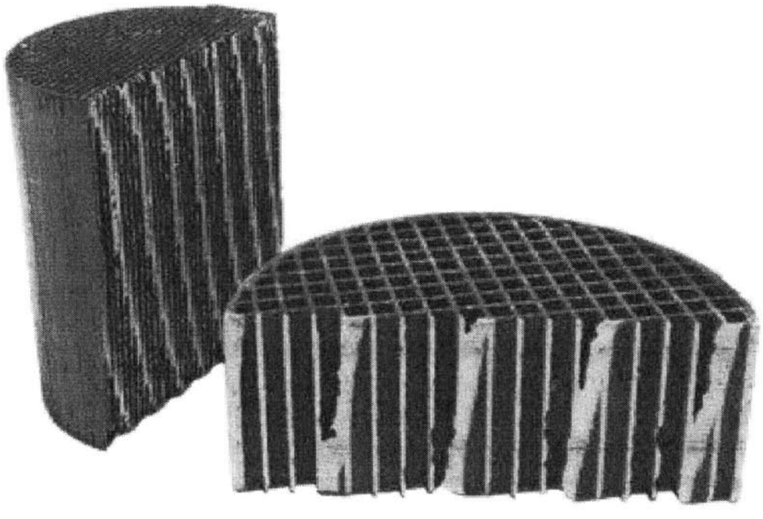

Fig. 2.2: *Monolithic reactors*

Monoliths are light, compact, cheap, and easy-to-build. They also offer a small resistance to the passage of the flow resulting in a low pressure drop. These advantages have made them the only type of catalytic reactor in use since the mid-seventies, displacing the packed-bed reactors[1].

2.1.2 Performance of TWCC

The three-way catalytic converters simultaneously reduce the three main types of harmful emissions -- CO, hydrocarbons (HC), and NOx. As mentioned in Chapter 1, the levels of engine-out emissions depend on the air-fuel ratio of the engine. Figure 2.3 shows that the performance of a TWCC also depends on this air-fuel ratio[2]. For instance, the CO conversion efficiency increases from 20% to 100% between $\lambda=0.98$ and $\lambda=1$. Moreover, the appropriate air-fuel ratio for high conversion depends on the considered species. Thus, CO and HC are easily and almost completely converted under lean operation, where the exhaust contains oxygen in sufficient amount to oxidize them, whereas NOx is better reduced under rich operation where enough CO and HC subsist in

---

[1] In packed-bed reactors, the catalyst is deposited on pellets

[2] The abscissa variable on Figure 2.3 is not the air-fuel ratio A/F but the air equivalence ratio λ (see note 1 p. 18)

the exhaust for its reduction. Hence, TWCC can achieve high conversions of the three pollutants in a narrow window near stoichiometry.

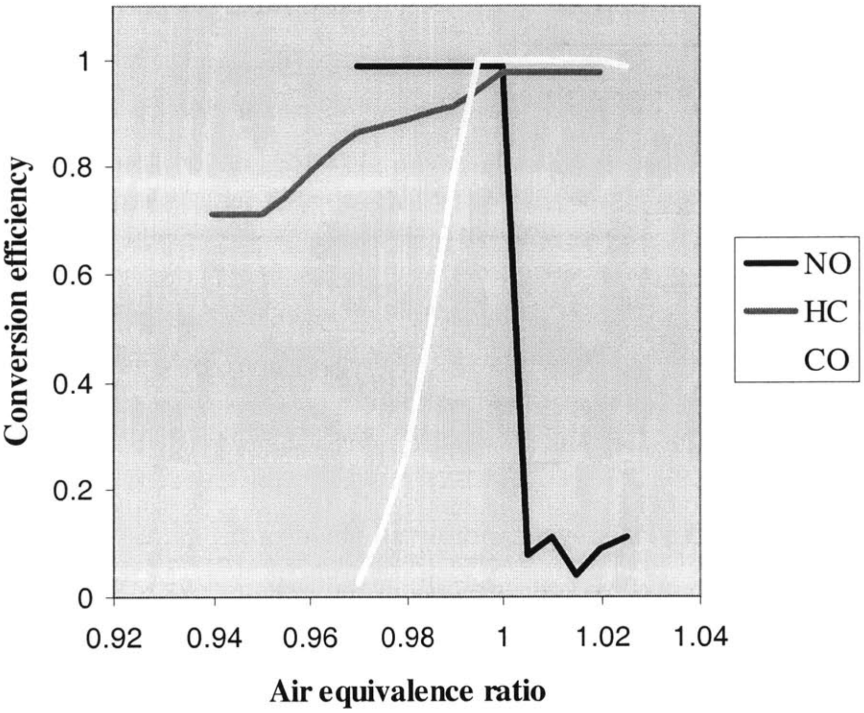

Fig. 2.3: *Evolution of the CO, HC, and NOx conversion efficiencies with* λ [14]

To maintain efficient catalytic operation, TWCC are combined with a control system as illustrated on Figure 2.4. The package of the converter plus the control system is called a closed-loop TWCC. Since it is practically difficult to keep λ precisely at 1 (within the narrow window of simultaneous high conversion efficiency), the closed-loop TWCC makes use of the oxygen storage capacity of the catalyst and modulates the A/F around stoichiometry. It uses a sensor feed-back system to maintain a time averaged λ of 1.

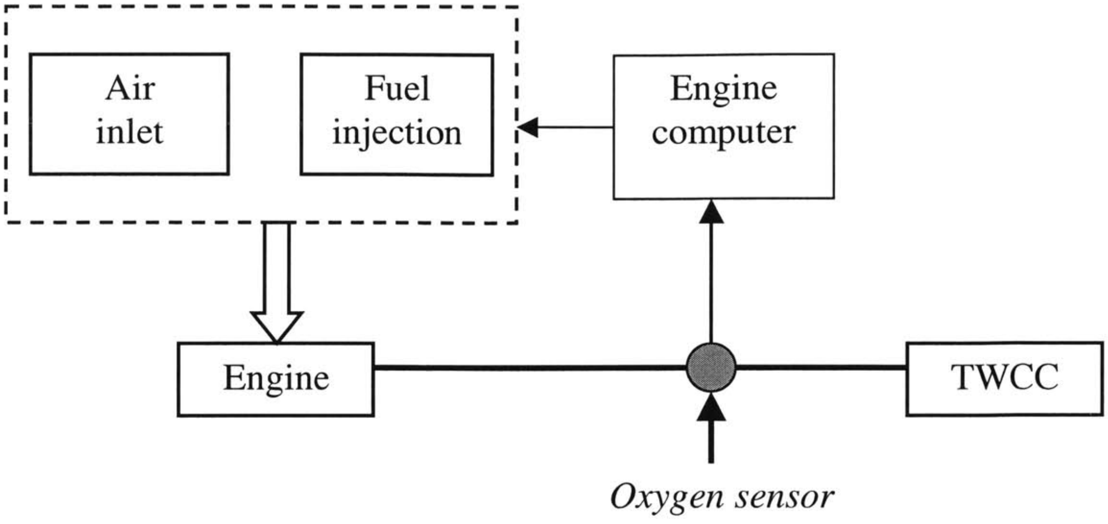

Fig. 2.4: *The closed-loop control system*

The control system includes an oxygen sensor mounted upstream of the converter inlet which measures the amount of oxygen present in the exhaust. This information is then sent to the engine computer which adjusts the air-fuel ratio so that, on the average, the A/F is stoichiometric. This control results in a periodic A/F signal. A typical lambda signal oscillates between λ=0.975 and λ=1.025, with a frequency of the order of 1-2 Hz.

The oxygen storage feature works as follows. Under lean operation, the oxygen storage components remove and store the excess oxygen present in the exhaust so that there is no excess O_2 to compete for the NOx reduction process. Under rich operation, the stored oxygen is released to oxidize the CO and HC. We will talk in more details about these oxygen storage components in section 2.2.2.

To summarize, the presence of both the control system and the oxygen storage components is responsible for overall conversion efficiencies between 97% and 100%.

2.2 Structural elements

As represented on Figure 2.5 below, a monolithic catalyst consists of three parts:

- The substrate, also commonly referred to as the monolithic structure or monolith
- The uncatalyzed washcoat or carrier –which will be simply called the washcoat in the next sections--, and
- The catalytic species

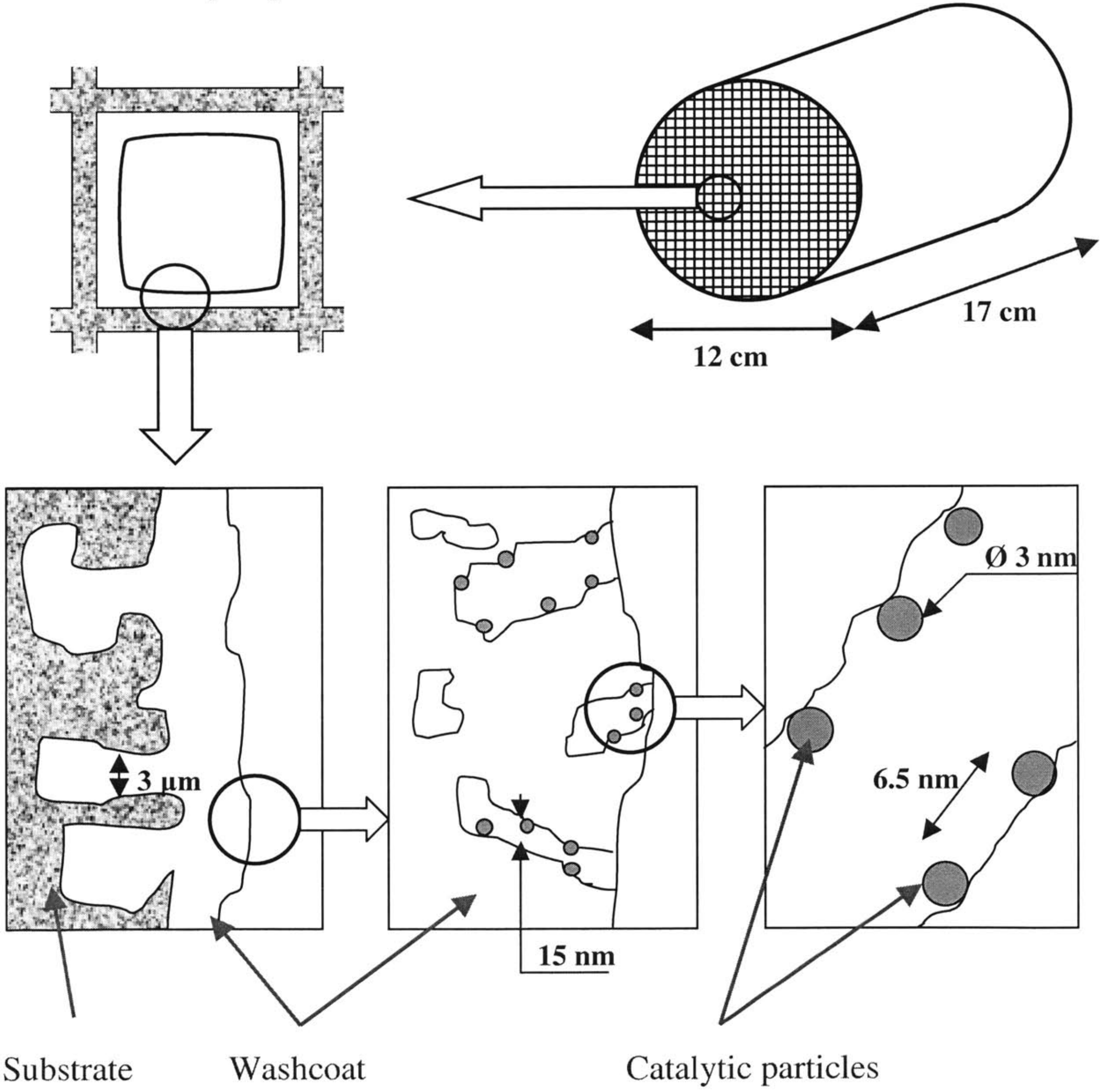

Fig. 2.5: *Structure of a coated monolithic catalyst*
(The dimensions given on the figure are not to scale, they are typical numbers)

The following sections present the main characteristics of each of these elements.

2.2.1 The substrate

As already said, the monolithic substrate consists of a cylindrical unit, most commonly of a circular or oval-like shape, in the structure of a honeycomb with equally sized and parallel channels. The channels may be square, sinusoidal, triangular, hexagonal, or round (see Figures 2.6(a) and 2.6(b)). Their reproducibility in size, but also in surface characteristics along the monolith, reduces the flow non-uniformity across the monolith.

Monolithic substrates for automotive applications show low internal surface areas from 0.1 to 2 m^2/g.

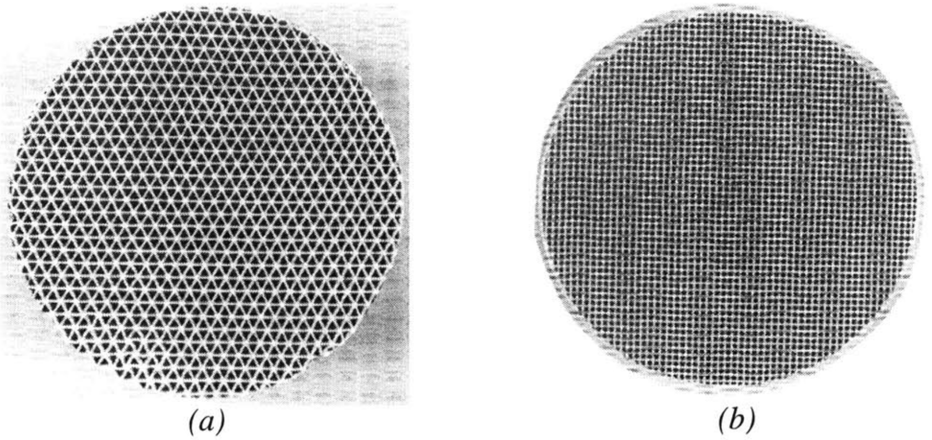
(a) *(b)*

Fig. 2.6: *Monolithic supports* [12]
(a) Extruded ceramic with triangular channels; (b) Extruded ceramic with square channels

Monoliths can be classified based upon two criteria:

- their structure: the walls between the channels can be impermeable or permeable (membrane reactors). The latter configuration loses the advantage of low pressure drop and flow uniformity, and is thus not of much use.
- their composition: the substrate can be made out of ceramic materials or metals. These two types of monoliths are described in the following paragraphs.

i- Ceramic substrates

The most common ceramic monoliths are made out of cordierite ($2MgO$-$2Al_2O_3$-$5SiO_2$) with small amounts of Na_2O, Fe_2O_3, and CaO. Indeed, cordierite shows all the important characteristics required for a substrate:

- Thermal shock resistance: when operated over a wide temperature range, cordierite experiences little dimensional change due to its low thermal expansion coefficient. It thus resists cracking due to thermal shock.
- Mechanical strength
- High melting point compared to catalytic converters highest temperatures ($T_{melting}$ = 1300 C), which guaranties its structural resistance to the harsh automotive environments.

Ceramic monoliths are manufactured by extrusion of a paste containing the cordierite precursors together with processing aids. The extrusion is then followed by drying and calcination.

Their incorporation into the converter system requires the use of several protecting layers, as illustrated on Figure 2.7. The overall ceramic-based converter thus consists of three parts:

- The monolithic ceramic support
- A mat, which surrounds the support, made either out of ceramic material or out of a metallic wire mesh. This mat protects the ceramic monolith against mechanical impact, and also serves as a thermal insulation.
- A converter housing made out of corrosion-resistant steel. This piece is inserted into the exhaust pipe and links the converter to the engine and to the rest of the aftertreatment system.

The converter can be packed with a single, two, or sometimes three single pieces of ceramic monoliths. If multiple pieces are used, they are mounted with well-defined distance between them, so that the wakes of one monolith mix out before the flow goes into another section.

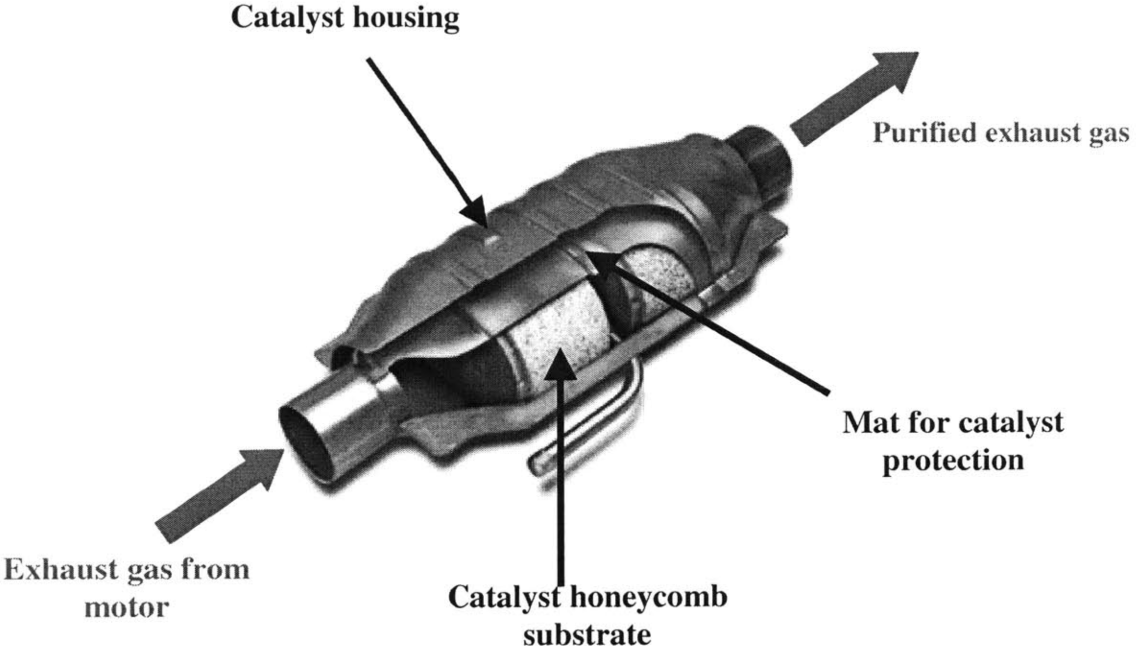

Fig. 2.7: *Design principle of a ceramic monolith based converter*

Ceramic monoliths with sizes up to 18 cm in diameter and 28 cm long have been built. Their cell density ranges from 9 to 1200 cells per square inch (cpsi). A typical ceramic monolith is about 17 cm long, 12 cm in diameter, includes 400 cpsi with channels of about 1 mm wide, a wall thickness of about 0.15 mm for square channels, and an approximate open frontal area of 70%.

Ceramic substrates used for automotive applications present 20 to 40% porosity. Their average pore size is about 3-4 μm, but the size range is wide, and pores as large as 15 μm exist. As will be explained later, these large pores help for good adhesion of the washcoat on the substrate.

ii- Metallic substrates

Metallic monoliths are most commonly made out of high temperature and corrosion-resistant aluminum-containing steel, for instance steel alloys such as Kanthal (5.5% Al, 22% Cr, 0.5% Co). They consist of alternate flat and corrugated thin metal foils, and most often include sinusoidal channels (see Figure 2.8).

Metallic substrates present several advantages over their ceramic counterpart. First, thinner walls, as thin as 0.05 mm, can be designed. Hence, at equal dimensions, metallic substrates show higher cell densities and a higher open frontal area -- about 90% -- than ceramic substrates. The pressure drop along the monolith is thus reduced. Secondly, the lower thermal inertia of the materials leads to faster light off. Third, metallic monoliths do not need steel housing like ceramic monoliths; they can be directly incorporated into the converter system.

However, they are non-porous structures, and need pretreatments to improve the adherence of the washcoat layer. Moreover, they experience durability problems, and are still expensive compared to ceramic monoliths. Therefore, they are not widely used.

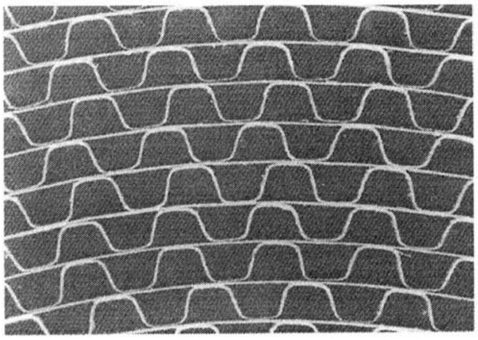

Fig. 2.8: *Closed-up view of a metallic monolithic substrate* [11]

2.2.2 The washcoat

The washcoat determines the overall stability and durability of the finished catalyst. In fact, its function can be divided into the three following main points:

- The washcoat provides a high surface area support to carry the catalytic species. For instance, typical coated ceramic monoliths have internal surface areas of about 20-100 m^2/g, whereas the uncoated substrate has a surface area between 0.1 and 2 m^2/g (see 2.2.1).
- It increases the resistance of the catalyst against deactivation processes occurring at high temperatures such as sintering and agglomeration of species, which decrease the catalytic area (see section 3.3.2).

- It supports the catalytic function of the precious metals, and even takes part in the catalytic reactions, in particular through the oxygen storage components evoked previously.

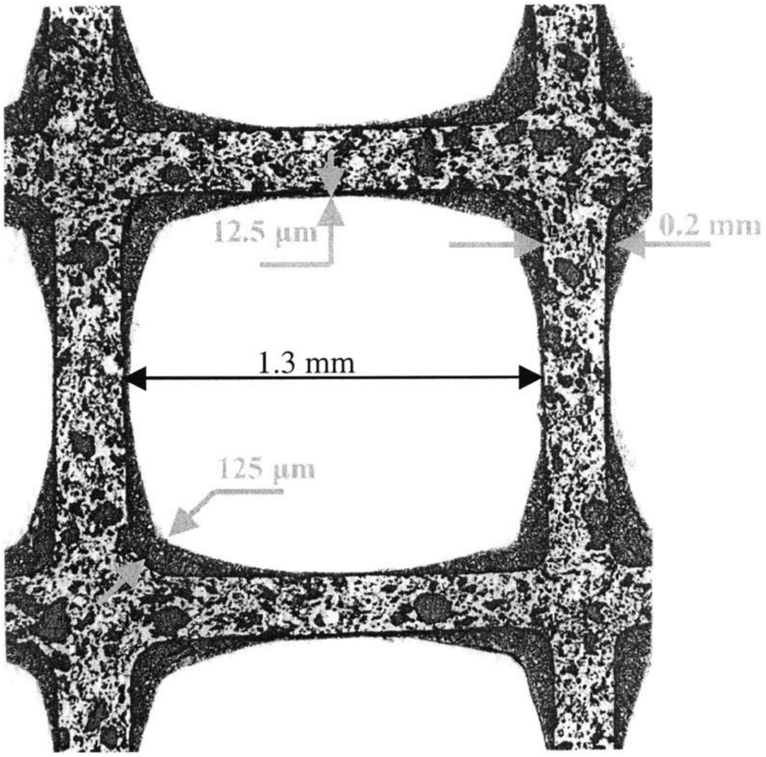

Fig. 2.9: *Ceramic monolith (porous, light color) coated with a catalyzed washcoat (grey color)* [12]
(The dimensions on the figure are to scale)

As shown on Figure 2.9 above, the washcoat is deposited over the entire walls of the channels. As can be seen, it is deposited non-uniformly in the case of square channels and concentrated in the corners. Thus, the coating layer is about 10 to 30 µm thick on the side of the channel --about 10 times thinner than the substrate walls--, and 100 to 150 µm thick in the corners. In fact, the amount of washcoat that can be deposited is limited by the pressure drop constraints along the monolith. Indeed, a high surface area is needed, but too much washcoat decreases the open area, thus increasing the pressure drop to an unacceptable level. Hence, the content of the coating layer varies from 5 to 20 wt % with respect to the monolithic support. Typical numbers for a 400 cells per square inch (cpsi) ceramic monolith are 15 wt % and a loading about 100 g/L monolith volume.

i- The washcoat components

The washcoat is composed of inorganic oxides organized in two groups of particles:

- The primary particles, from 10 to 20 nm in diameter (for a fresh catalyst)
- The secondary particles, from 2 to 30 μm in diameter, pure agglomerates of inorganic oxides or microscopic mixtures of several of them.

A typical washcoat surface is represented on Figure 2.10 below.

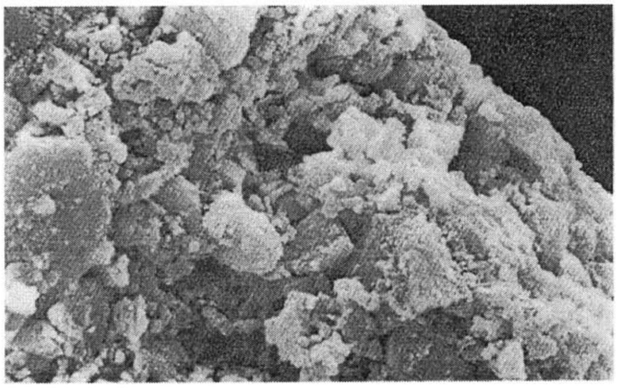

Fig. 2.10: *Scanning Electron Microscope view of a washcoat layer* [11]

These inorganic oxides can be divided into three categories:

- The main washcoat components present in largest amounts
- The promoters
- The oxygen storage components

The next sections give their main characteristics.

.

a) Major constituents

The choice of the main constituents determines the main thermal and physical characteristics of the washcoat. Hence, the eligible species have to fulfill certain criteria. For instance, the washcoat and substrate thermal characteristics must be close to ensure a good adhesion between these two parts of the monolith. Moreover, the washcoat must stabilize the catalytic species, and fix them quite easily on its surface. Based on these considerations, typical carriers are alumina Al_2O_3, silica SiO_2, titanium oxide TiO_2, and zeolites, combinations of silica and alumina, also called crystallite alumina silicates. Among those, Al_2O_3 is the most commonly used. Under catalytic converters conditions, alumina takes the crystallite form γ-Al_2O_3.

b) The promoters

The promoters can be split into two groups:

- *The physical promoters*

  These additives stabilize the internal surface area of the washcoat; they also maintain the physical integrity of the deposited catalytic agents. The precise cause of their stabilizing effect is not known, but high-resolution surface studies indicate that these oxides enter into the surface structure of γ-Al_2O_3, and thus greatly diminish the rate of physical and chemical changes on the surface, most particularly the mobility of Al and O ions, thus reducing the rate of sintering.

  Lanthanum oxide La_2O_3, barium oxide BaO, calcium oxide CaO, magnesium oxide MgO, and silica SiO_2 are examples of such promoters.

- *The chemical promoters*

  These additives enhance the chemical activity of the catalytic agents.

  Among the most common additives, zirconium oxides and cerium oxides are both chemical and physical promoters. They are thus present in significant proportions, and therefore often considered as main constituents. Between the two, cerium oxides are the most commonly used. Ceria interacts with the neighboring catalytic particles, thus facilitating the reactions between the gaseous species and the catalytic surface. Moreover, cerium oxides act as efficient oxygen storage components (see next section).

c) The oxygen storage components

As stated in the previous paragraph, cerium oxides are the in-use oxygen storage components in catalytic converters.

Ceria is known as a non-stoichiometric compound; nevertheless, it is found in the washcoat under two main identifiable forms: a reduced form Ce_2O_3 and an oxidized form CeO_2. Under lean operation, the reduced form is oxidized, thus storing oxygen inside its oxidized form; and under rich operation, the oxidized form is reduced, releasing oxygen available for further oxidations of CO and HC. These oxidation and reduction processes occur according to the following global reaction:

$$Ce_2O_3 + \frac{1}{2} \cdot O_2 \leftrightarrow 2.CeO_2$$

To summarize, typical in-use washcoats include between 10 and 20 wt % of cerium oxides, 1 to 2 wt % of stabilizers La_2O_3 or BaO, and the rest of γ-Al_2O_3.

ii- The washcoat porous structure

To provide the high surface area support necessary to carry the catalytic species, the washcoat presents a complex porous structure with pore sizes from 1 to 10^5 nm. According to the IUPAC (International Union of Pure and Applied Chemistry), the pores are classified regarding their diameter as follows:

- Micropores: $d < 2$ nm
- Mesopores: 2 nm $< d <$ 50 nm
- Macropores: $d > 50$ nm

The spaces between the secondary particles are responsible for the macroporosity of the washcoat, whereas the spaces between the primary particles constitute the micro- and mesopores.

The most common pore distribution is bimodal with a peak of pores in the micro-mesopore region -- generally simply called micropores --, and the other in the macropore region. In this case, the limit of the micropores is arbitrary fixed at 10 or 12.5 nm.

These washcoat pores have to remain sufficiently large to avoid strong diffusional limitations.

2.2.3 The catalytic particles

i- Historical background

Two categories of catalytic species have been tested since 1976:

- noble metals: platinum (Pt), palladium (Pd), rhodium (Rh), ruthenium (Ru), and iridium (Ir).
- base metal oxides: CuO, MnO_2, Cr_2O_3, Co_3O_4, V_2O_5, or a mixed oxide coming from the combination of several of these.

The base metal oxides were investigated between 1976 and 1979. They are less expensive than the noble metals and more readily available. However, their catalytic activity was found to be too low compared to the noble metals to obtain high conversion catalytic converters. Therefore, the noble metals have been mostly used since 1979. Among these, ruthenium and iridium were used at the beginning of this period only. In fact, under lean operation, they form volatile and/or toxic oxides, which decrease the catalytic area. Thus, the three main noble metals to be used nowadays are: Pt, Pd, and Rh.

One or several catalytic species can be used at the same time. Until the early nineties, mostly Pt/Rh combinations existed in three-way catalysts. However, platinum and rhodium are expensive noble metals compared to palladium. Thus, from the mid-nineties, Pd has been seriously considered to replace Pt. Pd has even been considered to replace Rh. In particular, all palladium technologies seem compatible with nowadays position and designs of the catalytic converter. Figures 2.11(a) and 2.11(b) below illustrate this transformation in the use of noble metals between 1992 and 1997, most particularly the considerable increase in the production and use of palladium.

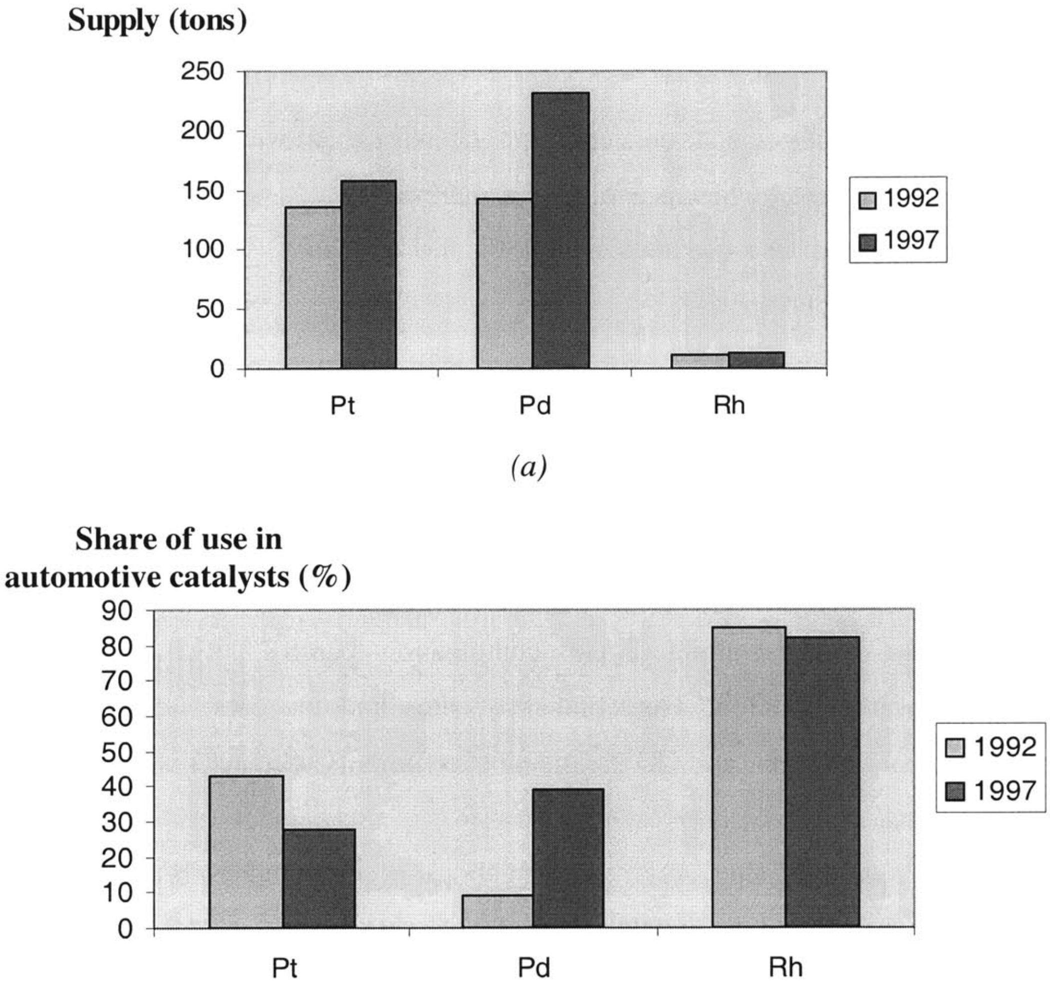

(a)

(b)

Fig. 2.11: *World supply of platinum, palladium, and rhodium (a) and share of its use in automotive catalysts (b)* [11]

Nowadays, most TWCC include a precious metal loading of about 2-5.5 g/L catalyst volume in a Pt : Pd : Rh mass ratio about 0-1 : 8-16 : 1.

ii- Dispersion and form of the catalytic species

The precious metal concentration can be either uniform in the radial and axial directions of the monolith structure or not. In fact, a non-uniform distribution of the catalytic agents within the washcoat layer is much more common. Such a configuration is often required for good kinetics and to eliminate bad interactions between different species. For example, the two following distributions can be encountered:

- Each precious metal is selectively deposited on different washcoat components. Thus, zirconium oxides constitute the preferred supports for rhodium.
- One precious metal concentration decreases as we penetrate inside the washcoat layer, whereas another one increases.

The deposition of the precious metals on the washcoat is characterized by the dispersion coefficient defined as:

$$\text{Dispersion}=\frac{\text{number of catalytic sites on the surface}}{\text{theoretical number of sites present}}\cdot 100$$

The number of catalytic sites on the surface is measured by selective chemisorption. This experiment measures the amount of gas adsorbed per unit weight of catalyst from which the catalytic area can be computed. This computation requires the knowledge of the stoichiometry of the reaction. The number of sites and the catalytic area are then proportional accordingly. H_2 and CO are the most commonly used selective adsorbates in these experiments.

The theoretical number of sites present in the catalyst is computed from the known mass loading in noble metals and the metals' molecular weights.

Since only surface atoms show some catalytic activity, the dispersion coefficient measures the number of catalytic sites effectively available for reactants adsorption and reaction. Therefore, the higher the dispersion, the higher the catalytic activity. Nowadays, dispersions from 10 to 50 % are encountered; they can even be a bit higher for fresh catalysts. When several noble metals are simultaneously used, each metal is characterized by its own dispersion coefficient.

To increase the dispersion, and hence the catalytic area, the noble metals are deposited under the form of small crystallites. Thus, the average catalytic particle size in a fresh catalyst that has not been heated any higher than 500 C lies below 50 angstroms, as illustrated on Figure 2.12. In fact, for the upper-right group of particles on Figure 2.12, the average size is about 30 angstroms. Not only do small particles ensure a high catalytic area, but they also happen to be more reactive than bigger ones. For instance, they are more easily oxidized [15].

The average distance between two particles is about the added size of two particles, about 65 angstroms for the same group of particles as above.

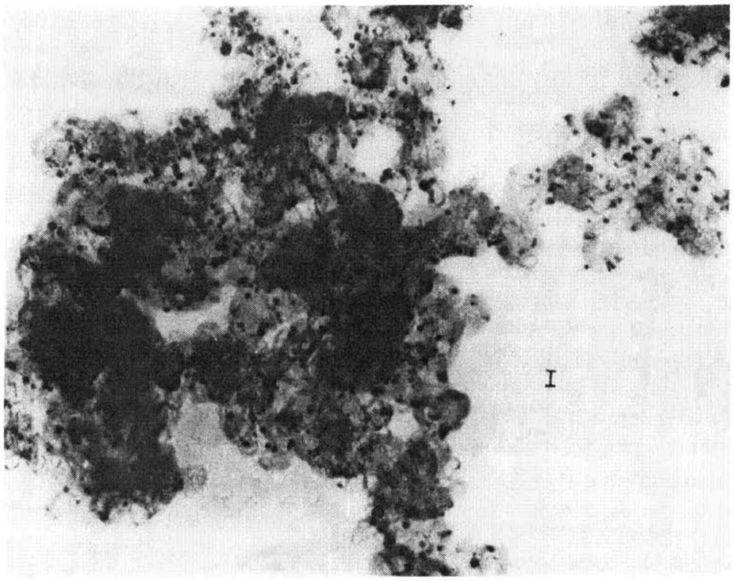

Fig. 2.12: *Transmission Electron Micrograph of platinum crystallites on a γ-Al_2O_3 carrier* [12]. *The black bar represents 100 angstroms.*

When only one noble metal is deposited, the catalytic particles are clusters of atoms as represented on Figure 2.13. Thus, a Pt particle of 2 nm in diameter consists of 220-230 atoms [15].

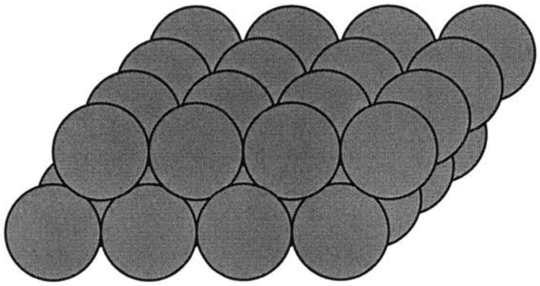

Fig. 2.13: *Cluster of Pt atoms*

When several metals are deposited simultaneously, Pt and Rh for example, part of these clusters is alloyed [16]. In such alloyed particles, the different constituents segregate according to their relative properties. The principal factors affecting the surface segregation of an alloy AB are [17]:

- The differences in bond strength, related to the heat of sublimation of the two components and to their enthalpy of mixing
- The difference in atomic size: the component with the smallest size segregates at the surface.
- The difference in surface tension: the species with the lower surface tension segregates at the surface

For example, in Pt/Rh clusters, Pt tends to segregate to the surface because of its lower surface tension. Nevertheless, the Pt surface enrichment is not sufficiently severe that top layers of almost 100% Pt are formed, as illustrated on Figure 2.14 below.

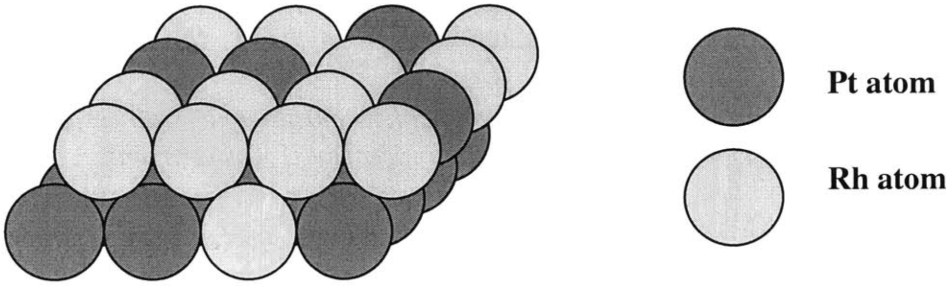

Fig. 2.14: *Segregated cluster of Pt and Rh atoms*

We will talk again about the segregation process in Chapter 3 to explain how this process affects the catalytic activity of the converter.

2.3 Making the finished catalyst

The making of the finished catalyst reveals the existence of two sorts of monolithic catalysts:

- Incorporated catalysts
  All the components (substrate material, washcoat components and catalytic species) are added together to the ingredient mixture, from which the monolith is to be subsequently formed and calcined. With this fabrication procedure, a significant amount of catalyst remains deep into the matrix.

- Coated catalysts
  The substrate is first built, and then coated with the washcoat and the catalytic species.

Because of the inefficient use of the active materials, incorporated catalysts are quite rare, and thus this section only covers the making of coated catalysts.

Two coating procedures exist:

- Coating the formed monolith with the catalyzed washcoat
- First coating the monolith with the uncatalyzed washcoat and then disperse the noble metals.

The second procedure is the most widespread since it results in higher dispersions, and therefore is the one described in the following sections.

2.3.1 Depositing the uncatalyzed washcoat on the monolith substrate

The washcoat is applied by a dipping process as an acidified aqueous slurry whose solid content is about 30-40%. The slurry bonds physically and chemically to the monolith surface.

In ceramic monoliths, some of the washcoat fills the large pores of the substrate, which provides adhesion. Hence, the particles of the washcoat need to be small enough compared to the size of the substrate pores to obtain a good adhesion. Therefore, before application to the monolith, the slurry is ball-milled for at least two hours to reduce the particle size.

Non-porous metallic surfaces are pretreated to add roughness and often made Al-rich to easily bond the alumina containing washcoat.

After submersion, the excess slurry is air-blown to clear the channels and dried at 110 C. Calcination between 300 and 500 C then bonds securely the washcoat to the walls and eliminates the excess preparation components.

Another alternative approach for metallic monoliths is to precoat the metal with the washcoat before wrapping or forming the metal into the monolithic structure.

2.3.2 Dispersing the noble metals on the coated monolith

The deposition of catalytic species on the uncatalyzed washcoat includes three parts:

- The impregnation and fixation of the catalytic species
- The drying of the catalyzed washcoat
- The calcination of the catalyzed washcoat

i- Impregnation and fixation

The most common procedure consists in impregnating an aqueous solution containing a salt or precursor of the catalytic element(s). Most preparations simply involve soaking the coated monolith into the solution, and use the following phenomena to disperse the catalysts:

- <u>Capillarity</u>

  If the surface is hydrophilic, the capillary forces force the aqueous solution inside the pores of the washcoat. If the surface is non-hydrophilic, a surface active agent is added, or water is replaced by a non-aqueous solvent with a lower surface tension to transport the precursors.

- Electrostatic adsorption

  For instance, the surface charge of alumina being negative, cations adsorb easily and uniformly over the entire surface.

- Ion exchange

  This technique leads to highly dispersed catalytic components, but is mostly used with zeolite catalysts.

Examples of ions from used precursor salts are $Pt(NH_3)_2^{2+}$, Pd^{2+}, $PdCl_2^{2-}$. Cations are usually derived from nitrate and oxalate salts such as $Pd(NO_3)_2$ and anions from chloride precursor salts such as Na_2PdCl_4.

To be certain of the precise amount of catalytic species dispersed on the washcoat, the water pore volume, or amount of water that can be uptaken by the carrier, is evaluated, and the salts are diluted in this precise amount of water, then used to impregnate the washcoat.

Then, to ensure a stable catalytic area, the catalytic species have to be fixed on the washcoat. Two main fixation processes are used:

- Adaptation of the pH of the solution to precipitate the catalytic species in the pores

The pH is adapted by pretreatment of the carrier by an adequate solution. For instance, pretreatment of Al_2O_3 by NH_4OH enables to precipitate hydrated PdO after addition of an acidic Pd salt. H_2S can also be used as a precipitating agent, with Rh_2O_3 for example. The deposited oxide is then reduced by exposure of the surface to a flow of H_2.

- Addition of reducing agents to precipitate catalytic species as metals

  This method is useful with ionic catalytic precursors. For example, HCOOH can be used to reduce Pd^{2+} to Pd. Noble metals are easily reduced to their metallic state.

ii- Drying

Excess water and other volatile species are removed by forced air drying at about 110C.

iii- Calcination

Calcination by forced air to about 400-500 C is employed to remove all traces of decomposable salts and additives used to precipitate the noble metals.

2.3.3 Constraints

Regarding the catalytic activity of the monolith, the resulting position of the introduced elements matters as much as the amount in which they are deposited. Indeed, all species need a precise position in the washcoat to function properly, especially to eliminate bad interactions. For example, rhodium reacts with CeO_2, which reduces both of their activities. Rhodium can also form alloys with palladium, which leads to the segregation of palladium at the surface and decreases the rhodium surface area. The location of these three species has thus to be done in consequence. A possible solution to these configuration problems lies in segregated washcoats. Figure 2.15 illustrates this point with a two-layer washcoat.

The size of the washcoat particles constitutes another constraint. Indeed, as previously said, the carrier particles must be compatible with the substrate pore size. Furthermore, studies proved the smaller the noble metals particles, the better the performance.

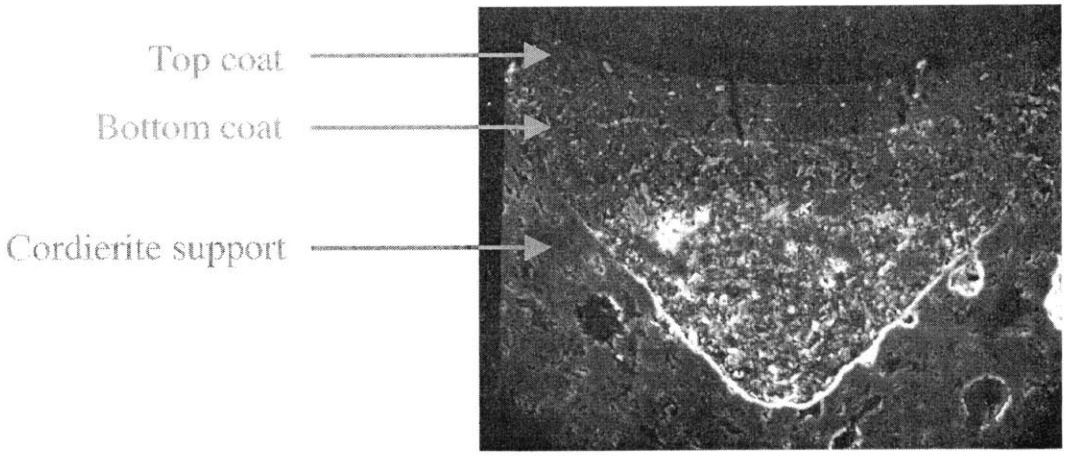

Fig. 2.15: *Double coat automotive catalyst* [12]

Chapter 3: Physical insight into the catalytic process in three-way catalytic converters

Automotive aftertreatment systems reduce the pollutants emissions by the process of heterogeneous catalysis. Heterogeneous catalysts are solid catalysts to which the reacting mixture is exposed to speed up reactions. Indeed, they can increase rates by factors of 10^{10}-10^{20}; rate enhancements as large as 10^{40} have even been observed. This chapter first explains how such rate enhancements are obtained and then details the interactions between the monolith surface and the chemical species involved in the catalytic reactions.

3.1 Overview of the catalytic action

Catalysts, whether homogeneous or heterogeneous, increase the reaction rate by changing the local environment around the reactants present in the mixture. They participate in the chemical reactions, but are regenerated at the end, and thus do not appear in the global equation for the catalyzed reaction.

Catalysts can work in a variety of different ways, and, depending on the reaction and the catalysts used, different modes of catalytic action can be encountered. This section presents the main modes of action of heterogeneous catalysts used in automotive applications (Pt, Rh, and Pd).

3.1.1 Initiating the reaction

The catalyst helps to initiate the catalyzed reaction by reducing the energy barriers to reaction. Figure 3.1 illustrates this catalytic property with the oxidation of CO by O_2 at 800 K. Figure 3.1(a) shows the potential energy diagram of the reaction occurring in the gas phase, whereas Figure 3.1(b) shows the potential diagram of this same reaction catalyzed by platinum. On 3.1(b), CO* and O* are intermediate adsorbed species on platinum; section 3.2 gives more details on the nature of the reactions occurring on the surface. The energy levels of the catalyzed reaction are explained in Chapter 4.

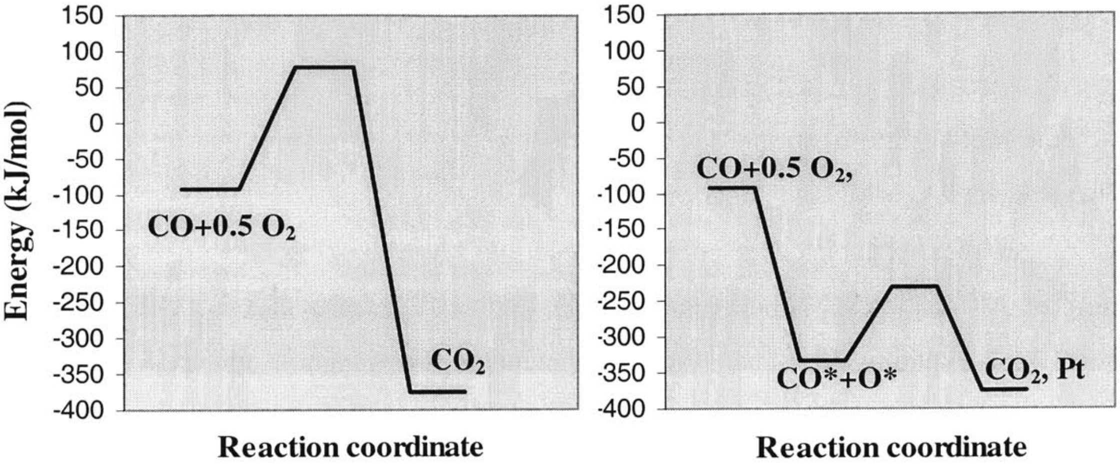

(a) *(b)*

Fig. 3.1: *Potential energy diagram for the oxidation of CO at 800 K (a) Homogeneous reaction; (b) Pt-catalyzed reaction*

By decreasing the activation barriers to reaction, the catalyst makes the catalyzed reaction possible at lower temperatures. At sufficiently high temperatures, however, the gas-phase reactions may be much faster than catalytic reactions.

3.1.2 Stabilizing the intermediates

Automotive catalysts, like all heterogeneous catalysts, speed up the reaction by binding some key intermediates, and thereby stabilizing them on the catalytic surface. The process lowers the enthalpy of formation of the intermediates via the strength of the adsorbate-surface bond. Therefore, the intermediates concentrations increase and thereby increase the rate.

However, if the intermediates are too strongly stabilized, they are not willing to further react, thus making it difficult for the products to be formed. Hence, the best catalysts are catalysts that bind the reactants strongly, but not too strongly. This is the so-called Sabatier principle.

3.1.3 Holding the reactants in close proximity

As presented in Chapter 2, automotive catalysts are deposited on the walls of the monolith channels under the form of small particles, typically less than 50 angstroms in diameter in fresh catalysts. This organization concentrates the reactants close to the surface and close to each other on the surface. This close proximity facilitates the reactions.

3.1.4 Stretching the bonds

Heterogeneous catalysts stretch the internal bonds of the adsorbates while interacting with them. By stretching these bonds, the enthalpy of activation of the corresponding reaction is lowered, thus lowering the intrinsic reaction barrier. The mechanism makes bonds easier to break (see section 3.2.1).

The next section illustrates the above modes of action; it gives more details on the process of heterogeneous catalysis, and draws a microscopic picture of what exactly happens at the surface of the catalyst.

3.2 Heterogeneous catalysis in catalytic converters

Heterogeneously catalyzed reactions consist of three steps:

1) *Adsorption:* the reactants adsorb on bare sites on the catalytic surface
2) *Surface reactions:* the adsorbed molecules recombine and react on the surface to form the products
3) *Desorption:* the newly formed products desorb from the surface, regenerating bare sites now available for new adsorption and surface reactions.

In fact, for a reaction to be called a heterogeneous catalytic event, at least one of the reactants must be attached to the surface. If one of the reactants is bound to the surface, the catalytic process is called an Eley-Rideal process; if all the reactants are bound to the surface, it is a Langmuir-Hinshelwood process.

The three steps cited above correspond to the intrinsic chemical part of the catalytic process. Definitions of heterogeneous catalysis may include two more diffusional steps:

- The reactants have to diffuse from the bulk gas phase to the surface of the catalyst.
- After being formed, the products have to diffuse from the surface of the catalyst to the bulk gas phase.

The following sections explain the main characteristics and principles of each of the three chemical steps. The diffusion steps will be dealt with in Chapter 4.

3.2.1 Adsorption

As represented on Figure 3.2, adsorption of the reactants on the catalytic surface is the result of two attractions: a long-range attraction called physisorption and a short-range attraction called chemisorption.

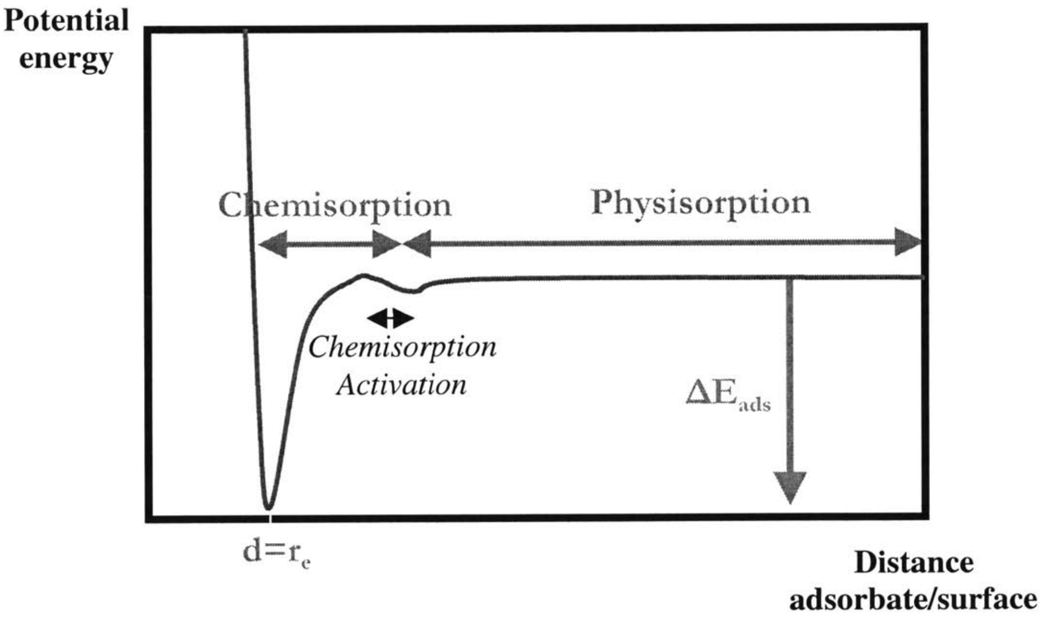

Fig. 3.2: *Potential energy curve for the adsorption process* [18]

- *Physisorption*

Physisorption is a weak attraction arising from Van der Waals forces. Its effectiveness depends on temperature and pressure. High pressures and low temperatures favor the process.

These attraction forces result in a minimum in the potential energy (PE) curve at a typical distance from the surface greater then 3 nm, which justifies the appellation of "long-range" attraction. This minimum appears on Figure 3.2 as the first minimum from the right. The low depth of this minimum reveals the weakness of the attraction.

This process is indiscriminate and non-activated. Thus, any species can physically adsorb on any solid surface, and no barrier prevents the atom or molecule approaching the surface from entering this physisorption as shown on Figure 3.2.

- *Chemisorption*

Chemisorption is a stronger attraction than physisorption, responsible for the formation of covalent bonds between the adsorbate and the catalyst. Hence, this attraction corresponds to a much deeper minimum in the PE curve at shorter values of the distance between the surface and the adsorbate.

Although the weak physical forces are present in any adsorbate/solid systems, chemisorption is an activated process with an energy barrier (see Fig. 3.2).

When one talks about adsorption in heterogeneous catalysis, one usually refers to chemisorption. And indeed, the adsorbates participate in the surface reactions once they are chemically bound to the surface. Hence, from now on, adsorption will simply refer to chemisorption.

i- Two types of chemisorption

Two types of chemisorption can be encountered.

a) Molecular chemisorption

The incoming molecule attaches itself to the solid without breaking a bond.

CO, NO, and unsaturated HC at low temperatures are examples of molecularly adsorbing molecules on Pt, Rh, and Pd.

b) Dissociative chemisorption

The adsorbate sticks by breaking a bond. To be rigorous, dissociative adsorption occurs in two steps: first, the molecule binds to the catalytic materials, and then it dissociates on the catalytic surface. However, these two steps occur simultaneously, and available data concerning this type of adsorption (heat of adsorption for instance) group the two steps.

H_2, O_2, and unsaturated HC at large temperatures adsorb dissociatively on Pt, Rh, and Pd.

ii- Nature of the adsorption process and properties of metal catalysts

The adsorption process results from the interaction between the orbitals of the adsorbate and the orbitals of the metallic surface. By interacting, these orbitals share electrons, which leads to the formation of covalent bonds.

Metals are particularly good catalysts because of their ability to strongly interact with the incoming molecules. This strong and efficient interaction appears to be linked to the three main metal properties described below.

a) Metals have quasi-entirely filled d-orbitals

This interesting property of metals corresponds to an anomaly in the filling of the orbitals of the periodic table elements. Indeed, let us consider the example of platinum Pt.

Iridium Ir is the element just before Pt in the same row. Iridium has 77 electrons, and its electronic structure is: [Xe] $4f^{14}$-$5d^7 6s^2$. Platinum only has one more electron than Iridium. We would expect this electron to keep on filling the 5d-orbital, thus leading to the following electronic structure: $5d^8 6s^2$. However, the actual external structure of Pt is: $5d^9 6s^1$. Therefore, Pt 5d-orbitals only need one more electron to be completely filled. Hence, they strongly interact with the orbitals of incoming molecules to gain this missing electron.

This particularity of platinum, but also of the other metals (Pd and Rh, collectively named the Platinum Group Metal PGM) used in automotive catalytic converters, is responsible for their good performances as catalysts. In particular, only strongly interacting d-orbitals like the ones described above succeed in dissociatively adsorbing H_2, which can only react on the surface under its atomic form. Figure 3.3 illustrates this dissociative adsorption. The figure shows two neighboring metal atoms represented with their d-orbitals and an incoming H_2 molecule. Orbitals of the same sign interact, which maintains H_2 close to the surface and at the same time weakens its bond. Depending on the force of the interaction, the bond may or may not be broken. With platinum, this interaction is strong enough and the bond is broken.

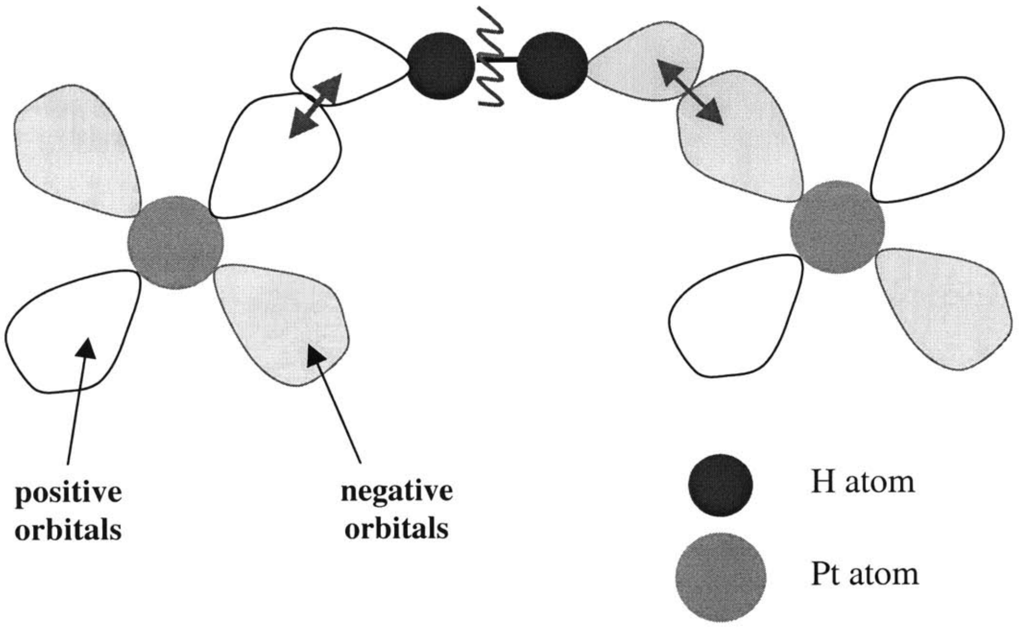

Fig. 3.3: *Dissociative adsorption of H_2 on platinum*

b) Metals satisfy the 18-electron rule

Metals try to reach the external electronic structure of the nearest noble gas in the periodic table, which contains 18 electrons. For example, the nearest noble gas to Pt is Radon Rn whose electronic structure is [Xe]$4f^{14}$-$5d^{10}6s^{2}6p^{6}$. According to the 18-electron rule, Pt thus tries to gain 8 electrons. Part of these electrons is gained by the bonds formed with the neighboring metallic atoms. The metal then tries to form bonds with incoming molecules to gain the missing ones. This rule urges the metallic surface to interact with the gaseous molecules that arrive on the surface.

c) Metals can form several covalent bonds with adsorbing molecules

Metallic surfaces stabilize intermediates by their ability to form several covalent bonds with the incoming molecules. For example, CO can adsorb molecularly on the platinum surface in four different configurations[1], forming one, two, three, or four bonds with the surface, as illustrated on Figure 3.4. The adsorbing configuration depends on the types of sites present on the surface.

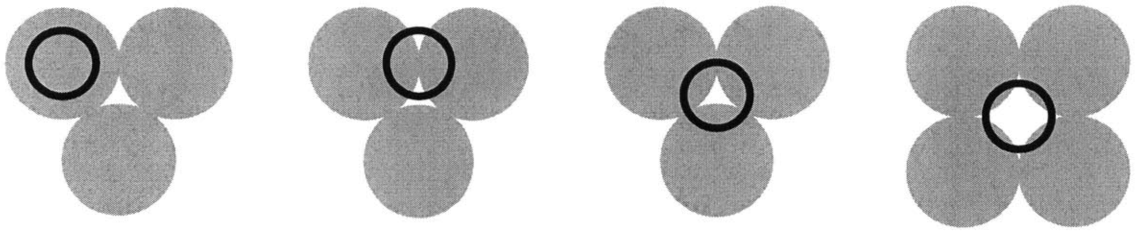

Terminal

Bridging (2f site)

Bridging (3f hollow)

Bridging (4f hollow)

Fig. 3.4: *Four adsorbing configurations of CO* [19]

The formation of several bonds with the surface weakens and partially breaks the triple bond between the carbon and oxygen atoms composing the CO molecule. Thus, the metal both stabilizes the intermediate CO* and improves its likeliness to perform further reactions.

However, the size of the catalytic particles affects the propensity of metals to form several bonds with the adsorbates, particularly with the carbon atoms [15]. Small particles as the ones encountered in fresh catalysts tend to form single bonds with the adsorbates. Hence, this property of metals only manifests itself once the particles have grown under the effect of aging. It thus appears as a natural way to fight against the loss of performance due to sintering (see section 3.3.2).

iii- Selectivity

Chemisorption is a selective process [17]. Thus, in TWCC impregnated with Pt and Rh for example, CO preferentially adsorbs on Pt, whereas O_2 and NO preferentially adsorb on Rh. H_2 is a non-selective molecule, both Pt and Rh interacting strongly enough with it to dissociate the molecule. These preferences result from differences in bond strength; for instance the Rh-O bond strength is much stronger than the Pt-O one.

---

[1] CO always adsorbs on the surface by the carbon atom

The selectivity of the adsorption process modifies the surface composition of alloyed particles. As explained in Chapter 2, part of the catalytic particles is alloyed in multimetallic converters, and these alloyed particles take the form of segregated crystallites. For example, Pt segregates to the surface in Pt/Rh particles (see Figure 2.14). In the presence of selectively adsorbing molecules, the natural segregation is altered. Figure 3.5 below illustrates this modification. Figure 3.5(a) shows the segregated cluster before adsorption. On 3.5(b), two molecules come close to the surface: CO and NO. The CO molecule adsorbs on one or several Pt atoms as explained in the previous section. The NO molecule, by coming close to the Pt surface, pulls the Rh atoms of the second layer to the surface by the strength of its interaction with these atoms. The NO molecule then adsorbs on these Rh atoms. Therefore, there is a dynamic adjustment of the surface atomic arrangement according to the gas stream composition.

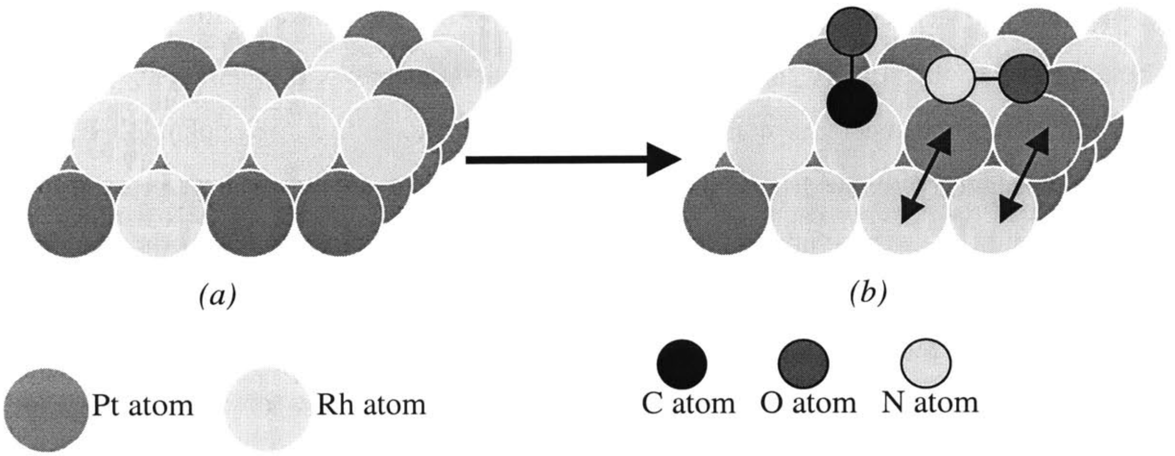

Fig. 3.5: *Alteration of the surface segregation by selective adsorption (a) Surface before adsorption; (b) effect of adsorption*

The occurrence of the above process favors an optimum performance of the multimetallic catalyst. Indeed, first, the species adsorb on the best catalyst for them. Second, the alteration of the surface composition ensures that all reactants are well mixed on the surface. This increases their proximity and so facilitates surface reactions.

3.2.2 Surface reactions

Once the reactants have adsorbed on the surface, they recombine and react to give further intermediates and finally lead to the products. These surface reactions occur on the catalytic surface, as expected, but can also involve the rest of the washcoat surface, which will be called the support in the following paragraphs. This section describes the principles which govern these reactions.

i- Reactions on the catalytic surface

As explained in the introduction to section 3.2, two main types of surface reactions exist: Langmuir-Hinshelwood reactions, where all reactants are adsorbed species, and Eley-Rideal reactions, where one of the reactants is still in the gas phase.

In both cases, the reactants need to be close to each other to react. For example, the surface species CO* and O* need to be within 1.78 angstroms to react and produce CO_2. In the case of Eley-Rideal mechanisms, diffusion in the gas phase brings the gaseous reactant close to the surface. In the case of Langmuir-Hinshelwood mechanisms, surface diffusion brings the reactants within the required distance. In fact, as explained in 3.2.1 iii-, the presence of alloyed particles and the selectivity of the adsorption process also help the mixing of the reactants on the surface and bring them close to each other.

Furthermore, the reactants need to be in the right configuration to react. Their configuration not only affect the occurrence or not of the reaction, but also the pathway the reaction will follow. For example, if CO* is close to a single O* and in the right configuration, CO* and O* react to form gaseous CO_2. However, if CO* is close to two O* and in the right configuration, the intermediary complex O*- CO*- O* forms, and then leads to the formation of CO_2 [20].

The catalyst can be designed to block undesirable side reactions. However, as revealed in Chapter 2, the mode of deposition of the catalytic particles in automotive converters makes it difficult to control the final form of the particles, and thus their structure.

ii- Reactions involving the support

The support can participate in the catalytic reactions in two ways:

- *Directly:* the support and the catalytic particles constitute two functional groups in the supported catalyst that are able to catalyze the main reactions. This occurs in bifunctional catalysts.
- *Indirectly:* the support, by itself, is not able to catalyze the main reactions; hence the main part of the reaction occurs on the catalytic surface. However, the support participates in the reactions through the spillover process.

The following paragraphs explain what the above roles consist of.

a) Bifunctional catalysis [15]

Bifunctional catalysts are designed so that part of the reactions occurs on the support. Reactants can directly adsorb on the support active sites and react, as well as on the noble metals. Nevertheless, the term bifunctional catalyst does not refer to a competitive catalysis between the two functional groups. On the contrary, the support and the metals participate together in the same reactions. The water-gas shift reaction $CO + H_2O \rightarrow CO_2 + H_2$ is an example of bifunctional mechanism [21]. Indeed, the reactants go through the following intermediary steps:

$$CO - Metal + OH - Al_2O_3 \rightarrow COOH - Al_2O_3 + Metal$$
$$Metal + COOH - Al_2O_3 \rightarrow Al_2O_3 + CO_2 + H - Metal$$

where the OH groups on alumina come from direct reaction between H_2O and alumina.

For automotive applications, the support is generally wanted catalytically inert toward the main catalytic reactions so that the performance could be better controlled. Hence, apart from the water-gas shift reaction, monolithic surfaces can be considered monofunctional. Indeed, for example, the direct rates of exchange of H_2 and O_2 on alumina are respectively one order of magnitude and two to three orders of magnitude smaller than on the metal particles [22].

However, the support in even monofunctional catalysts participates in some reactions, because it is responsible for unwanted or parasitic reactions, but above all through the spillover phenomena detailed in the following section.

b) Spillover catalysis

Generally speaking, the spillover phenomenon is the transport of active species adsorbed or formed on one phase to another phase which does not adsorb or generate these species under the given conditions. In other words, in a catalytic converter, spillover is the process by which adsorbed reactants move from the catalytic surface on which they formed to the support surface, as illustrated on Figure 3.6 with the example of H_2. The reverse process -- the transport of species from the support to the catalytic surface-- is called reverse spillover. As evoked in the general definition, spillover plays an important role at low temperatures when the support cannot adsorb the species itself. Thus, for instance, H_2 cannot be adsorbed and dissociated by the washcoat support at 300C, but atomic H can still adhere to the support surface via spillover.

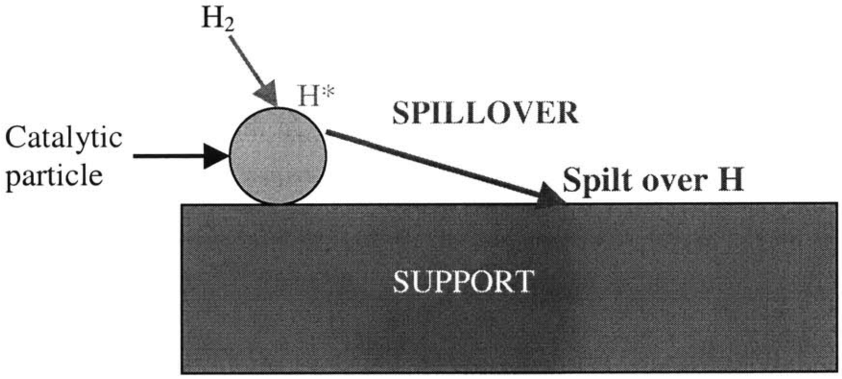

Fig. 3.6: *Definition of the spillover phenomenon*

The spilling-over species move from the catalytic surface to the support surface by surface diffusion due to the high concentration gradient at the catalyst-support interface. Further migration is then possible along the support surface. Since diffusion is involved, only the fast diffusional species are likely to spillover. Thus, the main spilt-over species are H, O, and CO, in decreasing order of diffusivity. NO spillover has also been observed but only at high temperatures. So hydrogen is the fastest diffusing species and has been observed to diffuse as far as 200 nm from the Pt particles on the Al_2O_3 surface at 400 C [23].

Studies of spillover have elucidated the precise means of transport along the support surface. Hydrogen migrates via the hydroxyl groups present on the support [23], whereas O moves via the presence of oxygen vacancies at the surface [24].

Spillover plays three different roles in catalytic converters.

- *It creates active sites on the support surface.*

  The spilt-over species is attached to the surface of the support to create these sites. Atomic hydrogen is especially active in this role. This type of spillover is called irreversible spillover since the spilt-over species will react with the gas stream or other spilt-over species and will not return to the catalytic metallic sites.
- *It provides reactants for reactions on the above sites.*
- *It stores reactants on the support.*

  These reactants are available for reactions on the active catalytic surface through the reverse spillover process.

The first two roles are minor because these actions on the support are slow. Therefore, the catalytic activity in automotive supported catalysts can be described as follows: the main part of the reactions occurs on the catalytic surface, and the support acts as a tank that stores active reactants through spillover and makes them available to the catalytic particles when they need them through reverse spillover. As said earlier, the water-gas shift mechanism constitutes an exception to this general behavior. The oxygen storage process constitutes a good example of the storage function of the support and is detailed in the next section.

iii- Oxygen storage process

As explained in Chapter 2, cerium oxides (CeO_2, Ce_2O_3) constitute the oxygen storage components in catalytic converters. They store oxygen during lean operation of the engine, and restitute it during rich operation. This oxygen storage process occurs through spillover, as represented on Figure 3.7.

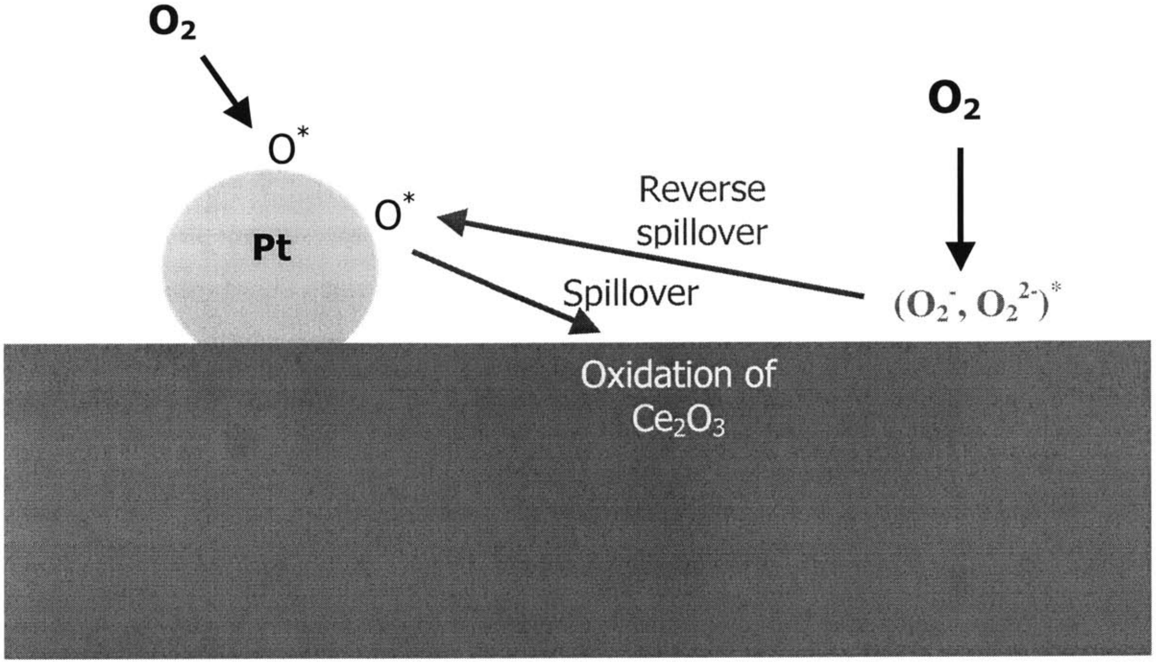

Fig. 3.7: *Oxygen storage process*

At low temperatures (up to about 350 C), ceria is able to adsorb O_2 directly under the ionic forms O_2^-, O_2^{2-}, but cannot dissociate it [25]. The major oxygen storage process requires atomic oxygen. Hence, in the absence of platinum, no oxygen can be stored on ceria at low temperatures.

Unlike ceria, platinum is able to adsorb O_2 dissociatively even at low temperatures. Thus, in the presence of platinum, oxygen atoms form on the metallic surface. These oxygen atoms have two origins:

- The direct dissociative adsorption of O_2 on Pt
- The dissociation of the ions O_2^- and O_2^{2-} moved from the ceria surface to the catalytic surface by reverse spillover.

These oxygen atoms can then migrate from the catalytic surface to the ceria surface to oxidize Ce_2O_3.

The above spillover process plays a particularly important role at low temperatures where it is responsible for the occurrence of the oxygen storage process. Above 350 C, ceria is able to dissociate O_2, and the oxidation of the surface occurs via two parallel pathways: the direct oxidation of ceria by O_2 and the oxidation of ceria through spillover [22].

The above paragraphs only consider the oxidation of the ceria surface by O_2 or atomic O. Spillover is also involved in the oxidation of Ce_2O_3 by H_2O and NO, and the reduction of CeO_2 by CO, H_2, and HC. Indeed, CO*, H*, and HC* adsorbed on Pt reduce the ceria surface and NO* and H_2O* oxidize it through spillover at low temperatures. At high temperatures, the ceria surface is also directly reduced by CO, H_2, and HC, and directly oxidized by NO and H_2O.

The relative location of platinum and ceria particles in automotive washcoats enhances the important role of spillover. Indeed, during the impregnation process, platinum particles tend to be deposited close to the ceria particles [26].

Mostly surface ceria participates in the oxygen storage and release process. In particular, the reduction of the bulk ceria is thermodynamically unfavorable [24]. Thus, [27] shows that the surface oxygen stored in ceria undergoes reactions with the gaseous reactants at temperatures of about 500 C, whereas the bulk oxygen only participates in reactions for temperatures as high as 850 C. Nevertheless, reduction of the bulk ceria has been observed as low as 525 C but only after two hours of exposure to a reducing flow [24]. In that case, the ceria surface was first reduced and then the oxygen migrated from the bulk to the surface to even out the vacancy concentration. Hence, even though bulk ceria does participate in the oxygen storage reactions, the rate of these reactions is too slow to be relevant in usual catalyst operation.

3.2.3 Desorption

On supported metal catalysts, two types of desorption dominate under most conditions: simple molecular desorption and recombinative desorption [28].

During a simple desorption, the adsorbate simply detaches itself from the surface without undergoing significant change. This is the case for CO*: $CO^* \rightarrow CO + S$, and for NO* and H_2O*. This kind of desorption happens with molecules which are not too strongly bound to the surface. Indeed, a strongly bound molecule will fragment rather than desorb. Moreover, such desorption requires the earlier formation of a stable adsorbate.

In recombinative desorptions, two strongly bound adsorbates combine to form a molecule which immediately desorbs from the surface. This occurs because the newly formed molecule is not stable in the adsorbed form. This is the case for the formation of CO_2 through the reaction $CO^* + O^* \rightarrow CO_2 + 2.S$. A particular case is the recombinative desorption of two identical atoms such as O*, H*, and N*: $2.O^* \rightarrow O_2$.

3.3 Enhancements and inhibitions of the catalytic activity in TWCC

The previous sections have explained the main steps of the heterogeneous catalytic process in TWCC. They focused on the intrinsic catalytic activity of the converters. This activity is altered in two ways:

- Positively through the action of promoters present in the washcoat
- Negatively through the aging process, which leads to the progressive deactivation of the catalyzed washcoat.

3.3.1 Enhancement by metals-washcoat components interactions

As explained in Chapter 2, promoters are added to the washcoat to enhance the basic metallic catalytic activity. Cerium oxides are the major promoters. As already said, cerium oxides improve the performance of the TWCC under transient conditions by their oxygen storage capacity; they also stabilize the configuration of the catalytic particles and the washcoat. Moreover, they improve the activity of the PGM by direct interaction.

Nunan et al [26] show a consequence of the direct interaction: the synergistic action of the catalyzed washcoat surface ($Pt/Rh/CeO_2/Al_2O_3$), as illustrated on Figure 3.8. Here a fresh catalyst surface is to have the various oxides on it to be removed by hydrogen in the catalytic preparation process. The H_2 uptake rate is a measure of the action of this process.

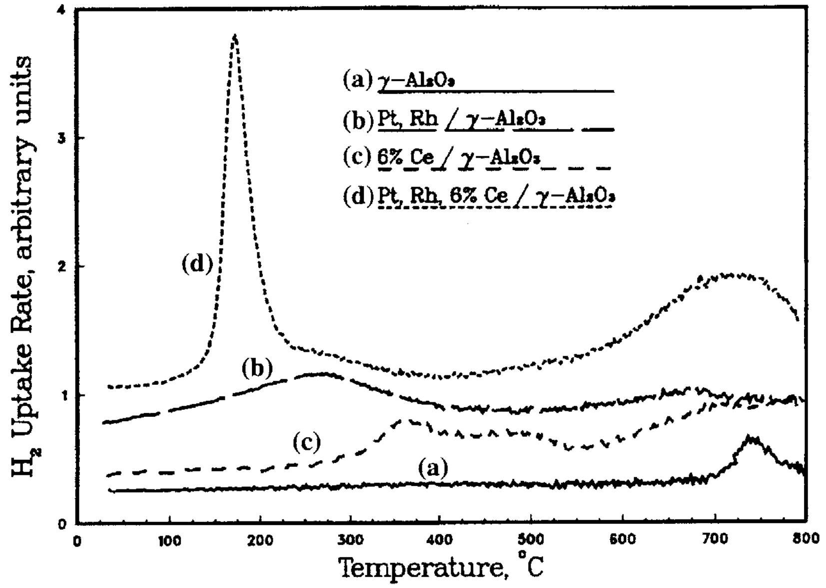

Fig. 3.8: *Comparison of the Temperature Programmed Reduction (TPR) for several catalyst compositions* [26]
(a) γ-Al_2O_3; (b) Pt, Rh/γ-Al_2O_3; (c) 6 wt % Ce/γ-Al_2O_3; (d) Pt, Rh, 6 wt % Ce/γ-Al_2O_3. Pt loading=0.77 wt %; Rh loading=0.04 wt %.

Figure 3.8 highlights two effects of the interaction between ceria and the noble metals:

- The barrier to removing the oxides of the noble metals is lowered: significant H_2 uptake by the noble metals starts at 175 C in the presence of ceria instead of 280 C without ceria.

  This effect is a result of the direct interaction between ceria and the noble metals [27]. In fact, the bond between any oxygen atoms and the noble metal is weakened due to the interaction between the metal and ceria. The adsorbed oxygen atoms are thus more active and can be reduced at lower temperatures (see Figure 3.9(a)).

- Ceria and the noble metals are synergistically reduced simultaneously

  As shown on Figure 3.8, the reduction of surface ceria normally occurs at about 350 C. In the presence of catalytic particles, surface ceria is reduced at 175 C and in larger amounts than alone. The catalytic particle activates the surface oxygen of the neighboring ceria particles, and easies its reduction via the spillover of the hydrogen atoms activated on the catalytic surface (see Figure 3.9(b)).

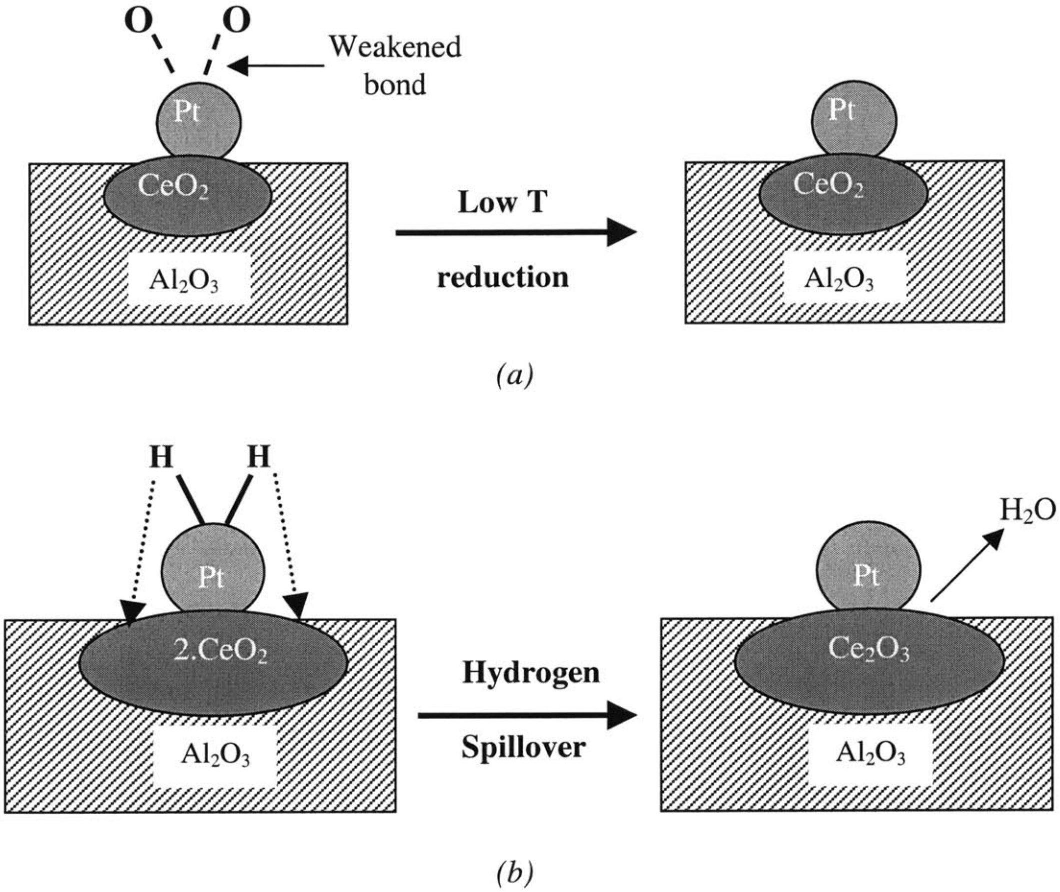

Fig. 3.9: *Modes of ceria-noble metal interaction in the synergistic reduction of the surface*
(a) Direct interaction; (b) Interaction through spillover

To summarize, the reduction example reveals two main modes of interaction between ceria and the noble metals: a direct mode of interaction increasing the activity of the reacting species (surface oxygen atoms on Pt and ceria), and an "indirect" mode of interaction involving the spillover process (see section 3.2.2 ii-).

Through these two modes of interaction, ceria also promotes the steam reforming reaction [29], the water-gas shift reaction, CO oxidation [26], and the reduction of NO by CO [30]. The promotion appears in the modification of the kinetics and selectivity of the reactions. For instance, in the presence of ceria, no N_2O is produced from the CO-NO reaction at low temperatures.

These favorable interactions occur when there is a large contact area between the noble metals and the ceria particles [26]. Platinum particles tend to deposit close to ceria, thus favoring the promoter action. Using small ceria particles constitutes another way of maximizing the interaction. Hence, ceria particles in fresh catalysts are typically less than 100 angstroms in diameter.

3.3.2 Aging

As TWCC age, three types of deactivation occur [12]:

- Thermal aging
- Poisoning
- Erosion of the washcoat

i- Thermally induced deactivation

During its operation, the catalyst can be exposed to temperatures greater than 850 C. This occurs for instance at the sudden braking after full load running of the vehicle, or during sustained engine misfiring caused by defects on the ignition module [31]. Exposure to such harsh environments causes thermal damage to the catalytic surface. Thermal aging leads to irreversible damages on the catalyst surface. These damages can be divided into two categories: sintering of the washcoat particles and undesirable interactions between the catalytic species and the carrier.

a) Sintering

1- Particle growth

The catalytic particles grow under high temperatures. In the fresh catalyst, the particles are small, about 20 to 30 angstroms in diameter, to obtain high dispersions. However, small particles are less stable than big ones and more mobile. Hence, particles tend to grow to form better defined and more stable crystals. In fact, the particles grow according to two mechanisms [15]:

- The migration of the small crystals and their coalescence upon collision.

- The Oswald ripening: small particles release atoms more easily than large ones, and migrating atoms are captured by large particles.

Hence, *Powell and Chen* [16] observed an average particle diameter of 96 angstroms for a 51680 km-old catalyst, whereas noble metal particles as small as 20 angstroms could be observed in the fresh catalyst.

The particles of the uncatalyzed washcoat also suffer from sintering. In particular, ceria forms larger crystals [24].

The growth of the catalytic and washcoat particles decreases the performance of the catalyst. Indeed, the number of available catalytic sites to the reactants decreases, as well as the oxygen storage capacity of the catalyst. Moreover, the contact area between the noble metals and the ceria particles is lowered; thus, the promoting interaction between the two species is decreased [27]. Furthermore, atoms in bigger particles are less reactive.

As already said in Chapter 2, the addition of stabilizers decrease the sintering rates by fixing the particles and reducing their mobility.

2- Carrier sintering

Thermal aging also leads to a gradual loss of the internal pore structure network of the carrier. Indeed, due to sintering, part of the pore openings becomes smaller, introducing more diffusional resistances to the reactions. Some of the pores even get closed, imprisoning catalytic sites. Thus, thermal aging decreases the surface area of the carrier.

Exposures to high temperatures can also lead to a conversion of the carrier into a new crystal structure. As represented on Table 3.1, the usual γ-Al_2O_3 structure can change to δ-Al_2O_3 or even θ-Al_2O_3. This conversion causes a decrease of internal surface area, from 150 to < 50 m^2/g for instance for the conversion γ-Al_2O_3 to δ-Al_2O_3.

Table 3.1: *Change in monohydrate alumina crystals as a function of temperature*

Temperature	< 500 C	500- 850 C	850-1050 C	1050- 1150 C	>1150 C
Form of the monohydrate alumina crystallite	Boehmite	γ -Al_2O_3	δ -Al_2O_3	θ -Al_2O_3	α -Al_2O_3

Again, the solution to prevent or rather delay these losses in activity is the use of stabilizers such as BaO, La_2O_3 (see Chapter 2).

b) Catalytic species-carrier interactions

Undesirable reactions that occur at high temperatures and not under usual catalytic converter conditions also decrease the activity of the catalyst. For example, Rh_2O_3 can react with Al_2O_3 above 800 C to give $Rh_2Al_2O_4$, the catalytic performance of which is inferior to Rh especially for NOx reductions [12].

Ceria can also react with alumina to form cerium aluminate $CeAlO_3$, which decreases the ceria surface area [24]. To reduce this loss, two kinds of dopants can be added to the washcoat:

- Cations of lower oxidation number than Ce^{4+}, like Ca^{2+}, can be introduced in the ceria lattice; they create oxygen vacancies that increase the oxygen bulk diffusion rate and thus the oxygen storage capacity.
- ZrO_2 can be added to ceria to form a solid solution CeO_2-ZrO_2, which increases the thermal stability of the ceria surface.

ii- Poisoning

The second most common cause of deactivation occurs because of contaminants present in the exhaust stream that deposit on the catalytic sites. This poisoning can be selective, when the contaminant reacts with the catalytic site, or non-selective through masking or fouling of the catalytic sites.

a) Selective poisoning

In the case of selective poisoning, the chemical contaminant reacts with the catalytic site or the carrier, thus making it less active and even sometimes completely inactive.

For instance, these reactions can lead to the formation of catalytically inert alloys between impurities such as Pb, Hg, or Cd and the noble metals.

Sulfur -- one of the fuel impurities-- is also a strong poisoning agent. Indeed, it reacts with the catalytic sites and thus blocks them. Furthermore, sulfur hinders the oxygen storage capacity of the catalyst ([24], [32]). In fact, under oxidizing conditions, ceria stores sulfur under the form of cerium sulphates, which then decompose and react with H_2 under reducing conditions to produce the pollutant H_2S. Sulfur can also react with alumina to form compounds such as $Al_2(SO_4)_3$, which can lead to pore obstruction, and thus increase diffusional resistances.

Poisoning also occurs with lead initially contained in the fuel and oil additives like zinc and phosphorous.

Fortunately, unlike thermal deactivation, poisoning is reversible. Indeed, the contaminants can be removed by heat treatment or washing. The contaminants can also be eliminated from their source: for example, the sulfur and lead levels of the fuel are being lowered.

The design of the catalyst can also decrease the sensitivity of the surface to poisoning. Cerium oxides for example decrease the poisoning by sulfur and lead of the noble metals when present under the form of small particles. In particular, special attention is given to the design of palladium-containing monoliths since palladium is the most sensitive noble metal to poisoning ([33], [34]).

b) Non-selective poisoning

Aerosols or high molecular weight materials from engine exhaust can physically deposit onto the surface of the catalyst. This type of deactivation is often referred to as fouling or masking. The deposits hide part of the catalytic sites, resulting in a decrease in geometric area and so in a loss of total achievable conversion. They can also deposit inside the pores and partially block them. This type of deposition is non-selective and involves physisorption of the contaminants on the washcoat surface.

In TWCC, examples of masking poisons are Fe, Ni, Cr… from corrosion, silica and alumina containing dusts, and phosphorous from lubricating oils.

iii- Washcoat loss

The surface of the monolith is exposed to harsh conditions of high vibration levels, gas flowing at high velocities, and rapidly varying temperatures. The monolith components are thus exposed to substantial mechanical and thermal stresses. The washcoat and the substrate are made out of different materials with different thermal expansion coefficients. Hence, they react differently to the stresses, and may fracture and lead to loss of materials.

This material loss decreases the total achievable conversion of the monolith.

To lessen these problems, binders such as SiO_2 can be added to the washcoat formulation to improve the chemical bond between the washcoat and the SiO_2-containing ceramic substrate. In the case of metallic substrates, the surface can be pretreated, as already explained in Chapter 2.

Chapter 4: Modeling of the monolithic catalyst

A one-dimensional fully transient model of a TWCC was formulated based on the review reported in Chapters 2 and 3. Only the monolith was modeled, which excludes the insulation layers, the inlet pipe, the diffuser, the exit pipe, and the nozzle. This chapter discusses the assumptions and approximations used in the modeling approach.

4.1 Main features of the model

4.1.1 Assumptions

i- One-dimensional model

The use of a diffuser before the monolith could result in a non-uniform distribution of the flow at the catalyst inlet [24]. Indeed, more flow passes through the center channels of the monolith than through its peripheral channels, due to separation of the flow on the diffuser walls. A one-dimensional model neglects this flow non-uniformity. In fact, it assumes that all channels in a cross-section of the monolith are identical.

We neglected these flow effects since our model was primarily meant to focus on the modeling of the transport and chemical reactions, as we shall see later. The good converter simulations obtained by previously developed one-dimensional models seem to validate this assumption.

Thus, with this one-dimensional approach, only one channel needs to be modeled.

ii- Geometrical assumptions

The model applies to ceramic monoliths of any form of channel cross-section. Now, as explained in section 2.2.2, the washcoat is unevenly deposited on the walls of square channels. To simplify the model and adapt square channels to the one-dimensional assumption, the washcoat was considered to be evenly deposited whatever the form of the channel. In the case of square channels, the constant thickness is computed as the average between the actual side and corner thicknesses.

iii- A single solid phase

The substrate and washcoat were treated as one single solid phase with uniform properties (density, conductivity, and heat capacity) and temperature. The properties of the resulting solid phase were computed by weighted averages of the properties of the washcoat and substrate based on their weight percentages. The assumption of a uniform temperature will be discussed later on in section 4.3.

iv- Flow treatment

The flow was considered as the sum of a one-dimensional main flow and boundary layers, as represented on Figure 4.1.

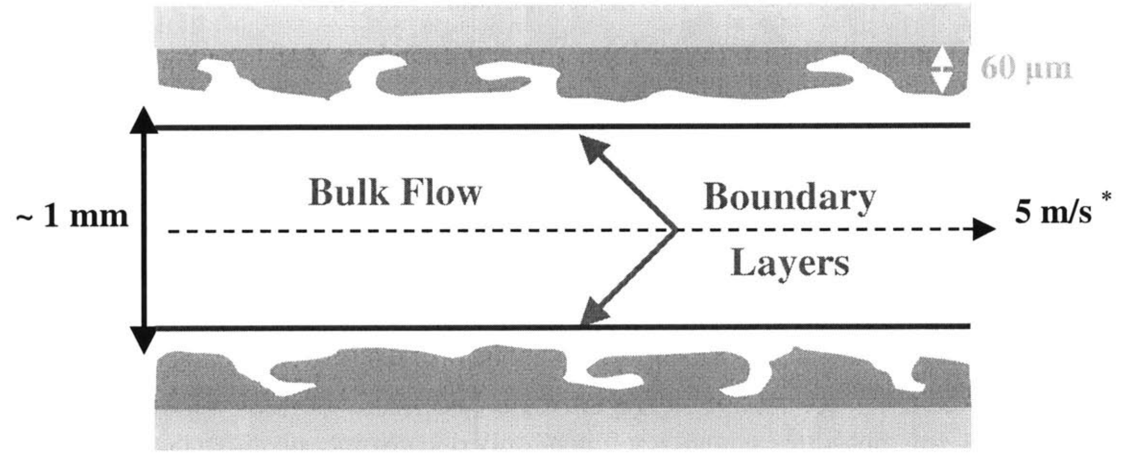

Fig. 4.1: *Flow representation in the modeled monolith channel*
(*at 1600 rpm, 0.5 bar intake pressure)

This assumption will be discussed in more detail in section 4.3.2.

v- Pressure considerations

In all the computations, the pressure was considered constant at 1 bar.

4.1.2 Modeled processes

The model accounts for the three following main processes:

- The transport of energy and mass between the wall and the mean stream

  Figure 4.2 illustrates the two main kinds of transport to be modeled:
  - *The macroscopic transport or external diffusion* (see Figure 4.2(a)), which corresponds to the diffusion of energy and mass between the bulk flow and the surface of the catalyst.
  - *The microscopic transport or internal diffusion* (see Figure 4.2(b)), which corresponds to the diffusion of energy and mass inside the pores of the washcoat.

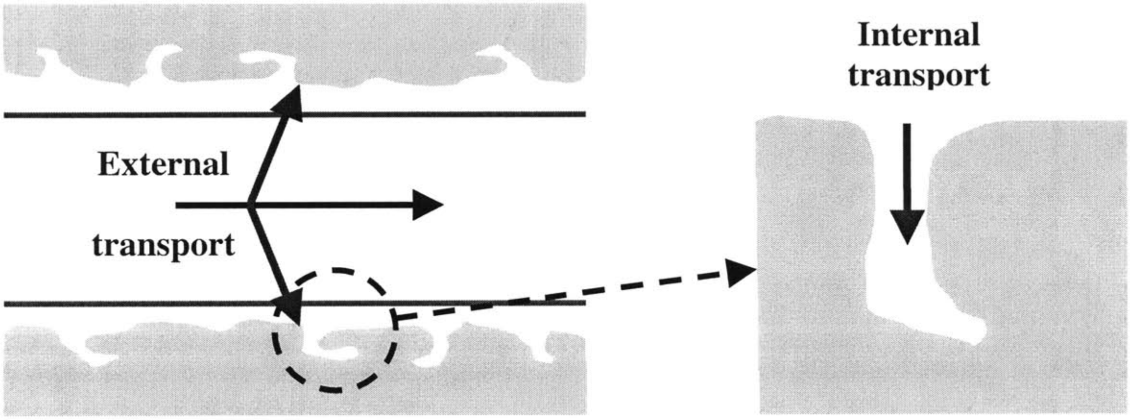

(a) *(b)*

Fig. 4.2: *Transport processes occurring in the monolith channels (a) External transport; (b) Internal transport*

- The catalytic reactions
- The oxygen storage process

The oxygen storage process has to be accounted for to simulate the good performance of the catalyst under transient conditions. The next section discusses why the transport and chemical processes also have to be considered.

4.2 Limiting processes

The chemical reactions and the transport processes all need to be accounted for to simulate the behavior of the catalyst on a wide range of temperatures. Indeed, each of these processes limits the overall catalytic process in a specific range of temperatures.

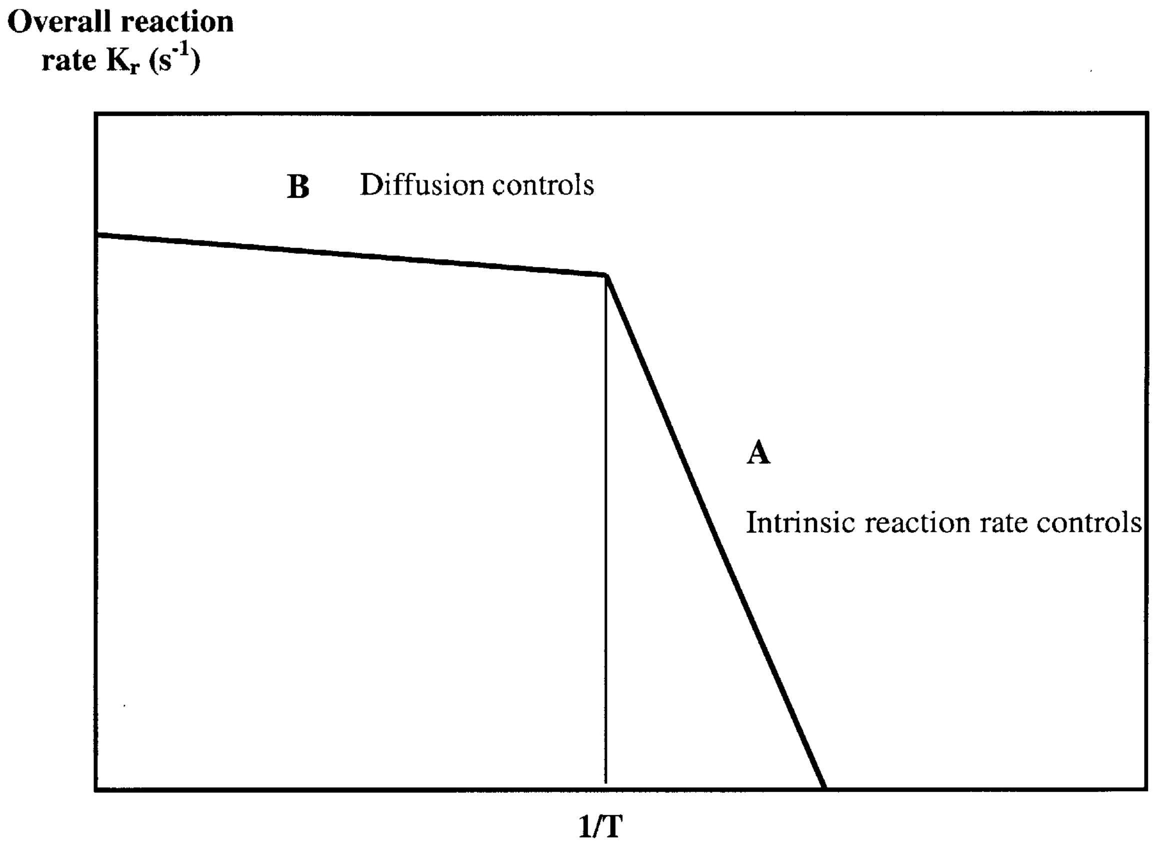

Fig. 4.3: *Possible kinetic regimes in a gas phase reaction occurring on a porous solid catalyst*

As revealed on Figure 4.3, a heterogeneously catalyzed reaction by a porous catalyst shows two overall conversion regimes as the temperature increases. At low temperatures (region A), the chemical reactions control the overall catalytic process. In fact, the reaction characteristic time is larger than the external and internal diffusion times, and thus the reactions limit the speed of the overall process. As the surface temperature increases, the reaction rates increase exponentially and thus the chemical processes become faster than the diffusion times: the heterogeneous catalysis process enters region B and thus becomes diffusion limited.

To further illustrate this behavior, let us compare the characteristic times of the external diffusion, internal diffusion, and catalytic reactions at different temperatures in the oxidation of CO.

The characteristic times for each of the considered processes are defined below.

- External transport

The characteristic time of the external diffusion process is the time a species takes to diffuse from the middle of the channel to the surface of the washcoat. Thus, this characteristic time can be computed as $\frac{d^2}{4 \cdot D_m}$, where D_m is the molecular diffusivity of the slowest diffusing reactant in m^2/s and d is the diameter of the channel in m.

In our example, O_2 diffuses faster than CO, thus the external transport characteristic time is determined by the diffusivity of CO.

The calculations are detailed in Appendix A. For a cell size d of 1 to 2 mm, the typical external diffusion time is a few milliseconds. Note that, under typical engine conditions, this is much less than the flow through time of 10 to 100 ms (depending on the engine operating conditions).

- Internal transport

The internal diffusion process includes two characteristic times:

- The characteristic time of the diffusion along the pore $t_1 = \frac{l^2}{D_{eff}}$, where l is the length of the considered pore in m and D_{eff} the effective diffusivity of the diffusing species in m^2/s(see below).
- The characteristic time of the diffusion across the pore $t_2 = \frac{d_p^{\ 2}}{D_{eff}}$, where d_p is the diameter of the considered pore in m.

Because of the range of pore sizes, the transport is in a mixture of the continuum and Knudsen regimes. Therefore, the above two characteristic times involve the effective diffusivities of the reactants. Unlike the molecular diffusivity, the effective diffusivity accounts for the structure of the porous catalyst. In particular, for a given type of pore, the effective diffusivity depends on the pore diameter, the porosity of the washcoat in this particular type of pores, and the deviation of the pore from the cylindrical shape characterized by the tortuosity factor. Appendix A gives more information on its computation and on these dependences.

To compute the time across the pore, the diffusivity was evaluated in the continuum region, which is valid for pore-radius-to-mean-free-path ratios greater than 1. This continuum region thus includes pores larger than several hundred angstroms depending on the temperature and considered diffusing species -- 517 angstroms for CO at 300 K. To compute the time along the pore, the diffusivity was evaluated using the general formula for the whole range of diffusivities accounting for both the continuum and the Knudsen diffusion regimes.

The characteristic time across the pore was computed for the dominant macropores of a typical bimodal pore distribution. The computation of the time scale along the pores assumes a largest possible pore length of 100 μm, according to the thickness of the washcoat in the corners of a square channel.

Appendix A details all these assumptions and calculations.

- Catalytic reactions

As will be explained in more details in section 4.4, the catalytic reactions are modeled by a set of elementary reactions of adsorption, desorption, and surface reactions. For instance, the reaction we are considering here, $CO + 0.5 \cdot O_2 \leftrightarrow CO_2$, is equivalent to the three following elementary steps:

$$\begin{cases} O_2 + 2 \cdot S \leftrightarrow 2 \cdot O^* (1) \\ CO + S \leftrightarrow CO^* (2) \\ CO^* + O^* \leftrightarrow CO_2 \ (3) \end{cases}$$

In such elementary reactions, S represents an available catalytic site and the superscript * refers to adsorbed species.

The characteristic reaction time for this mechanism is defined as the characteristic time for the production of CO_2. Hence, the reaction time is the characteristic time of the slowest reaction among the elementary steps of the considered chemical mechanism. In other words, one must determine which step is rate limiting: the adsorption of CO, the adsorption of O_2, or the surface reaction producing CO_2.

The definition of the characteristic time of an elementary step depends on the nature of the considered reaction.

For an adsorption reaction, the time scale characterizes the time needed for the concentrations of adsorbing reactant and adsorbate to reach a steady state. Figure 4.4 shows the typical decrease in gaseous reactant concentration due to adsorption (in light color). Graphically, the adsorption characteristic time is computed from the origin tangent to the curve (in black on the figure). Theoretically, the concentration of CO, for example, decreases according to the following ordinary differential equation: $\frac{d[CO]}{dt} = k_{f_2}.[CO][S]$, where [S] is the concentration of vacant sites on the surface, and k_{f2} the kinetic constant for CO adsorption. Hence, the adsorption characteristic time for CO is $\tau_{ads,CO} = \frac{1}{k_{f_2}.[S]_0}$, where $[S]_0$ is the initial concentration of vacant sites, i.e. the total concentration of catalytic sites on the surface.

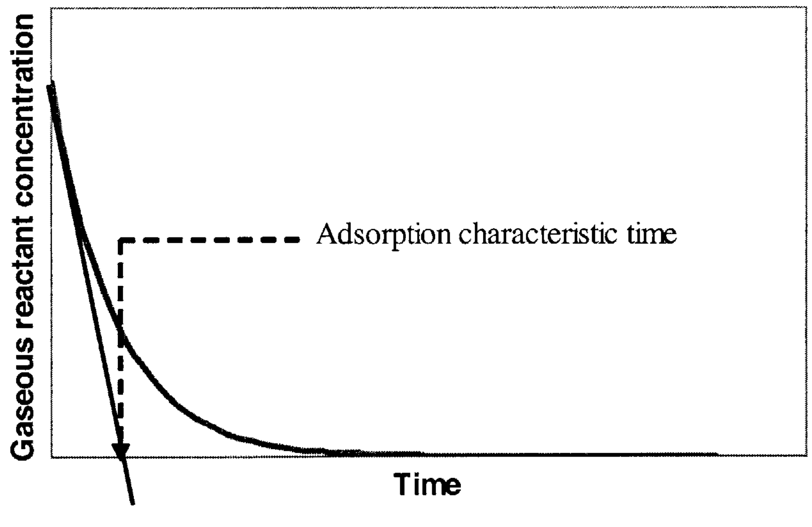

Fig. 4.4: *Concentration of an adsorbing reactant as a function of time*

Unlike CO, O_2 adsorbs dissociatively on the surface. Thus, its adsorption time scale is a bit different: $\tau_{ads,O_2} = \frac{1}{k_{f_1}.[S]_0^2}$, where k_{f1} is the kinetic constant for O_2 adsorption; but the reasoning behind the formula is the same (see Appendix A for more details).

For surface reactions, the time scale refers to the time needed to consume the reactants when the surface composition initially is in equilibrium. For instance, CO* disappears through the surface reaction according to the following equation: $\frac{d[CO^*]}{dt} = -k_{f_3}.[CO^*][O^*]$. Hence, the characteristic time for its disappearance is $\tau_1 = \frac{1}{k_{f_3}.[O^*]}$. As can be seen, this time constant depends on the level of O* on the surface. By convention, the calculation of the surface reaction time scale uses the value of [O*] at equilibrium. In fact, the ordinary differential equation for O* defines another time scale: $\tau_2 = \frac{1}{k_{f_3}.[CO^*]}$, different from the previous one. The characteristic time of the surface reaction is defined as the maximum of (τ_1, τ_2) computed at equilibrium.

The required equilibrium concentrations of [O*] and [CO*] were computed from the equilibrium constants of the reactions (see Appendix A).

Table A.1 gives the results of all the time computations. The next paragraphs comment on the main trends that could be highlighted.

- **Chemical time constants**

Table 4.1 gives the characteristic times of the three elementary steps of the CO-O_2 mechanism at 4 representative temperatures.

Table 4.1: *Time scales of the elementary steps in the CO-O_2 mechanism*

Temperature (K)	$\tau_{\text{ads CO}}$ (s)	$\tau_{\text{ads O2}}$ (s)	τ_{surface} (s)
300	$6.08.10^{-7}$	$8.54.10^{-6}$	255075
500	$4.71.10^{-7}$	$1.41.10^{-5}$	0.104
800	$3.72.10^{-7}$	$2.25.10^{-5}$	$2.452.10^{-5}$
1000	$3.33.10^{-7}$	$2.80.10^{-5}$	$1.56.10^{-6}$

These numbers show that surface reaction 3 constitutes the rate limiting step of the CO-O_2 mechanism for temperatures less than about 800 K. Among the adsorption reactions, O_2 adsorption then becomes rate limiting. Figure 4.5 below further illustrates this change in rate limiting step.

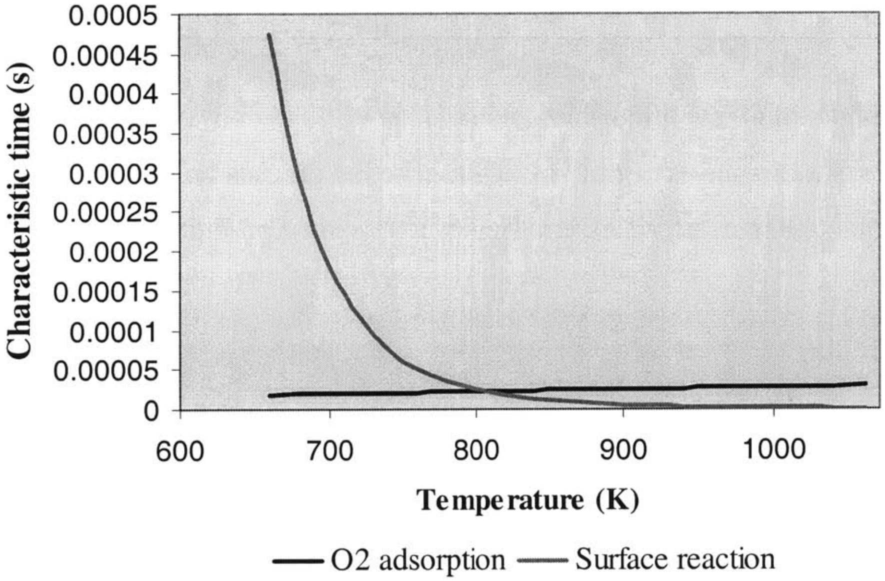

Fig. 4.5: *Characteristic times of O_2 adsorption and CO*-O* surface reaction versus temperature*

Figure 4.5 also shows the exponential variation of the surface reaction time scale with temperature. On the contrary, the effect of temperature on the adsorption times is rather weak. These differences in temperature sensitivity are responsible for the change in rate limiting step.

- **Characteristic time of the heterogeneous catalytic process**

Table 4.2 below summarizes the characteristic times of the three main processes involved in the heterogeneous catalysis for different temperatures.

Table 4.2: *Time scales of the transport and chemical processes*

Temperature (K)	External transport time (s)	Internal transport time (s)		Reaction time (s)
		Across pore	Along pore	
400	$1.83.10^{-2}$	$1.55.10^{-14}$	$1.84.10^{-2}$	26.19
550	$9.95.10^{-3}$	$8.42.10^{-15}$	$1.5.10^{-2}$	$1.4.10^{-2}$
800	$5.2.10^{-3}$	$4.41.10^{-15}$	$1.2.10^{-2}$	$2.25.10^{-5}$

These numbers illustrate three phenomena.

- The kinetic reactions limit the heterogeneous process below 550 K; then the internal transport becomes limiting, as represented on Figure 4.6 below.

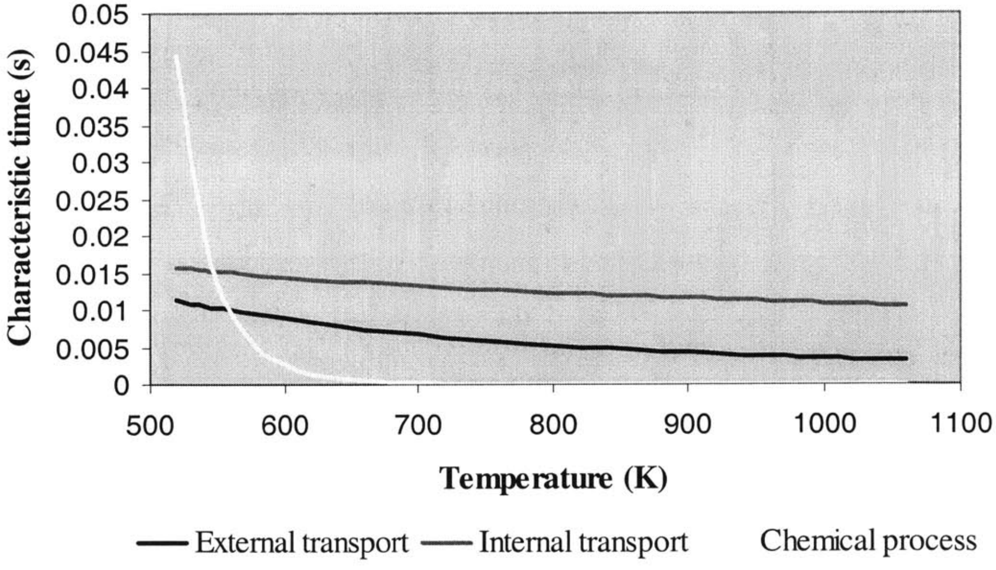

Fig. 4.6: *Characteristic times of the chemical and transport processes versus temperature*

Once again, we see that the exponential decrease of the reaction time with increasing temperature is responsible for the change in kinetic regime.

- The internal transport across the pores is very fast. Species concentrations can thus be considered constant in a pore cross-section.
- The external diffusion, even if not limiting of the whole catalytic process, is slow compared to the chemical reactions and of a comparable order of magnitude than the internal transport.

Hence, the computed time scales illustrate the existence of the two kinetic regimes evoked before and explain why all three processes must be accounted for. In particular, the kinetic reactions are limiting at low temperatures and thus are essential to simulate the warm-up of the monolith, whereas under steady-state operation (high temperatures), the internal transport is limiting.

4.3 Transport modeling

4.3.1 Internal transport

As explained in the previous section, the internal transport becomes limiting at intermediate temperatures, and thus needs to be modeled. By lack of time, we did not develop our own model but used and adapted the modeling approach and results of *Hayes and Kolaczkowski* [39]. This section first reviews the internal diffusion problem and the general modeling approach. The used model is then detailed.

i- The effectiveness factor

Above about 600 K, the internal diffusion process along the pores limits the heterogeneous catalytic process. In particular, the gaseous reactants react faster than they diffuse. This leads to a non-uniform concentration profile inside the pore as represented on Figure 4.7: the reactants concentrations decrease as the mixture diffuses inside the pore.

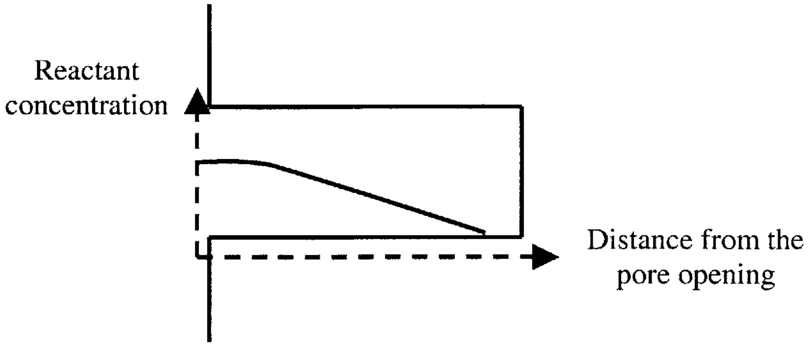

Fig. 4.7: *Non-uniform concentration profile inside a pore under internal transport limitation*

These diffusional effects decrease the performance of the converter. Indeed, the catalytic particles deposited near the end of the pore are exposed to very poor reactant levels, and thus are not efficiently used. In fact, depending on the difference between the chemical and diffusional time scales, the reactants can even be completely consumed before the end of the pore. In this particular case, part of the catalytic area is unutilized.

This loss in catalytic activity is generally modeled through an effectiveness factor:

$$\eta = \frac{\text{average rate of reaction in the washcoat}}{\text{rate evaluated at surface conditions}}$$

Computing the average rate of reaction in the washcoat requires the calculation of the concentration profiles inside the pores. This point will be further detailed in the next section about the internal transport model we used.

The effectiveness factor decreases with increasing surface temperature, i.e. the diffusional resistances become more important (relative to the surface reaction time) with increasing temperature. It also depends on the geometry of the considered porous material (spherical pellet, cylinder, or slab for example) and on the concentrations of reactants at the surface. Furthermore, the effectiveness factor depends on the considered species since it traduces diffusional effects.

The internal diffusional limitations not only affect the concentration profiles but also the temperature profile inside the pores. Indeed, as the mixture flows inside the pore, less reactants are available for reactions; the catalytic activity thus decreases towards the end of the pore, which results in a non-uniform heat release from the reactions. Therefore, like the reactants concentrations, the temperature decreases along the pore.

This non-uniform temperature profile is characterized by the Prater number $\beta = \frac{\Delta T_{max}}{T_s}$, where ΔT_{max} is the maximum variation of temperature along the pore and T_s the surface temperature. However, as explained in [39], the washcoats used for automotive applications can be considered as isothermal. Hence, the solid phase can be characterized by a single uniform temperature T_s, as announced in section 4.1.

Figure 4.8 below summarizes the internal transport modeling approach. As explained in the previous paragraphs, the porous structure shows non-uniform concentration profiles along its pores. In the modeling, the effectiveness factor lumps these concentration profiles as well as the pore structure in its expression. In fact, the surface is modeled as a flat non-porous surface -- of the same internal surface area as the real one -- exposed to uniform reactants concentrations. The pore distribution is included in the calculations of equivalent reaction rates: $\eta.\ R(c_s, T_s)$.

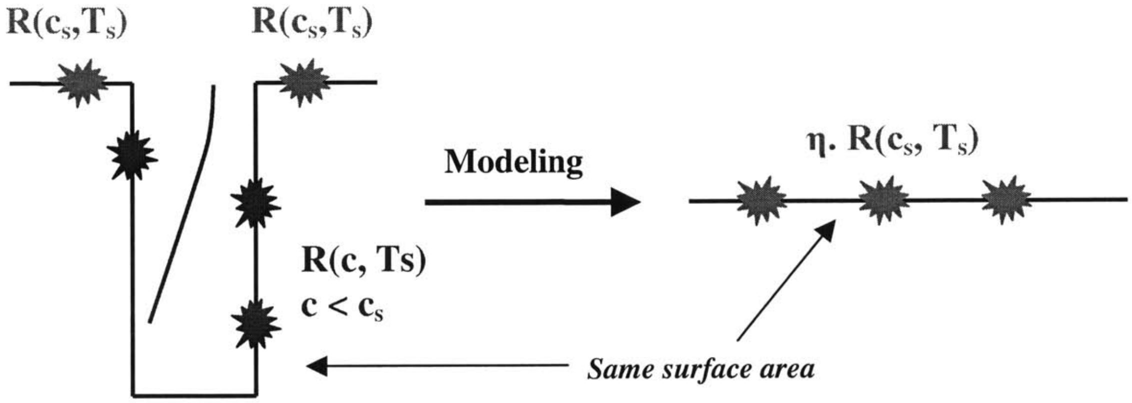

Fig. 4.8: *Internal transport modeling principle*

ii- Current model

Most models of catalytic converters do not account for the internal transport explicitly, but lump it in global rate expressions determined experimentally, as explained in Chapter 1. Nevertheless, as early as 1971, *Kuo et al* [40] included effectiveness factor calculations in their model of an oxidation pelleted catalyst. *Cai and Collings* [41] computed the effectiveness factor for a monolith, assuming a slab geometry, and showed that better predictions can be obtained with an explicit internal diffusion model than with a diffusion-lumped model. Two more recent models accounting for internal diffusion were produced: *Edvinsson and Cybulski*'s [42] and *Hayes and Kolaczkowski*'s [39] models. *Edvinsson and Cybulski* do not model a reactor for automotive use, but they consider reactors similar to catalytic monoliths in geometry.

The two latter models use the same general method:

- they account for the uneven thickness of a washcoat in square cross-section channels
- they compute the concentration profiles numerically from the steady transport equation inside the pores: $\nabla(D_{eff}.\nabla c_i) - R(c_i, T_s) = 0$, where c_i refers to the concentration of species i and R is its rate of disappearance. This equation balances the diffusion and the reactions inside the pores (the transport inside the pores is essentially due to diffusion, the convective velocity inside the pores being negligible).

However, the overall model of *Hayes and Kolaczkowski* is closer to our model, especially regarding the external transport modeling, and thus easier for us to adapt. Therefore, we chose to use their computations of the effectiveness factor.

Hayes and Kolaczkowski studied the evolution of the effectiveness factor for two reactions: the oxidations of CO and propane. As already said, they considered a monolith with square channels and computed η from the concentration profiles in its non-uniform washcoat by a 2D finite-element method. In their calculations, they used global rate expressions. Moreover, they had to assume a pore distribution to determine the effective diffusivity. Since they were missing information about the actual pore distribution of their modeled washcoat, they used the results from the random pore model detailed in *Oh and Cavendish* [43]. The random pore model divides the pores in micropores and macropores and represents the diffusion flux as being the sum of the flux through the macropores alone, the flux through the micropores alone, and the flux by a series diffusion through both [38].

They obtained the following results:

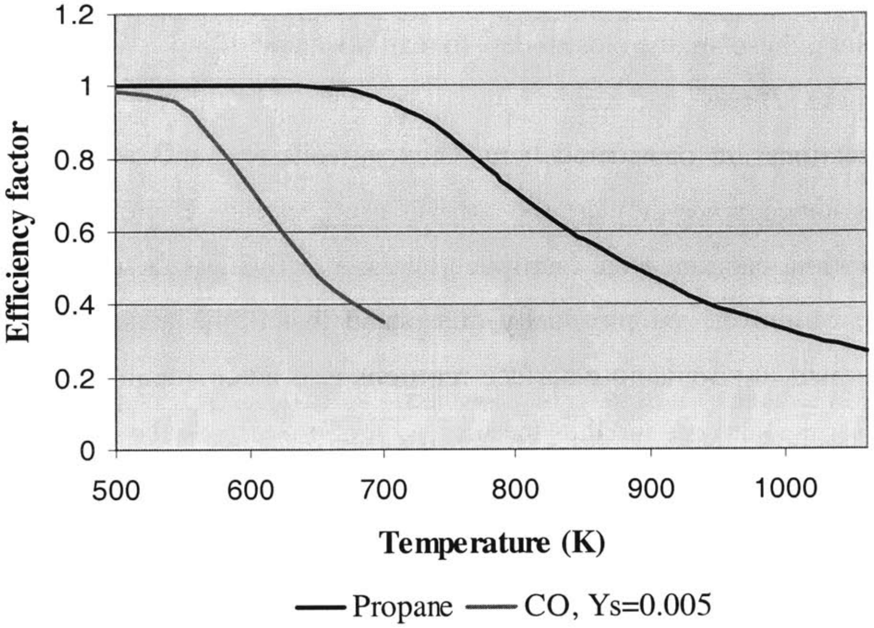

Fig. 4.9: *Effectiveness factor versus solid temperature for the oxidations of propane and carbon monoxide*

Figure 4.9 above shows that the effectiveness factor can be as low as 0.3 above 700 K. The assumption of negligible diffusional effects is thus not valid in automotive converters. Moreover, it illustrates that the effectiveness factor strongly depends on the considered species.

The above model considers the same geometry as ours, and is even more precise than our model in its 2D approach. On the other hand, it just computes the effectiveness factors for two reactions highlighting a big difference between the two. However, propane oxidation rate is low compared to CO oxidation rate, propane being a slow oxidizing HC. Hence, even though the effectiveness factor does depend on the considered species, the dependence is not as important as it appears on Figure 4.9.

Propane is not included in our model. Moreover, the included species have diffusivities close to CO diffusivity, and their rate of reaction can be assumed to be closer to CO oxidation rate than to propane oxidation rate.

Therefore, in the model, we neglected the differences between the reactions and considered an identical effectiveness factor for all the included reactions. Thus, we used the curve of the effectiveness factor versus temperature for CO oxidation for a surface

CO fraction of 0.005%. CO levels encountered in automotive catalysts are higher than that; nevertheless, these are the closest data to reality we could find.

Furthermore, *Hayes and Kolaczkowski* use global kinetic rate expressions while elementary reactions are considered here. Only gaseous reactants are affected by the diffusional resistance, since they are the only diffusing species. Therefore, in the model, only the adsorption reactions were multiplied by the effectiveness factor from *Hayes and Kolaczkowski*. Moreover, we physically understand that if the adsorption of gaseous reactants is limited, the remaining surface reactions also automatically are because less adsorbates cover the surface; and thus the formation of products is also affected.

This aspect of the problem reveals the inaccuracy of the use of global rate expressions. Indeed, using global rate expressions leads to the computation of an effectiveness factor per reaction, whereas the detail of the elementary reactions shows that more rigorously we should compute an effectiveness factor per adsorbing species. We used *Hayes and Kolaczkowski*'s numbers to be able to account for the important internal diffusion process. Obtaining more precise effectiveness factors would require the development of a model adapted to the set of elementary reactions.

4.3.2 External transport

Unlike the internal transport which principally affects the mass transfer in automotive catalysts, both the external transport of mass and energy need to be modeled.

i- Assumptions

The external transport modeling involves the following assumptions:

- The homogeneous reactions in the gas phase are neglected since the operating temperatures of the system are not high enough.
- The axial diffusion in the gas phase is negligible compared to the flow convection.

  Indeed, in a typical monolith channel, the gases are convected at a velocity $v = 5$ m/s, the channel length is about $L = 17$ cm, and the axial dispersion coefficient (by Taylor diffusion) of the gases, taken as that of the dominant species N_2, is about $1.3.10^{-3}$ m^2/s at 800 K. Hence, the Peclet number, which compares the axial diffusion time and the convection time, is: $\mathrm{Pe} = \frac{\text{diffusion time}}{\text{convection time}} = \frac{v.L}{D_i} = 653$. Thus, the gaseous reactants are convected much faster than they diffuse, and diffusion can be neglected.

- The axial thermal conduction in the gas phase is also negligible compared to convection.

  Indeed, for gas molecules, conduction and diffusion are governed by the same mechanism. Hence, the thermal diffusivity and the diffusivity are of the same order of magnitude, as expressed by the Lewis number $\mathrm{Le} = \frac{\lambda_g}{\rho_g.Cp_g.D_i} \approx 1$, in which λ_g, Cp_g, and ρ_g are the thermal conductivity, heat capacity, and density of the gaseous mixture, respectively. Thus conduction is negligible compared to convection.

- The heat losses to the ambient are evenly distributed among all individual channels.

  In a real monolith, the peripheral channels lose heat to the surrounding ambient air. Because of this, and also of the flow non-uniformity at the inlet of the catalyst, two neighboring channels are not exactly at the same temperature and exchange energy. As explained previously, the flow non-uniformity is neglected in the one-dimensional model. Yet, to account for these heat exchanges, the heat losses to the ambient were included in the model. They were considered equally due to all individual channels. Only the heat losses by convection were accounted for.

ii- External mass transfer

With the above assumptions, Figure 4.10 represents the fluxes in a slice of monolith channel between x and x+dx.

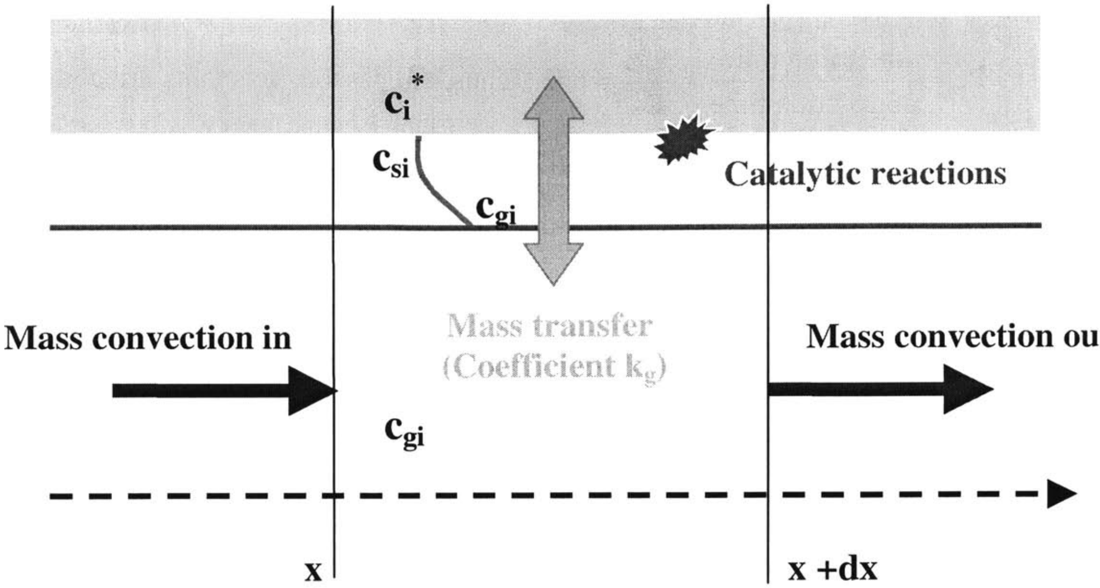

Fig. 4.10: *Mass transport fluxes on a slice of monolith*

The main fluxes are:

- The axial convection of mass in the bulk flow
- The mass transfer through the boundary layer
- The consumption and production of mass by the catalytic reactions

The modeling of the catalytic reactions is the object of section 4.4.

The mass transfer between the bulk flow and the boundary layer results in the formation of a boundary layer concentration profile. Indeed, the gaseous reactants have to diffuse from the bulk flow to the surface of the catalyst, which results in a decrease in concentration as we come closer to the surface, as illustrated on Figure 4.10. Rather than looking at the detail of the boundary layer, the mass exchange was modeled by a film approach including mean bulk concentrations c_{gi} and solid-gas interface concentrations c_{si}. In this approach, the whole profile is lumped into the mass transfer coefficient k_g. This coefficient will be further discussed in section 4.3.2 iv-.

Thus, three types of transport equations result from these fluxes: one for the gaseous reactants in the bulk flow, one for the gaseous reactants close to the surface, and one for the adsorbates. These equations simply balance the mass fluxes and accumulation of mass in a slice of monolith.

a) Transport equation for the bulk gaseous reactants

The balance of fluxes in the gas phase can be written:

Accumulation of mass = convection in - convection out - mass transfer to the surface.

Or, in mathematical terms:

$$\varepsilon \cdot V \cdot \frac{dc_{g,i}}{dt} = v \cdot A \cdot c_{g,i}\Big|_{x} - v \cdot A \cdot c_{g,i}\Big|_{x+dx} - k_g \cdot A_{ap} \cdot \left(c_{g,i} - c_{s,i}\right) \tag{4.1}$$

where $c_{g,i}$ is the concentration of species i in the bulk flow in mol/m^3

$c_{s,i}$ is the concentration of species i at the gas-solid interface in mol/m^3

ε is the void fraction of the monolith (consistent with the definition of A)

V is the monolith volume in m^3 between position x and x+dx

A the monolith channel cross section in m^2 (including the washcoat)

A_{ap} is the apparent internal surface area of the washcoat in m^2 (see Figure 4.11)

v the velocity of the flow in m/s

k_g is the mass transfer surface velocity in m/s

Assuming the velocity stays constant along a channel, Equation (4.1) can be simplified to:

$$\varepsilon \cdot V \cdot \frac{dc_{g,i}}{dt} = -v \cdot A \cdot \Delta x \cdot \frac{dc_{g,i}}{dx} - k_g \cdot A_{ap} \cdot \left(c_{g,i} - c_{s,i}\right) \tag{4.2}$$

Or, by dividing by V:

$$\boxed{\varepsilon \cdot \frac{dc_{g,i}}{dt} = -v \cdot \frac{dc_{g,i}}{dx} - k_g \cdot S \cdot \left(c_{g,i} - c_{s,i}\right)} \tag{4.3}$$

where $S = \frac{A_{ap}}{V}$ is the gas-solid interface area per unit volume in m^{-1}, or apparent area per unit monolith volume.

b) Transport equations for the reactant close to the surface

We performed a similar mass balance for the gas-solid interface concentrations looking at the detail of the surface between x and x+dx. Figure 4.11 illustrates the considered geometry. In this case, the balance of the transport fluxes gives:

$$V^* \cdot \frac{dc_{s,i}}{dt} = k_g \cdot A_{ap} \cdot \left(c_{g,i} - c_{s,i}\right) - A^* \cdot \sum_{j=1}^{N_i} R_j\left(\overline{c_s}, \overline{c^*}, N_{s0}, T_s\right) \tag{4.4}$$

where V^* is the void volume or volume occupied by the gases close to the surface in m^3, (thus, V^* is the pore volume)

A^* is the actual internal surface area in m^2

$\overline{c*}$ is the vector of adsorbate concentrations c_i^*, expressed in mol/m^2 of actual surface area

N_{s0} is the number of catalytic sites per m^2 of actual internal surface area, which depends on the loading and dispersion of the noble metals in the monolith

$\sum_{j=1}^{N_i} R_j\left(\overline{c_s}, \overline{c*}, N_{s0}, T_s\right)$ is the apparent rate of consumption of species i expressed in $mol/m^2.s$ for the equation to be homogeneous. N_i is the total number of reactions involving gaseous species i. The adjective "apparent" modifying the rate refers to the multiplication by the effectiveness factor of the adsorption reactions. This effective factor is necessary because in general, the gas species concentration c_s is non-uniform in the pore cavity so that the local concentration at the catalyst site may not be equal to c_s (the latter is true when the reaction rate is slow compared to the diffusion time within the pore). The rates of elementary reaction j, R_j, depends on the surface temperature T_s, on the vectors of gaseous surface concentrations $\overline{c_s}$ and adsorbates concentrations $\overline{c*}$, and on the total number of catalytic sites on the surface, as will be detailed in section 4.4.

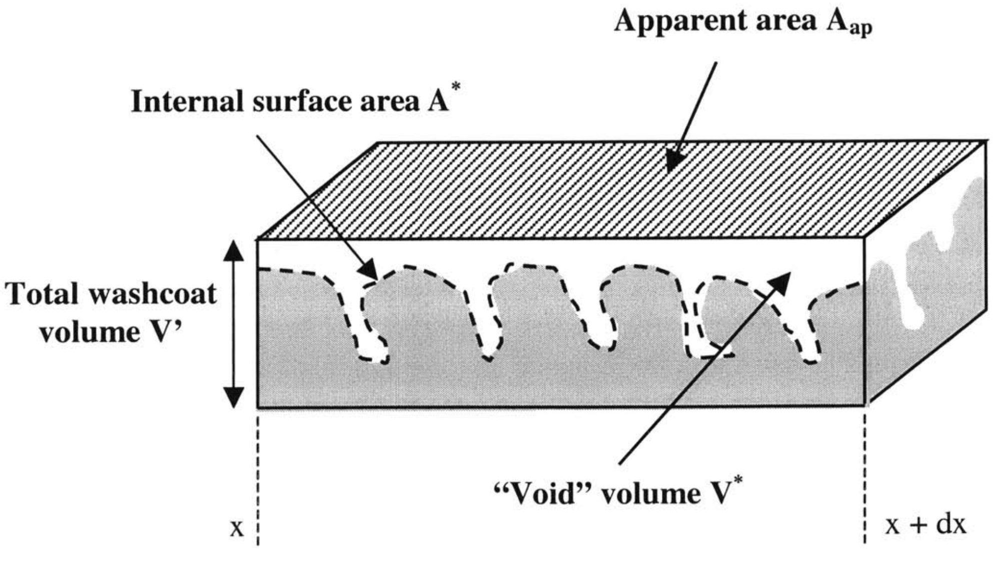

Fig. 4.11: *Definition of the volumes and areas involved in the mass transport equations*

Dividing by A_{ap}, Equation (4.4) becomes:

$$\frac{V^*}{A_{ap}}\cdot\frac{dc_{s,i}}{dt} = k_g\cdot\left(c_{g,i}-c_{s,i}\right)-\frac{A^*}{A_{ap}}\cdot\sum_{j=1}^{N_i} R_j\left(\overline{c_s},\overline{c^*},N_{s0},T_s\right) \tag{4.5}$$

Moreover, $\frac{V^*}{A_{ap}}=\frac{V^*}{V'}\cdot\frac{V'}{A_{ap}}=\frac{V^*}{V'}\cdot\frac{1-\varepsilon}{S}$, where $\frac{V^*}{V'}$ corresponds to the porosity of the washcoat referred to by ε_w. The monolith pore volume can be experimentally measured. Thus ε_w is a known quantity. It depends on the considered monolith but is usually of the order of 0.7 for automotive monolithic converters.

On the other hand, $\frac{A^*}{A_{ap}}=\frac{A^*}{V}\cdot\frac{V}{A_{ap}}=\frac{A^*}{V}\cdot\frac{1}{S}$. $\frac{A^*}{V}$ is the internal surface area per monolith volume and can be measured by physisorption experiments. Usually, this quantity, which will be referred to as a_m, is about 20000 m^2/L monolith volume [11].

Therefore, Equation (4.5) can be written as follows:

$$\boxed{\varepsilon_w\cdot(1-\varepsilon)\cdot\frac{dc_{s,i}}{dt} = k_g\cdot S\cdot\left(c_{g,i}-c_{s,i}\right)-a_m\cdot\sum_{j=1}^{N_i} R_j\left(\overline{c_s},\overline{c^*},N_{s0},T_s\right)} \tag{4.6}$$

with the kinetic rates expressed in $mol/m^2.s$.

ε_w and a_m depends on the axial position along the monolith axis. However, this dependence is hard to determine experimentally. Therefore, we consider them as uniform quantities along the monolith.

c) Transport equation for the adsorbates

The adsorbates only experience the changes of mass due to catalytic reactions. Hence, the transport equation for adsorbate i is:

$$A^*\cdot\frac{dc_i^*}{dt} = -A^*\cdot\sum_{j=1}^{N_i^*} R_j\left(\overline{c_s},\overline{c^*},N_{s0},T_s\right) \tag{4.7}$$

where N_i^* is the total number of elementary reactions involving adsorbate species i.

Dividing the equation by A^*, we obtain:

$$\boxed{\frac{dc_i^*}{dt} = -\sum_{j=1}^{N_i^*} R_j\left(\overline{c_s},\overline{c^*},N_{s0},T_s\right)} \tag{4.8}$$

To simulate the catalyst performance, equations (4.3), (4.6), and (4.8) need to be written for each individual species.

iii- External heat transfer

Figure 4.12 below summarizes the energy fluxes included in the model.

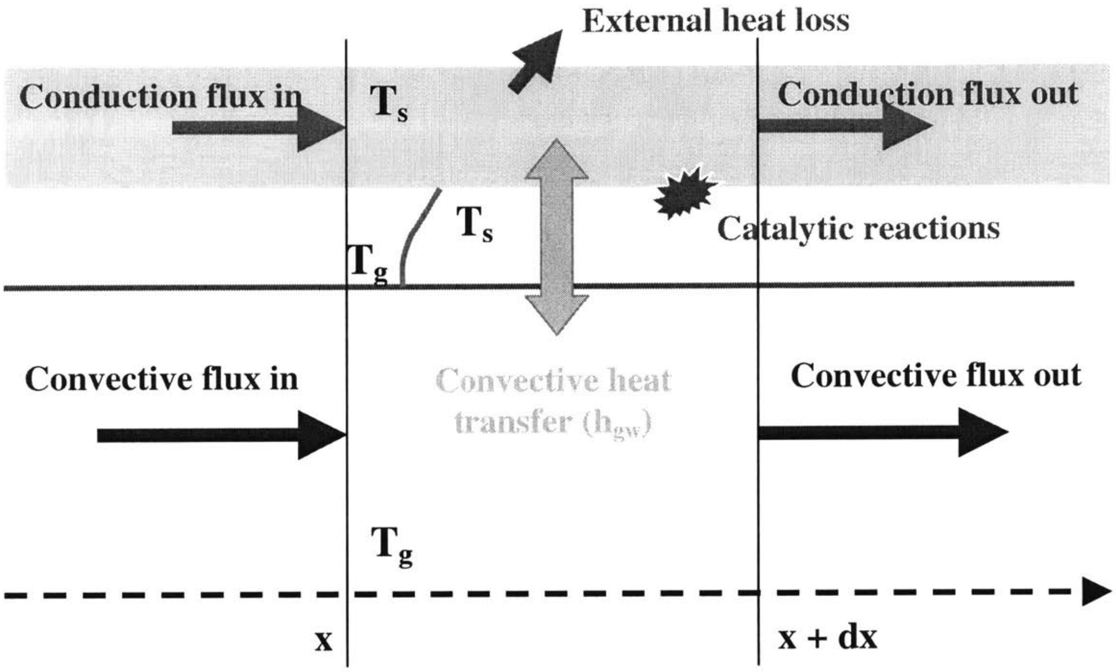

Fig. 4.12: *Energy transport fluxes on a slice of monolith*

The main fluxes accounted for are:

- The axial convective energy transfer in the bulk gas flow
- The heat transfer exchange between the bulk flow and the washcoat surface through the boundary layer
- The heat release and consumption from exothermic and endothermic reactions, respectively
- The axial conduction of heat in the solid phase
- The heat losses to the ambient

The modeling of the energy transfer through the boundary layer is done the same way as for the mass transfer. Indeed, as explained before, the boundary layer temperature profile can be lumped into a heat transfer coefficient h_{gw}, instead of looking at the detail of the boundary layer. Like the mass transfer coefficient k_g, this heat transfer coefficient will be further discussed in section 4.3.2 iv-.

The convection between the solid phase and the ambient is also modeled by a convective heat transfer coefficient h_{amb}.

Therefore, two quantities need to be balanced: the gaseous enthalpy and the solid enthalpy.

a) Transport equation for the gas phase

Since the enthalpy diffusion and conduction are neglected, the conservation of the gas phase enthalpy can be written:

$$\varepsilon \cdot \rho_g \cdot V \cdot \frac{dh_g}{dt} = -\dot{m} \cdot \Delta x \cdot \frac{dh_g}{dx} - h_{gw} \cdot A_{ap} \cdot \left(T_g - T_s\right) \tag{4.9}$$

where h_g is the massic enthalpy of the bulk gas mixture in J/kg

T_g is the gas phase temperature in K

T_s is the solid temperature in K

ρ_g is the density of the gas mixture in kg/m^3

$\dot{m}$ is the mass flow rate: $\dot{m} = \rho_g \cdot v \cdot A$, in kg/s

h_{gw} is the convective heat transfer coefficient in J/m^2.K.s.

In the above equation, ρ_g has been assumed constant along the monolith channel.

Considering the mixture as an ideal gas with constant heat capacity with respect to time and space, Equation (4.9) becomes:

$$\boxed{\varepsilon \cdot \rho_g \cdot Cp_g \cdot \frac{dT_g}{dt} = -\rho_g \cdot v \cdot Cp_g \cdot \frac{dT_g}{dx} - h_{gw} \cdot S \cdot \left(T_g - T_s\right)} \tag{4.10}$$

where Cp_g is the heat capacity of the gas mixture in J/kg.K.

b) Transport equation for the solid phase

The heat release of the surface reaction is assumed to be deposited only on the solid surface. With this assumption, the solid enthalpy balance leads to:

$$V' \rho_s \cdot \frac{dh_s}{dt} = \lambda_s \cdot V' \cdot \frac{d^2 T_s}{dx^2} + h_{gw} \cdot A_{ap} \cdot (T_g - T_s) - h_{amb} \cdot A_{ext} \cdot (T_s - T_{amb}) + \dot{Q}_{reaction} \tag{4.11}$$

where h_s is the massic enthalpy of the solid phase in J/kg

ρ_s is the solid density in kg/m^3

λ_s is the solid thermal conductivity in W/m.K

h_{amb} is the convective heat transfer coefficient at the solid/ambient air interface in J/m^2.K.s

T_{amb} is the temperature of the ambient air surrounding the monolith in K

A_{ext} is the effective area of convective exchange with the ambient; according to our assumption of equal distribution among the channels, $A_{ext} = \frac{S_{ext}}{n}$, where S_{ext} is the external peripheral area of the monolith and n its number of cells

$\dot{Q}_{reaction}$ is the heat flux due to the catalytic reactions:

$$\dot{Q}_{reaction} = A^{*}.\sum_{j=1}^{R} R_j\left(\overline{c_s}, \overline{c^*}, N_{s0}, T_s\right)\cdot(-\Delta H_j),$$

where R is the total number of considered elementary reactions and ΔH_j is the heat of elementary reaction j in J/mol. By convention, ΔH_j is negative for exothermic reactions and positive for endothermic ones.

Dividing Equation (4.11) by V, we obtain:

$$(1-\varepsilon)\cdot\rho_s\cdot\frac{dh_s}{dt} = \lambda_s\cdot(1-\varepsilon)\cdot\frac{d^2T_s}{dx^2} + h_{gw}S\cdot(T_g - T_s) - h_{amb}S_{amb}\cdot(T_s - T_{amb}) + \dot{q}_{reaction} \quad (4.12)$$

where $S_{amb} = \frac{A_{ext}}{V}$ and $\dot{q}_{reaction} = a_m.\sum_{j=1}^{R} R_j\left(\overline{c_s}, \overline{c^*}, N_{s0}, T_s\right)\cdot(-\Delta H_j)$ (in J/m^3.s).

Assuming that the solid heat capacity is constant with respect to time and space, the equation becomes:

$$\boxed{(1-\varepsilon)\cdot\rho_s\cdot Cp_s\cdot\frac{dT_s}{dt} = \lambda_s\cdot(1-\varepsilon)\cdot\frac{d^2T_s}{dx^2} + h_{gw}S\cdot(T_g - T_s) - h_{amb}S_{amb}\cdot(T_s - T_{amb}) + \dot{q}_{reaction}} \quad (4.13)$$

where Cp_s is the solid heat capacity in J/kg.K.

The variables of the transport equations c_{gi}, c_{si}, c_i^*, T_g, and T_s are all functions of two variables: the time t and the position along the channel x.

iv- Mass and heat transfer coefficients

The heat transfer coefficient h_{gw} and the mass transfer coefficient k_g were computed from the non-dimensional Nusselt and Sherwood numbers, respectively: $Nu = \frac{h_{gw}.d_h}{\lambda_g}$ and $Sh = \frac{k_g.d_h}{D_i}$. In these formulas, λ_g is the thermal conductivity of the considered gas mixture, D_i is the dispersion coefficient, and d_h is the hydraulic diameter of the considered pipe.

The Nusselt and Sherwood numbers were estimated from correlations for a laminar flow.

Indeed, at the monolith inlet, the flow is highly turbulent; thus, it enters the channel with Reynolds numbers in the region 5000-60,000 in the immediate front of the monolith [9, 24]. The flow stays turbulent in the channel entrance before a turbulent-to-laminar transition occurs. In the rest of the channel, the flow is laminar with Reynolds numbers between 20 and 300. The entrance length in which the flow stays turbulent only represents a small fraction of the monolith length [9] and was therefore neglected. The flow was thus considered as entirely laminar in the monolith channels.

The entrance length in which the flow develops may be estimated by $\left(\frac{d_h}{2}\right)^2.\frac{v}{D}$, where D is either the thermal or mass diffusivity. For a monolith with d_h=1.5 mm and $D \sim 0.6.10^{-4}$ m^2/s, this length at partial load, medium speed condition (v=5 m/s) is about 5 cm. The value will be larger at higher flow rates. Therefore, the transfer coefficients for a developing flow should be used. To simplify the matter however, the values for a fully developed flow are used here.

The Nusselt and Sherwood numbers were then approximated by their asymptotic values in rectangular channels for constant heat flux in the monolith channels [41]: $N_{u,\infty}$=3.608 and $S_{h,\infty}$=2.976.

This assumption has been proven to correctly predict quasi-steady state performance of the converter [39]. It is less adapted for the prediction of highly transient flows, but at least enables to capture the trends [3]. This assumption probably leads to an underestimation of the performance.

A more accurate model on this point would require a close look at the structure of the flow in the channels.

4.4 Catalytic reactions

As evoked previously with the examples of the CO oxidation, the catalytic reactions are modeled as a set of elementary reactions representing the detail of the adsorptions, desorptions, and surface reactions.

The reactions are considered to happen on the surface of the noble metals. The rest of the washcoat surface is modeled as a tank that stores species through the oxygen storage process. The oxygen storage modeling is detailed in section 4.5; this section focuses on the reactions on the precious metals.

4.4.1 Included species and chemical mechanisms

The chemistry model accounts for the 8 following gaseous species: O_2, CO, C_3H_6, H_2, NO, H_2O, CO_2, and N_2. The oxidation of propene (C_3H_6) represents the totality of the hydrocarbon reactions.

In the model, these species react through 7 overall mechanisms which are divided into three groups:

- *The oxidations reaction*
  - Oxidation of CO: $CO + 0.5 \cdot O_2 \leftrightarrow CO_2$
  - Oxidation of HC: $C_3H_6 + 4.5 \cdot O_2 \leftrightarrow 3 \cdot CO_2 + 3 \cdot H_2O$
  - Oxidation of H_2: $H_2 + 0.5 \cdot O_2 \leftrightarrow H_2O$
- *The NO reduction reactions*
  - Reduction of NO by CO: $CO + NO \leftrightarrow CO_2 + 0.5 \cdot N_2$
  - Reduction of NO by H_2: $NO + H_2 \leftrightarrow H_2O + 0.5 \cdot N_2$
- *The water reactions*
  - The water-gas shift reaction: $CO + H_2O \leftrightarrow CO_2 + H_2$
  - The steam-reforming reaction: $C_3H_6 + 6 \cdot H_2O \leftrightarrow 3 \cdot CO_2 + 6 \cdot H_2$

In reality, NO is also reduced by the hydrocarbons. However, the hydrocarbons diffuse more slowly to the surface than H_2 and CO. Thus, the fraction of NO reduced by HC is negligible compared to its reduced fraction by CO and H_2.

The formations of N_2O and NH_3 due to the reduction of NO were not accounted for. Indeed, N_2O is produced only at low temperatures and dissociated at higher temperatures in N_2. Moreover, even at low temperatures, the CO-NO reaction produces negligible amounts of N_2O in the presence of ceria (about 9 wt %), as explained in Chapter 3 [30]. Given the high percentages of ceria in typical automotive washcoats (about 20 wt %), N_2O production can thus be neglected. No information was found on the production of N_2O from the NO-H_2 reaction in the presence of ceria, but the trends were assumed to be similar to those of the CO-NO reaction.

NH_3 production is non-negligible on platinum and palladium. However, rhodium shows a high selectivity for N_2 formation, especially near stoichiometry [44]. Now, as explained in Chapter 3, the NO reactions tend to happen on rhodium, or at least to involve rhodium in alloyed particles because of the selectivity of the adsorption process. Moreover, catalytic converters are operated near stoichiometry. Thus, we did not include NH_3 production in the model. NH_3 production is especially low at high temperatures (above 500 C) [44]; so neglecting its production should mostly affect the warm-up predictions.

The water-gas shift and the steam reforming reactions were included because of their important role in the transient behavior of the catalyst [6].

4.4.2 Determination of the elementary steps in each mechanism

As said earlier, microkinetics modeling looks at the detail of the elementary reactions occurring on the surface. All reactions are considered simultaneously and are not grouped under the form of mechanisms in the simulation. Nevertheless, we looked at the reactions mechanism by mechanism because we need the mechanisms to determine the kinetic constants as explained in section 4.4.4. Given that most elementary reactions here considered appear in several mechanisms, we determined a minimal set of mechanisms by including only the main reactions necessary for formation of the products. Even if this minimal set does not represent all the physics of the real reaction, it contains the major ones.

i- CO oxidation

The oxidation of CO is a well-known mechanism. As already said, it includes three steps:

- The adsorption and desorption of O_2
- The adsorption and desorption of CO
- The formation of CO_2

As discussed in Chapter 3, CO adsorbs molecularly on the precious metals, but can adsorb on a single or several metal atoms depending on the form of the catalytic sites present on the surface. However, automotive catalysts present small catalytic particles that tend to adsorb CO on a single atom. Indeed, chemisorption experiments using CO have shown CO/Pt ratios of about 1 [16, 45]. A ratio of 1:1 is also expected on Pd. Unlike the other two noble metals, large Rh particles adsorb CO in a ratio 1/2 and small Rh particles in a ratio 2/1. Nevertheless, as explained in Chapter 3, in trimetallic catalysts, CO tends to adsorb on Pt and Pd, which adsorb it more strongly than Rh. Therefore, we chose a ratio CO/noble metal of 1:1.

O_2 adsorbs dissociatively on the noble metals. In fact, according to [46], O_2 can be found under two forms on the platinum surface: a molecularly adsorbed state and an atomically chemisorbed state. However, the molecularly adsorbed state desorbs at about 170 K, and is thus not encountered under automotive converters' operating conditions. On the contrary, the atomically chemisorbed state desorb from 600 to 1100 K, which perfectly corresponds to converters environments.

As discussed in Chapter 3, dissociative chemisorption occurs in two close steps: a molecular adsorption and then the dissociation on the surface. This type of adsorption can thus be represented in two different ways: by the two consecutive steps or by a single dissociative step, depending on the kinetic data that can be found. We chose to represent O_2 adsorption by a single dissociative step.

The third step in the CO-O_2 mechanism is the recombinative desorption of CO_2, CO_2 not being stable as an adsorbate.

To summarize, the CO oxidation mechanism is:

$$\begin{cases} O_2 + 2\cdot S \leftrightarrow 2\cdot O* \\ CO + S \leftrightarrow CO* \\ CO* + O* \leftrightarrow CO_2 \end{cases}$$

ii- H_2 oxidation

As explained in Chapter 3, H_2 adsorbs dissociatively on the metallic surface and only atomic H are active enough to participate in reactions [45]. Therefore, the adsorption of H_2 was represented as a single dissociative step: $H_2 + 2\cdot S \leftrightarrow 2\cdot H*$. On the contrary, H_2O adsorbs and desorbs molecularly.

According to *Sriramulu et al* [10] and *Anton and Cadogan* [47], the formation of H_2O occurs through the intermediate formation of adsorbate OH* as expressed in the following mechanism:

$$\begin{cases} H_2 + 2\cdot S \leftrightarrow 2\cdot H* \\ O_2 + 2\cdot S \leftrightarrow 2\cdot O* \\ O* + H* \leftrightarrow OH* + S \\ 2\cdot OH* \leftrightarrow H_2O* + O* \\ H* + OH* \leftrightarrow H_2O* + S \\ H_2O* \leftrightarrow H_2O + S \end{cases}$$

In particular, the direct desorption of OH* can be neglected at temperatures usually encountered during catalytic converters' operation. In fact, OH* desorption becomes important at higher temperatures (above 1000K) [48]. Direct adsorption of the hydroxyl radical $OH^\bullet$ is also neglected, this radical not being stable at the operating temperatures.

iii- HC oxidation

Very few articles detail the mechanisms of HC oxidation. *Schwartz et al* [49] studied the oxidation of several types of hydrocarbons (alkanes, olefins, alcohols...) on Pt and Pd and showed that the process of HC oxidation is initiated by the dissociative chemisorption of the hydrocarbon during which the weakest C-H bond is broken. This phenomenon was especially observed for alkanes. *Sriramulu et al* [10] confirm this observation by their assumed mechanism for C_3H_6 oxidation: during the catalytic oxidation process, the hydrocarbon is broken bond by bond.

Regarding C_3H_6 adsorption, *Sriramulu et al*'s mechanism is used here. The process consists of C_3H_6 molecular adsorption followed by successive partial dissociation of the hydrocarbon.

Again according to *Sriramulu et al*, the smaller hydrocarbon adsorbate is then oxidized step by step by the atomic oxygen from O_2 adsorption, which finally leads to the formation of CO_2.

Since H_2O is one of the products of HC oxidation, all the reactions involved in the H_2 oxidation mechanism also participate in the HC oxidation mechanism. H_2O is thus formed from the H* liberated during HC successive partial dehydrogenations.

To summarize, the global mechanism for HC oxidation is:

$$\begin{cases} O_2 + 2\cdot S \leftrightarrow 2\cdot O^* \\ C_3H_6 + S \leftrightarrow C_3H_6{}^* \\ C_3H_6{}^* + S \leftrightarrow C_3H_5{}^* + H^* \\ C_3H_5{}^* + S \leftrightarrow C_2H_4{}^* + CH^* \\ C_2H_4{}^* + S \leftrightarrow 2\cdot CH_2{}^* \\ CH_2{}^* + S \leftrightarrow CH^* + H^* \\ CH^* + O^* \leftrightarrow COH^* + S \\ COH^* + O^* \leftrightarrow COOH^* + S \\ COOH^* \leftrightarrow CO_2 + H^* \\ O^* + H^* \leftrightarrow OH^* + S \\ 2\cdot OH^* \leftrightarrow H_2O^* + O^* \\ H^* + OH^* \leftrightarrow H_2O^* + S \\ H_2O^* \leftrightarrow H_2O + S \end{cases}$$

iv- NO reduction reactions

On the Pt surface, NO primarily adsorbs molecularly and on terminally bound sites -- the N atom of the NO molecule attaches itself to a single noble metal atom --, especially as the surface coverage increases [50]. On Rh, NO dissociates very rapidly once adsorbed; thus, its adsorption is often considered as a dissociative one. However, even on Rh, the mechanism for the formation of N_2 involves NO molecules on the surface, especially at low temperatures [17] (see below). Moreover, Rh is not the only noble metal present in three-way catalysts. Therefore, the adsorption of NO was considered to be molecular, and its dissociation was included apart in the mechanisms for NO reduction.

As shown by *Hirano et al* [51], N_2 is formed through two pathways in the reduction of NO by H_2, depending on the temperature range. The common step is the adsorption of NO on the catalyst site to NO*, followed by dissociation to N*+O*. Then:

- below 600 K, the main contribution to N_2 formation comes from the reaction $NO^* + N^* \leftrightarrow N_2 + O^*$
- above 600 K, the main contribution comes from the direct recombination of two adsorbed nitrogen atoms: $N^* + N^* \leftrightarrow N_2$

The role of H_2 is to remove the O* so that the mechanism assists the N_2 conversion. To simulate the performance of the catalytic converter over a wide range of temperatures, both pathways must be included in the mechanism.

We assumed that the production of N_2 followed the same behavior in the NO-CO reactions.

According to the above discussions, the NO reduction mechanisms accounted for in the model are:

NO-CO mechanism

$$\begin{cases} CO + S \leftrightarrow CO^* \\ NO + S \leftrightarrow NO^* \\ NO^* + S \leftrightarrow N^* + O^* \\ NO^* + N^* \leftrightarrow N_2 + O^* + S \\ 2\cdot N^* \leftrightarrow N_2 + 2\cdot S \\ CO^* + O^* \leftrightarrow CO_2 \end{cases}$$

NO-H_2 mechanism

$$\begin{cases} H_2 + 2\cdot S \leftrightarrow 2\cdot H^* \\ NO + S \leftrightarrow NO^* \\ NO^* + S \leftrightarrow N^* + O^* \\ NO^* + N^* \leftrightarrow N_2 + O^* + S \\ 2\cdot N^* \leftrightarrow N_2 + 2\cdot S \\ H^* + O^* \leftrightarrow OH^* + S \\ 2\cdot OH^* \leftrightarrow H_2O^* + O^* \\ H^* + OH^* \leftrightarrow H_2O^* + S \\ H_2O^* \leftrightarrow H_2O + S \end{cases}$$

v- Water-gas shift reaction

As discussed in Chapter 3 (section 3.2.2 ii-), the water-gas shift reaction has been experimentally observed to occur through a bifunctional mechanism ([21], [52]). For instance, the mechanism involves the formation of formic acid groups COOH on the support surface from CO and OH adsorbed on the catalytic particles, as well as the direct adsorption of water by the support.

However, as previously said, we want to develop a simplified model in which the only interaction between the support and the catalytic particles lies in the oxygen storage process. We also neglected all direct reactions of the gaseous species with the support except from this oxygen storage process. Therefore, we chose to model the water-gas shift reaction by a monofunctional mechanism including the formation of the intermediate species observed in [21] and [52].

The resulting mechanism is:

$$\begin{cases} \mathrm{CO + S \leftrightarrow CO^*} \\ \mathrm{H_2O + S \leftrightarrow H_2O^*} \\ \mathrm{H_2O^* {+} S \leftrightarrow H^* {+} OH^*} \\ \mathrm{OH^* {+} CO^* \leftrightarrow COOH^* {+} S} \\ \mathrm{COOH^* \leftrightarrow CO_2 + H^*} \\ \mathrm{2 \cdot H^* \leftrightarrow H_2 + 2 \cdot S} \end{cases}$$

The H_2-O_2 reactions could also be added to the mechanism, but as explained at the beginning of the section, we chose not to include them to obtain a minimal representative mechanism.

vi- Steam reforming reaction

Several mechanisms have been proposed for the steam reforming reaction. [53], [54], and [55] propose bifunctional mechanisms in which H_2O is first adsorbed and activated on the support, on which it either forms OH groups ([54], [55]) or H_2 [53]. *Duprez et al* [55] admit the possibility of a monofunctional mechanism and propose a mechanism in which H_2O is activated on the metal to produce OH* and H_2. To stay consistent in our modeling of the chemical processes, we need to assume such a monofunctional mechanism. However, the reaction *Duprez et al* propose is highly endothermic and thus seems very unlikely. Therefore, we assumed that H_2O^* dissociated to produce OH* through reaction -17 and that H_2 was formed by recombination of two adsorbed H*.

Apart from the particularity of the H_2O reactions leading to H_2, all proposed mechanisms agree on the hydrocarbon part. Thus, the hydrocarbon is first dissociated bond by bond as explained earlier; the smallest hydrocarbon then reacts with OH* according to the following reaction: $CH^* + OH^* + S \leftrightarrow CO^* + 2 \cdot H^*$ (OH* being adsorbed on the support in bifunctional mechanisms).

The production of CO_2 and H_2 was then through the water-gas shift mechanism. Once again, not all reactions involving H*, OH*, and H_2O^* were included in the mechanism.

The following mechanism results:

$$\begin{cases} H_2O + S \leftrightarrow H_2O^* \\ C_3H_6 + S \leftrightarrow C_3H_6^* \\ C_3H_6^* + S \leftrightarrow C_3H_5^* + H^* \\ C_3H_5^* + S \leftrightarrow C_2H_4^* + CH^* \\ C_2H_4^* + S \leftrightarrow 2 \cdot CH_2^* \\ CH_2^* + S \leftrightarrow CH^* + H^* \\ H_2O^* \leftrightarrow OH^* + H^* \\ CH^* + OH^* + S \leftrightarrow CO^* + 2 \cdot H^* \\ CO^* + OH^* \leftrightarrow COOH^* + S \\ COOH^* \leftrightarrow CO_2 + H^* \\ 2 \cdot H^* \leftrightarrow H_2 + 2 \cdot S \end{cases}$$

The above mechanism shows that only the formation of CO_2 and H_2 was considered. Another type of steam reforming reaction that produces CO and not CO_2 also exists. We did not include the formation of CO because CO desorption from the surface is small, as proven by its kinetic constant in the next section.

To summarize, the global chemical reactions occurring on the catalytic surface were modeled by a set of 22 elementary reactions (see Table 4.3) involving 8 gaseous species and 14 adsorbed intermediates. In the rest of the study, these elementary reactions will be referred to by their numbers in Table 4.3.

Table 4.3: *List of the elementary reactions included in the model*

(1) $O_2 + 2 \cdot S \leftrightarrow 2 \cdot O*$

(2) $CO + S \leftrightarrow CO*$

(3) $C_3H_6 + S \leftrightarrow C_3H_6*$

(4) $H_2 + 2 \cdot S \leftrightarrow 2 \cdot H*$

(5) $NO + S \leftrightarrow NO*$

(6) $H_2O + S \leftrightarrow H_2O*$

(7) $CO* + O* \leftrightarrow CO_2 + 2 \cdot S$

(8) $C_3H_6* + S \leftrightarrow C_3H_5* + H*$

(9) $C_3H_5* + S \leftrightarrow C_2H_4* + CH*$

(10) $C_2H_4* + S \leftrightarrow 2 \cdot CH_2*$

(11) $CH_2* + S \leftrightarrow CH* + H*$

(12) $CH* + O* \leftrightarrow COH* + S$

(13) $COH* + O* \leftrightarrow COOH* + S$

(14) $COOH* \leftrightarrow CO_2 + H*$

(15) $H* + O* \leftrightarrow OH* + S$

(16) $2 \cdot OH* \leftrightarrow O* + H_2O*$

(17) $H* + OH* \leftrightarrow H_2O* + S$

(18) $NO* + S \leftrightarrow N* + O*$

(19) $NO* + N* \leftrightarrow N_2 + O* + S$

(20) $2 \cdot N* \leftrightarrow N_2 + 2 \cdot S$

(21) $OH* + CO* \leftrightarrow COOH* + S$

(22) $CH* + OH* + S \leftrightarrow CO* + 2 \cdot H*$

4.4.3 Rate expressions

The rates of the above reactions can be written as a function of their kinetic constant, reactant concentrations, and the reactants stoichiometric coefficients only. Indeed, the rate expression for an elementary reaction $\alpha \cdot A + \beta \cdot B \rightarrow \gamma \cdot C + \delta \cdot D$ is $R = k \cdot [A]^{\alpha} \cdot [B]^{\beta}$, where k is the kinetic constant for the reaction, [A] and [B] the reactants concentrations, and α and β the reactants stoichiometric coefficients. We shall use the convention that all gaseous concentrations are in mole/m^3 and all surface species concentrations are in mole/m^2.

All the elementary reactions listed in Table 4.3 are considered in both forward and reverse directions. They are thus characterized by two elementary rates. We use the subscript f for forward rates and kinetic constants and the subscript r for reverse rates and kinetic constants. Moreover, in microkinetics modeling, no simplification is made that any step is rate limiting or equilibrated.

By convention, partial coverages rather than concentrations are used for adsorbed species. The coverage of a species i is defined as the ratio of the concentration of adsorbed species i over the total surface concentration of catalytic sites on the surface: $\theta_i^* = \frac{[i]}{[S]_0}$. Thus, for instance, the rate expression for CO desorption is written: $R_{r2} = k_{r2} \cdot [S]_0 \cdot \theta_{CO}^*$. This convention also applies for the concentration of available sites on the surface: $[S] = [S]_0 \cdot \left(1 - \sum_{i=1}^{N^*} \theta_i^*\right)$, where N* is the total number of adsorbate species present on the surface. In the model, the total surface concentration of sites [S]$_0$ (mol/m^2) is assumed to be uniform along the monolith and only monocoverage of the surface is allowed. Also, the model does not distinguish between the different types of catalytic sites (whether it is Pt, Pd, or Rh).

4.4.4 Kinetic constants determination

i- Assumptions

The main part of the chemical modeling consisted in the determination of the kinetic constants for each forward and reverse elementary reactions. This determination was made with the following assumptions.

a) Form of the kinetic constants

The kinetic constants were searched under the form:

$$k = A \cdot \left(\frac{T}{300}\right)^{\beta} \cdot \exp\left(-\frac{E_A}{R_g \cdot T}\right),$$

where A is the pre-exponential factor, β characterizes the temperature dependence, E_A is the activation energy of the reaction in J/mol, T is the temperature at which the reaction occurs (surface temperature T_s in our case), and R_g is the universal gas constant (R_g=8.314 J/mol.K). Therefore, three parameters needed to be determined for each forward and each reverse reactions: A, β, and E_A.

In fact, the pre-exponential factor and activation energy depend on the global coverage of the catalytic surface. Indeed, as the global coverage increases, the mobility of the adsorbates on the surface is reduced. Moreover, the probability of two reactants to adsorb close to each other decreases. We neglected this dependence and considered A and E_A as constants. While gathering the needed kinetic information, we thus tried to assemble a set of data corresponding to low surface coverages. This may surestimate the performance of the catalyst.

Note that the set of reactions included here does not include those associated with the catalyst aging process.

b) Surface diffusion

We have seen in section 3.2.2 that two adsorbed reactants need to be close to each other to react, and that they move toward each other via surface diffusion. In the model, this surface diffusion process was lumped into the kinetic constants of the reactions. Indeed, values of surface diffusion at low surface coverages and ambient temperatures are typically in the range of 10^{-4} to 10^{-6} cm^2/s ([37], [38], [39]). The catalytic particles typically being 50 angstroms in diameter in fresh catalysts, the resulting diffusion time is less than $2.5.10^{-7}$ s at ambient temperature. Surface diffusion is thus fast compared to the chemical reactions (see section 4.2).

c) Noble metals considerations

The three noble metals show different catalytic activities towards the main chemical reactions. For example, Rh is particularly good at promoting NO reduction and the steam reforming reaction whereas Pt is better at promoting CO and HC oxidations, and the water-gas shift reaction; Pd is even better than Pt for the oxidations of CO and fast-oxidizing HC.

TWCC use a combination of two or three of the noble metals. As seen in Chapter 3, even in such combinations, the particular roles of the different catalysts tend to be respected, especially thanks to the selectivity of the adsorption process. For instance, when sufficient Rh is present, the participation of Pt in NO removal has been shown to be minimal. Nevertheless, interactions between the noble metals become important if the loadings are important.

Our model neglects the interactions between the noble metals and assumes that the catalytic activity is independently divided among the different noble metals. Moreover, kinetic data for reactions on Pd were difficult to find; thus, only Rh and Pt were considered. Hence, in the model, NO adsorption and dissociation occur on Rh while the rest of the reactions occur on Pt.

Furthermore, all noble metals were considered initially present under their reduced metallic form.

d) Structure sensitivity

The activity of a catalyst depends on the structure of its crystallite surface. This crystallite structure is usually identified by a number; for example, Pt(111), Pt(110), and Pt(100) are different crystal planes with different activities. All reactions are not structure sensitive; nevertheless the oxidation and reduction reactions have been shown to be.

Since we do not have enough knowledge about crystallites structures and did not want to further complicate the model, we neglected the structure sensitivity of the reactions.

ii- Determination of the pre-exponential factors, activation energies, and temperature dependence coefficients

a) General determination methods

The determination of the missing 132 kinetic parameters required the combined use of the following main methods:

- Literature review
- Thermodynamic consistency of the mechanism at 800K
- Estimations from transition state theory (TST)
- Collision theory formula for adsorption reactions

These four methods helped us to determine kinetic constants that characterize the catalytic activity on a flat metallic surface and not on the catalytic surface of a supported-catalyst. The determined kinetic constants are thus fundamental numbers. The required conversion will be detailed in section 4.4.4 ii- c).

The assembled and computed constants were then compared to global kinetic rate expressions to discuss their validity.

The next paragraphs give the main characteristics of each of these methods.

1) Literature review

Literature constitutes our first source of kinetic data. In particular, *Sriramulu et al* [10] report kinetic data for several forward reactions involved in the CO-O_2, C_3H_6-O_2, H_2-O_2 reactions on Pt, and NO reduction reactions on Rh. In fact, this article is the only one that gathers kinetic data on several mechanisms in the same place. The rest of our literature sources consist of specialized articles focusing on a single mechanism. Indeed, mechanisms such as the CO-O_2, H_2-O_2, and NO reduction reactions by CO and H_2 have been studied several times. We thus compared the obtained kinetic data and selected the ones that corresponded the most to our operating conditions and to the assumption of low coverages (see 4.4.4 i-). As previously announced, we indifferently looked at sources for different crystallite structures, trying to average these data to account for all structures when possible.

However, the literature review did not suffice to determine all the kinetic data. In particular, the reverse HC oxidation reactions and the detail of the water-gas shift and steam reforming reactions have not been widely studied. Methods 2 and 3 were used to fill in the blanks.

2) Thermodynamic consistency of the mechanism at 800 K

The detail of the elementary reactions must be thermodynamically consistent with the global reaction. Indeed, the enthalpy and entropy changes of a global reaction must be equal to the stoichiometry-weighted enthalpy and entropy changes computed from the detailed mechanism of the same reaction, as expressed by the following equations [56]:

$$\sum_{i=1}^{N} \sigma_i \cdot E_{Ai,f} - \sum_{i=1}^{N} \sigma_i \cdot E_{Ai,r} = \Delta H_{net} \tag{4.14}$$

$$\prod_{i=1}^{N} \left(\frac{A_{i,r}'}{A_{i,f}'} \right)^{\sigma_i} = \exp\left(\frac{\Delta G_{net} - \Delta H_{net}}{R_g \cdot T} \right) \tag{4.15}$$

where $E_{Ai,f}$ anf $E_{Ai,r}$ are the forward and reverse activation energies of elementary reaction i

$A_{i,f}' = A_{i,f} \cdot \left(\frac{T}{300} \right)^{\beta_f}$ and $A_{i,r}' = A_{i,r} \cdot \left(\frac{T}{300} \right)^{\beta_r}$

N is the number of elementary reactions in the considered mechanism

ΔH_{net} and ΔG_{net} are the enthalpy and free energy changes of the global reactions at temperature T in J/mol

σ_i is the stoichiometric number of elementary reaction i

To understand what the stoichiometric numbers are, let us consider the example of the CO oxidation reaction. The global reaction $CO + 0.5 \cdot O_2 \leftrightarrow CO_2$ is represented by the three following elementary steps: $\begin{cases} O_2 + 2 \cdot S \leftrightarrow 2 \cdot O^* (1) \\ CO + S \leftrightarrow CO^* (2) \\ CO^* + O^* \leftrightarrow CO_2 (7) \end{cases}$. In fact, the weighted addition

0.5*(1) + 1*(2) + 1*(7) gives the global reaction. The coefficients 0.5, 1, and 1 are the stoichiometric numbers of reactions (1), (2), and (7) respectively.

Thus, Equations (4.14) and (4.15) combine the definition of the stoichiometric numbers with the definition of the enthalpy and entropy changes of an elementary reaction i:

$$\Delta H_i = E_{i,f} - E_{i,r}$$

$$A_{i,r}' = A_{i,f}' \cdot \exp\left(\frac{\Delta G_i - \Delta H_i}{R_g \cdot T}\right)$$

In these equations, one has to be careful about the units to be used. Indeed, the pre-exponentials for surface reactions must be in s^{-1}. Moreover, the units must be consistent with the conditions chosen for calculation of the free energy for reactions involving gaseous species. For instance, if the free energy has been computed for a pressure of 1 bar, the pre-exponentials for adsorption reactions must be expressed in $bar^{-1}.s^{-1}$. The conversion of the rate constants will be further discussed in section 4.4.4 ii-c.

The model ensures the thermodynamic consistency of the mechanisms at 800K, which corresponds to the mean temperature that can be encountered during usual catalytic operation.

3) Estimations from transition state theory

The thermodynamic consistency formulas are particularly useful to determine the kinetic data of a single missing reaction. However, additional information is required when the kinetic information of several reactions is unknown.

The transition state theory furnishes estimations for the pre-exponentials of different kinds of reactions such as molecular and dissociative adsorptions, Langmuir-Hinshelwood and Eley-Rideal surface reactions, and molecular and recombinative desorptions. Figure 4.13 presents the computed estimations we used [56].

Reaction and Conditions	*Estimates*
Molecular Adsorption	
$A + * \rightarrow A^*$	$r = A\,[\exp -(E_a/k_BT)]P_A\theta^*$
Mobile transition state	$A = 10^3$/Pa s
Immobile transition state	$A = 10^1$/Pa s
Dissociative Adsorption	
$A_2 + 2^* \rightarrow 2A^*$	$r = A\,[\exp -(E_a/k_BT)]P_{A2}(\theta^*)^2$
Mobile transition state	$A = 10^3$/Pa s
Immobile transition state	$A = 10^1$/Pa s
Langmuir–Hinshelwood Reaction	
$A^* + B^* \rightarrow C^* + D^*$	$r = A\,[\exp -(E_a/k_BT)]\theta_{A^*}\theta_{B^*}$
Mobile surface species with rotation	$A = 10^8$/s
Mobile surface species without rotation	$A = 10^{11}$/s
Immobile surface species without rotation	$A = 10^{13}$/s
Eley–Rideal Reaction	
$A + B^* \rightarrow AB^*$	$r = A\,[\exp -(E_a/k_BT)]P_A\theta_{B^*}$
Mobile transition state	$A = 10^3$/Pa s
Immobile transition state	$A = 10^1$/Pa s
Molecular Desorption	
$A^* \rightarrow A + *$	$r = A\,[\exp -(E_a/k_BT)]\theta_{A^*}$
Similar freedom for adsorbed and transition states	$A = 10^{13}$/s
More rotational and translational freedom for transition state	$A = 10^{16}$/s
Associative Desorption	
$2A^* \rightarrow A_2 + 2^*$	$r = A\,[\exp -(E_a/k_BT)](\theta_{A^*})^2$
Mobile adsorbed and transition states with full rotational freedom	$A = 10^8$/s
Mobile adsorbed and transition states without rotation	$A = 10^{11}$/s
Immobile adsorbed and transition states	$A = 10^{13}$/s
Immobile species with more rotational and translational freedom for transition state	$A = 10^{16}$/s

Fig. 4.13: *Transition-state theory estimates of pre-exponential factors [56]*

4) Collision theory formula for adsorption reactions

Adsorption reactions can be treated differently from the other reactions. Indeed, the collision theory gives a formula to compute the adsorption kinetic constant from the sticking probability of the adsorbing gas molecule. In the literature, adsorption reactions are usually written in terms of partial pressures of the gas species. Then for example, for CO adsorption, with n_{CO} the molecular concentration in the gas phase:

$$\begin{aligned}\frac{d[CO^*]}{dt} &= k_f' \cdot n_{CO} \cdot [S] \\ &= \left(\frac{k_f'}{k_B \cdot T}\right) \cdot P_{CO} \cdot [S] \\ &= k_f \cdot P_{CO} \cdot [S]\end{aligned}$$

Here, [S] and [CO*] have dimensions of sites/m^2, and k_f has dimensions of Pa^{-1}.s^{-1} and is given by the following formula:

$$k_f = \frac{s_0(T) \cdot \sigma}{\sqrt{2 \cdot \pi \cdot M \cdot k_B \cdot T}} \tag{4.16}$$

where M is the weight of the adsorbing molecule in kg

k_B is Boltzmann constant: $k_B = 1.38.10^{-23}$ J/K

T is the surface temperature in K

s_o is the initial sticking coefficient (dimensionless) of the gaseous molecule, or, in other words, the probability that the gaseous molecule adsorbs on an empty surface

σ is the adsorption area per site in m^2.

Equation 4.16 was employed to compute the adsorption constants of O_2, CO, H_2, and H_2O whose sticking coefficients were found in the literature. We were able to account for the temperature dependence of the sticking coefficient only for O_2. The remaining adsorption constants (C_3H_6, NO) were directly found in the literature.

5) Comparisons of the detailed kinetics with global rate expressions

As explained in Chapter 1, all previously developed models, except for *Sriramulu et al* [10], use global rate expressions. Among those models, *Koltsakis et al* [9] give global rate expressions for the oxidation of CO, H_2, fast and slow oxidizing hydrocarbons, the reduction of NO by CO, and the steam reforming reaction. They also provide global rate expressions for the oxygen storage process. As will be explained in section 4.5, we used these oxygen storage rates to determine some of the kinetic constants for our oxygen storage submodel. Hence, to stay consistent in our comparisons, we chose to use the other rate expressions from *Koltsakis et al* as well.

We were not able to find a sufficient set of global rate expressions to compare all our mechanisms. However, all mechanisms agree with each other. Hence, the comparison of a few of them enabled us to discuss the validity of our kinetic data.

These comparisons are detailed in section 4.4.4 iii-.

The next sections detail how the discussed methods were applied to each mechanism.

b) Gathering of the kinetic constants

The assembled set of kinetic data is summarized in Table 4.12 at the end of the section.

1) Computed adsorption constants

As explained previously, O_2, CO, H_2, and H_2O adsorption constants were computed from the collision-theory formula.

- *O_2 adsorption*

The sticking coefficient for O_2 was taken from *Campbell et al* [46]. Indeed, they studied the evolution of the initial sticking coefficient for dissociative O_2 adsorption with surface temperature (see Figure 4.14(a)) and proposed the following expression to fit their experimental data: $s_o = 6.8.10^{-3} \cdot \exp\left(\frac{6270}{R_g \cdot T_s}\right)$, where T_s is the surface temperature.

To simplify the problem and keep the temperature dependence under the form $\left(\frac{T}{300}\right)^{\beta}$, we fitted the exponential decrease of the sticking coefficient by a power decrease as represented on Figure 4.14(b).

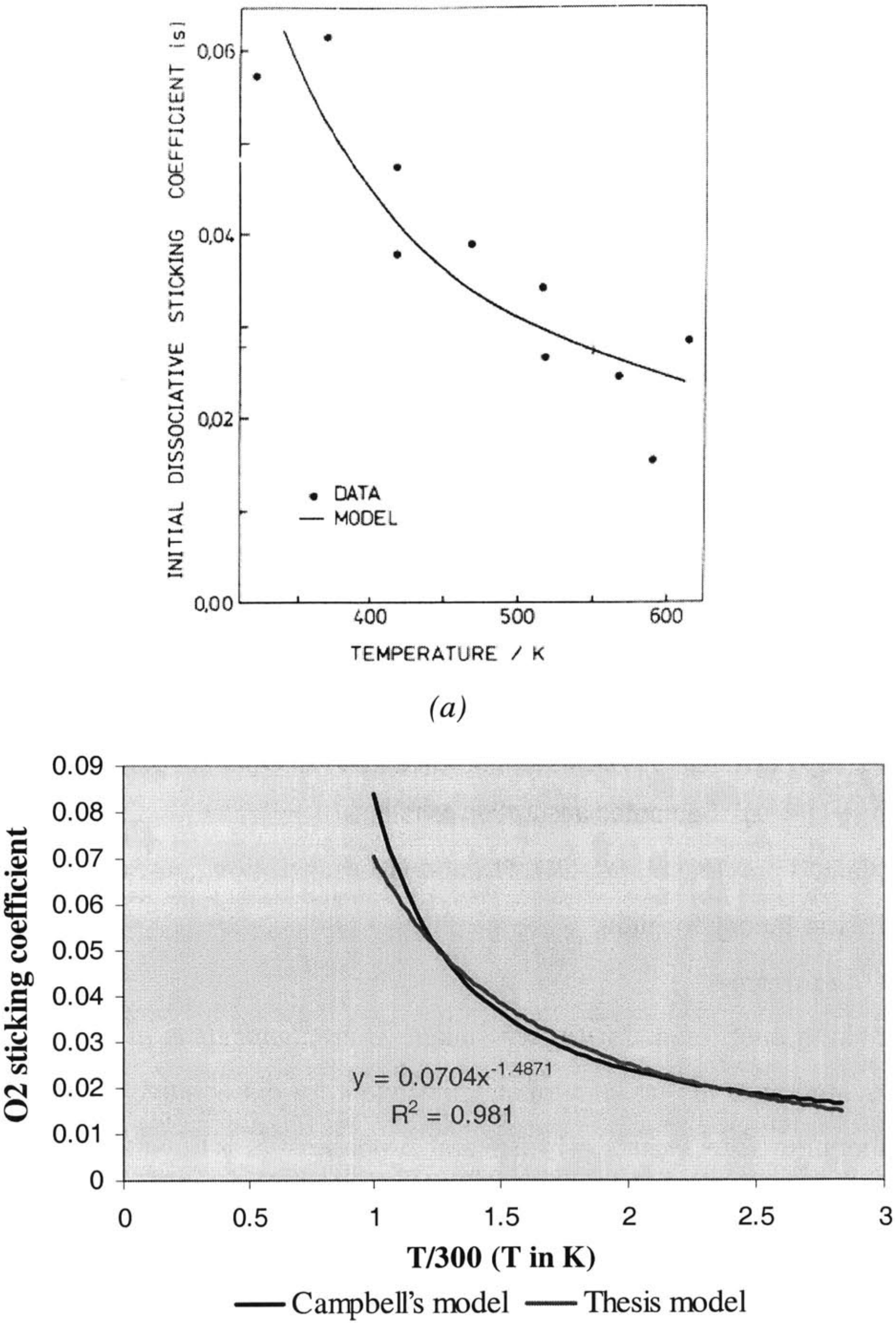

(a)

(b)

Fig. 4.14: *Variation of O_2 sticking coefficient with the surface temperature (a) Campbell's fitting model [46]; (b) Adaptation of Campbell's model to our model*

Thus, in our model: $s_o = 0.0704 \cdot \left(\frac{T_s}{300}\right)^{-1.487}$.

Since the activation energy for O_2 adsorption is $E_{Af1}=0$ on Pt ([10], [46]), the rate constant can thus be written: $k_{f1} = A_{f1} \cdot \left(\frac{T_s}{300}\right)^{\beta} = \frac{0.0704 \cdot \sigma}{\sqrt{2 \cdot \pi \cdot M \cdot k_B}} \cdot \left(\frac{T_s}{300}\right)^{-1.487} \cdot T_s^{-0.5}$.

Using this formula at 300 K gives: $\frac{k_{f1}}{\sigma} = 1.894 \cdot 10^{21} \cdot \left(\frac{T_s}{300}\right)^{-1.987}$ $m^{-2}.Pa^{-1}.s^{-1}$.

In typical catalytic converters, the noble metal collision cross-section per atom is about $\sigma=8.10^{-20}$ m^2 ([56], [57]).

Hence, $\boxed{k_{f1} = 1.51 \cdot 10^{2} \cdot \left(\frac{T_s}{300}\right)^{-1.987} \ s^{-1}.Pa^{-1}}$.

- *CO adsorption*

Like O_2 adsorption, CO adsorption is a non-activated process: $E_{Af2}=0$. Moreover, the initial sticking coefficient of CO has been found to be independent of T between 300 and 650 K [58]. Hence, we assumed $s_0=0.92$ over the entire range of operating temperatures, which corresponds to the adsorption of CO on Pt [58]. With this value, we found: $\boxed{k_{f2} = 2.12 \cdot 10^{3} \cdot \left(\frac{T_s}{300}\right)^{-0.5} \ s^{-1}.Pa^{-1}}$.

- *H_2 adsorption*

The kinetic constant for H_2 adsorption, k_{f4}, was computed from the initial sticking coefficient given in *Williams et al* [48]: $s_0=0.105$. Although *Williams et al* performed a study at high temperatures, the initial sticking coefficients they propose seem to agree with other articles that give results at lower temperatures. For instance, *Anton and Cadogan* [47] declare that the initial sticking coefficient for H_2 adsorption must be greater than 0.08 between 373K and 723K. Moreover, $E_{Af4}=0$ ([10], [48]).

Hence, the adsorption constant for H_2 adsorption is:

$$\boxed{k_{f4} = 9.04 \cdot 10^{2} \cdot \left(\frac{T_s}{300}\right)^{-0.5} \ s^{-1}.Pa^{-1}}$$

- *H_2O adsorption*

Williams et al [48] propose an initial sticking coefficient for H_2O adsorption of s_o=0.1 at high temperatures. However, sticking coefficients as large as 0.5 have been reported on Pt [59]. Thus, it seems that H_2O sticking coefficient varies quite rapidly with temperature. We chose to use an average sticking coefficient of 0.35, which seems to agree with the adsorption pre-exponential given in *Sriramulu et al* [10] of 10^3. With this value of the sticking coefficient, and since $E_{Af6}=0$ [10], the kinetic constant for H_2O adsorption is: $\boxed{k_{f6} = 10^3 \cdot \left(\frac{T_s}{300}\right)^{-0.5} \quad s^{-1}.Pa^{-1}}$

These computed adsorption constants are the only constants that show a temperature dependence in $\left(\frac{T}{300}\right)^{\beta}$, except for k_{f19}, which is discussed in 5). In other words, only β_{f1}, β_{f2}, β_{f4}, β_{f6}, and β_{f19} are different from 0.

2) Enthalpy and free energy changes of the global reactions

The changes in enthalpy and free energy of the global reactions need to be checked for thermodynamic consistency. These values were computed from JANAF thermodynamic tables [60] and [61] using the enthalpies and free energies of the individual gaseous species listed in Table 4.4.

Table 4.4: *Enthalpies and free energies (chemical plus sensible) of the gaseous species at 800 K*

Species	Enthalpy at 800 K (kJ/mol)	Free energy at 800 K (kJ/mol)
O_2	15.835	-172.901
CO	-95.35	-277.171
C_3H_6	70.315	-217.648
H_2	14.702	-112.936
NO	105.839	-87.031
H_2O	-223.824	-402.884
CO_2	-370.716	-576.711
N_2	15.046	-161.767

3) CO-O_2 mechanism

Table 4.5: *Mechanism for the CO-O_2 reaction*

Reaction	Stoichiometric number
(1) $O_2 + 2\cdot S \leftrightarrow 2\cdot O*$	0.5
(2) $CO + S \leftrightarrow CO*$	1
(7) $CO* + O* \leftrightarrow CO_2 + 2\cdot S$	1

The kinetic constants for O_2 desorption, CO desorption, and forward reaction 7 were obtained from the literature.

O_2 desorption pre-exponential was taken from [46], whereas its activation energy is an average for low coverage values based on [46] and [62].

CO desorption pre-exponential and activation energy were taken from [58]. In particular, the activation energy is an average between the reported activation energies for Pt(111), Pt(110), and Pt(100) ([58] p15).

The kinetic parameters for forward reaction 7 come from *Sriramulu et al* [10].

Thus, in the CO-O_2 mechanism, only the kinetics of reverse reaction 7 were unknown. A_{r7} and E_{Ar7} were determined from the thermodynamic consistency of the mechanism at 800 K.

4) H_2-O_2 mechanism

Table 4.6: *Mechanism for the H_2-O_2 reaction*

Reaction	Stoichiometric number
(4) $H_2 + 2\cdot S \leftrightarrow 2\cdot H*$	1
(1) $O_2 + 2\cdot S \leftrightarrow 2\cdot O*$	0.5
(15) $O* + H* \leftrightarrow OH* + S$	0.5
(-16) $H_2O* + O* \leftrightarrow 2\cdot OH*$	0.5
(17) $H* + OH* \leftrightarrow H_2O* + S$	1.5
(-6) $H_2O* \leftrightarrow H_2O + S$	1

The kinetic parameters for H_2 desorption come from *McCabe and Schmidt*, whereas H_2O desorption kinetics were taken from *Fisher and Gland* (see [48]).

The kinetic data for reactions 15 forward, 16 reverse, and 17 forward come from [10]. Forward reaction 16 was determined from [47] and [63]. To be more precise, E_{Af16} was computed as the average between the activation energies given by the two articles (75 kJ/mol and 51.4 kJ/mol respectively). In fact, the obtained value agrees with the heat of reaction ΔH_{16} from [47].

Reverse reactions 15 and 17 were missing. The thermodynamic consistency enabled us to find first equations linking A_{f15} to A_{f17} and E_{Af15} to E_{Af17}. Indeed, according to the stoichiometric numbers reported in Table 4.6, we have:

$$A_{r15}{}^{0.5} \cdot A_{r17}{}^{1.5} = 1.22 \cdot 10^{26} \tag{4.17}$$

$$0.5 \cdot E_{Ar15} + 1.5 \cdot E_{Ar17} = 183.944 \tag{4.18}$$

These two equations are not sufficient for us to determine the four missing parameters; two more equations are required. These required equations come from the consistency of the NO reduction reactions, as explained in the next section.

5) NO reduction reactions

As explained in section 4.4.2, two pathways lead to N_2 formation: the combination of NO* and N* (reaction 19) and the recombination of two N* (reaction 20). The stoichiometric numbers were thus more complicated to determine for the NO reduction mechanisms than for the previous reactions. Indeed, there is not a unique way of setting them. Thus, we considered that both reactions 19 and 20 equally participated in the production of N_2. Table 4.7 and 4.8 below give the resulting list of stoichiometric numbers for the NO-CO and NO-H_2 reactions, respectively.

Table 4.7: *Mechanism for the NO-CO reaction*

Reaction	Stoichiometric number
(5) $NO + S \leftrightarrow NO^*$	1
(2) $CO + S \leftrightarrow CO^*$	1
(18) $NO^* + S \leftrightarrow N^* + O^*$	0.75
(19) $NO^* + N^* \leftrightarrow N_2 + O^* + S$	0.25
(20) $N^* + N^* \leftrightarrow N_2 + 2 \cdot S$	0.25
(7) $CO^* + O^* \leftrightarrow CO_2 + 2 \cdot S$	1

Table 4.8: *Mechanism for the NO-H_2 reaction*

Reaction	Stoichiometric number
(5) $NO + S \leftrightarrow NO*$	1
(4) $H_2 + 2 \cdot S \leftrightarrow 2 \cdot H*$	1
(18) $NO* + S \leftrightarrow N* + O*$	0.75
(19) $NO* + N* \leftrightarrow N_2 + O* + S$	0.25
(20) $N* + N* \leftrightarrow N_2 + 2 \cdot S$	0.25
(15) $O* + H* \leftrightarrow OH* + S$	1.5
(17) $H* + OH* \leftrightarrow H_2O* + S$	0.5
(16) $2 \cdot OH* \leftrightarrow O* + H_2O*$	1
(-6) $H_2O* \leftrightarrow H_2O + S$	0.5

A_{f5} and E_{Af5} correspond to the adsorption of NO on Rh and were taken from [10].

Fink et al [64] studied NO desorption from Pt and report $A_{r5}=1.7.10^{15}$ s^{-1} and $E_{Ar5}=150$ kJ/mol at low coverages. *Hirano et al* [51] report $A_{r5}=10^{13}$ s^{-1} and $E_{Ar5}=105$ kJ/mol on $Pt_{0.25}$-$Rh_{0.75}$ for saturation coverages. Neither of these two articles gives data that correspond to our assumptions. Indeed, as explained previously, we want to represent NO adsorption on Rh at low coverages. Nevertheless, according to [64], the desorption energy decreases with increasing coverage whereas the pre-exponential stays constant. Hence, we chose $A_{r5}=10^{13}$ s^{-1} to be close to Rh activity and $E_{Ar5}=120$ kJ/mol to respect our low coverage assumption.

The kinetic data for forward reaction 18 corresponds to the dissociation of NO on Rh [10]. In absence of such data on Rh, the kinetic parameters for forward reaction 20 were taken from *Fink et al* [64], and thus represent the reaction on Pt.

As explained earlier, reaction 19 is the main pathway to N_2 formation under 600 K while reaction 20 is the main pathway above 600 K. We determined the kinetic parameters A_{f19}, E_{Af19}, and β_{f19} to traduce this experimentally observed behavior. In fact, these three parameters were set for k_{f19} to be about 5 times larger than k_{f20} at 400K, about the same at 600K, and 5 times less at 800K. In this computation, we tried to keep the orders of magnitude of the pre-exponential and activation energy of reaction 20. The resulting parameters are: $A_{f19}=10^{11}$ s^{-1}, $E_{Af19}=76$ kJ/mol, and $\beta_{f19}= -2.5$.

The kinetic constants of the three remaining reactions (reverse reactions 18, 19, and 20) were computed from the thermodynamic consistency of the NO-CO mechanism, estimations from the transition state theory and thermodynamics considerations.

The thermodynamic consistency of the NO-CO mechanism gives the following equations:

$$A_{r18}^{0.75} \cdot A_{r19}^{0.25} \cdot A_{r20}^{0.25} = 5.86 \cdot 10^{14} \tag{4.19}$$

$$0.75 \cdot E_{Ar18} + 0.25 \cdot E_{Ar19} + 0.25 \cdot E_{Ar20} = 178 \text{kJ/mol} \tag{4.20}$$

According to [65], N_2 heat of adsorption on Pt(111) is ΔH_{-20}= -15.24 kJ/mol. Hence, E_{Ar20}=69.16 kJ/mol.

Moreover, the heats of reactions 18, 19, and 20 are linked by the relation:

$$\Delta H_{19} = \Delta H_{18} + \Delta H_{20} \tag{4.21}$$

Indeed, the bonds broken and reformed in reaction 19 are the same as those broken and reformed in reactions 18 and 20.

Solving Equations (4.20) and (4.21) knowing E_{Ar20} gives E_{Ar18}=163 kJ/mol and E_{Ar19}=153.8 kJ/mol.

Regarding the pre-exponential factors, N_2 adsorbs dissociatively on the noble metal according to reverse reaction 20. N_2 does not adsorb easily on the catalytic surface. However, the activation energy calculation gave a low E_{Ar20}. Thus, to reconcile with the negligible adsorption of N_2 on the noble metals, we chose $A_{r20}=10^6$ $bar^{-1}.s^{-1}$ from the estimations of the transition state theory. Reverse reaction 19 seems even less probable since it involves three reactants, but this fact has been included in its high activation energy. We chose $A_{r19}=10^6$ $bar^{-1}.s^{-1}$ assuming the transition state of such a trimolecular reaction to be immobile. A_{r18} can then be computed from the consistency equation (4.19).

Hence, the NO-CO mechanism enabled us to determine all the missing kinetic parameters for the NO reactions. Thus, A_{r15}, A_{r17}, E_{Af15}, E_{Af17} constitute the only remaining unknowns of the NO-H_2 mechanism. As announced in the previous section, the thermodynamic consistency of this mechanism gives the two missing equations to compute these four unknowns:

$$A_{r15}^{1.5} \cdot A_{r17}^{0.5} = 7.46 \cdot 10^{26} \tag{4.22}$$

$$1.5 \cdot E_{Ar15} + 0.5 \cdot E_{Ar17} = 191.1435 \tag{4.23}$$

Solving the system (4.17, 4.22) gives A_{r15} and A_{r17} while solving the system (4.18, 4.23) gives E_{Ar15} and E_{Ar17}.

6) Water-gas shift reaction

Table 4.9: *Mechanism for the water-gas shift reaction*

Reaction	Stoichiometric number
(2) $CO + S \leftrightarrow CO^*$	1
(6) $H_2O + S \leftrightarrow H_2O^*$	1
(-17) $H_2O^* + S \leftrightarrow H^* + OH^*$	1
(21) $OH^* + CO^* \leftrightarrow COOH^* + S$	1
(14) $COOH^* \leftrightarrow CO_2 + H^*$	1
(-4) $2 \cdot H^* \leftrightarrow H_2 + 2 \cdot S$	1

In this mechanism, the kinetic parameters for reactions 14 and 21 are missing.

A_{f14} and E_{Af14} were taken from [10].

Ovesen et al [66] studied the water-gas shift reaction on a working Cu-based catalyst. In particular, they developed a kinetic model in which they compute the equilibrium constants of the elementary steps of the mechanism through the partition functions of the involved species. Although they do not consider the same mechanism as the one we do, their method can be applied to any mechanism. Thus, even though Cu shows less catalytic activity than the noble metals used in automotive converters, we used their method and their numbers to compute the kinetic parameters of reaction 21.

The equilibrium constant of reaction 21 is defined as: $K_{21} = \frac{k_{f21}}{k_{r21}}$, where k_{f21} and k_{r21} are the forward and reverse kinetic constants for reaction 21, respectively; or $K_{21} = \frac{q_{COOH^*}}{q_{OH^*} \cdot q_{CO^*}}$, where q_i is the molecular partition function of species i. The molecular partition function factorizes into one term each degree of freedom of the considered molecule: $q = q_t . q_v . q_r . q_e$, where q_t is the translational partition function, q_v the vibrational partition function, q_r the rotational partition function, and q_e the electronic partition function. Adsorbates have no rotational degree of freedom. Moreover, according to [66], their translational degrees of freedom are limited to parallel and orthogonal vibrations to the surface. Thus, $q_t = \frac{\exp\left(-\frac{1}{2}\frac{h_P \cdot \omega_\perp}{k_B \cdot .T}\right)}{1-\exp\left(-\frac{h_P \cdot \omega_\perp}{k_B \cdot .T}\right)} \cdot \frac{\exp\left(-\frac{h_P \cdot \omega_{//}}{k_B \cdot .T}\right)}{\left(1-\exp\left(-\frac{h_P \cdot \omega_{//}}{k_B \cdot .T}\right)\right)^2}$, where $\omega_\perp$ and $\omega_{//}$ are the orthogonal and parallel vibration frequencies, respectively, k_B is Boltzmann constant, h_P Planck's constant, and T the temperature of the surface. The vibrational partition function is: $q_v = \frac{\exp\left(-\frac{1}{2}\frac{h_P \cdot \omega}{k_B \cdot .T}\right)}{1-\exp\left(-\frac{h_P \cdot \omega}{k_B \cdot .T}\right)}$, and the electronic partition function $q_e = \exp\left(-\frac{E_g}{R_g \cdot T}\right)$, where E_g is the ground state energy of the molecule in J/mol.

From the vibrational frequencies and ground state energies of OH*, CO*, and COOH* ([66], [67]), K_{21} was computed at 800K:

$$K_{21} = \frac{A_{f21}}{A_{r21}} \cdot \exp\left(-\frac{\Delta H_{21}}{R_g \cdot T}\right) = 14.88 \tag{4.24}$$

On the other hand, the thermodynamic consistency of the water-gas shift mechanism gives:

$$\frac{A_{r21}}{A_{f21}} \cdot A_{r14} = 3.23.10^6 \tag{4.25}$$

$$E_{Af21} - E_{Ar21} + E_{Ar14} = -42.1 \tag{4.26}$$

From transition state theory, A_{r14} was assumed equal to 10^8 $bar^{-1}.s^{-1}$. With this assumption, Equation (4.25) gave $\frac{A_{r21}}{A_{f21}}$ and then ΔH_{21} was determined from Equation (4.24). E_{Ar14} was computed from (4.26). According to these calculations, reaction 21 is endothermic, which agrees with [68].

Moreover, E_{Af21}=41.38 kJ/mol [68] and we assumed $A_{f21}=10^{13}$ s^{-1} from transition state theory. A_{r21} and E_{Ar21} were then deduced from $\frac{A_{r21}}{A_{f21}}$ and ΔH_{21}.

7) C_3H_6-O_2 mechanism

Table 4.10: *Mechanism for the C_3H_6-O_2 reaction*

Reaction	Stoichiometric number
(1) $O_2 + 2 \cdot S \leftrightarrow 2 \cdot O*$	4.5
(3) $C_3H_6 + S \leftrightarrow C_3H_6*$	1
(8) $C_3H_6* + S \leftrightarrow C_3H_5* + H*$	1
(9) $C_3H_5* + S \leftrightarrow C_2H_4* + CH*$	1
(10) $C_2H_4* + S \leftrightarrow 2 \cdot CH_2*$	1
(11) $CH_2* + S \leftrightarrow CH* + H*$	2
(12) $CH* + O* \leftrightarrow COH* + S$	3
(13) $COH* + O* \leftrightarrow COOH* + S$	3
(14) $COOH* \leftrightarrow CO_2 + H*$	3
(15) $O* + H* \leftrightarrow OH* + S$	4
(16) $2 \cdot OH* \leftrightarrow O* + H_2O*$	1
(17) $H* + OH* \leftrightarrow H_2O* + S$	2
(-6) $H_2O* \leftrightarrow H_2O + S$	3

[10] gives $A_{f3}=4.10^8$ $bar^{-1}.s^{-1}$ and E_{Af3}=40 kJ/mol. We directly took their pre-exponential factor, but the activation energy was adapted from their data. Indeed, [10] says that C_3H_6 is the slowest adsorbing HC and declares that only considering it as representative of all the hydrocarbons underestimates the HC conversion performance of the converter. On the contrary, C_3H_6 represents the fast-oxidizing HC, and thus only considering it should overestimate the HC conversion performance of the converter. On the other hand, the adsorption activation energies for all the other included reactants have been taken as 0 kJ/mol, and Pt shows similar activities toward CO and C_3H_6 conversions. Thus, we assumed E_{Af3}=0 kJ/mol.

In absence of any experimental data on the desorption of propylene, we assumed $A_{r3}=10^{13}$ s^{-1} and $E_{Ar3}=120$ kJ/mol by analogy with CO and NO desorption energies. Anyway, the desorption activation energy has no impact on the global kinetics of C_3H_6 oxidation, as shown by the Matlab simulation of the microkinetics mechanism (see section 4.4.4 iii-).

A_{f8}, E_{Af8}, A_{f9}, E_{Af9}, A_{f10}, A_{f11}, A_{f12}, E_{Af12}, A_{f13}, and E_{Af13} were found in [10] and E_{Ar12} in [68]. The chosen E_{Af10} is the average between the values given in [10] and [56] while E_{Af11} is the average between the values given in [10] and [68].

For reverse reaction 10, [68] gives $E_{Ar10}=0$ kJ/mol on Pt whereas [56] gives $E_{Ar10}=114.95$ kJ/mol on Pd. To simulate the performance of both metals, we chose E_{Ar10} as the average of these two numbers. E_{Ar11} and E_{Ar13} are given in [68] and can also be computed from E_{Af11} and E_{Af13} and ΔH_{11} and ΔH_{13} [68]. We chose to average these two numbers.

E_{Ar8} was extrapolated based on [68] results. In fact, the data in *Hei et al* [68] enabled us to compute the heats of dehydrogenation of CH_2^* and $C_2H_6^*$: $\Delta H_{CH2^*}=46.8$ kJ/mol and $\Delta H_{C2H6^*}=12.9$ kJ/mol. These results show that the heat of dehydrogenation decreases as the hydrocarbon chain becomes larger. According to this observation, we assumed $\Delta H_8=8$ kJ/mol. This gives $E_{Ar8}=42$ kJ/mol.

E_{Ar9} can then be computed from the thermodynamic consistency of the mechanism at 800 K.

To ensure the thermodynamic consistency of the mechanism, the six remaining unknowns (A_{r8}, A_{r9}, A_{r10}, A_{r11}, A_{r12}, and A_{r13}) must satisfy:

$$A_{r8} \cdot A_{r9} \cdot A_{r10} \cdot A_{r11}{}^{2} \cdot A_{r12}{}^{3} \cdot A_{r13}{}^{3} = 3.5 \cdot 10^{142} \tag{4.27}$$

[56] (p. 129) gives the pre-exponential and activation energy for the hydrogenation of C_2H_4 into $C_2H_5^*$. Since reverse reactions 8 and 11 are hydrogenation reactions, we determined their pre-exponentials by identification with C_2H_4 hydrogenation. Indeed, the activation energy given in [56] is of the same order of magnitude as E_{Ar8} and E_{Ar9}. Hence, we chose $A_{r8}=A_{r11}=3.10^{10}$ s^{-1}.

A_{r9} was taken of the order of 10^{13} s^{-1} by analogy with the order of magnitude of the forward rate of the reaction, whereas $A_{r10}=10^{10}$ s^{-1} for reaction 10 to be significant.

We then precisely adapted A_{r9} and A_{r12} to satisfy (4.27).

8) Steam reforming reaction

Table 4.11: *Mechanism for the steam reforming reaction*

Reaction	**Stoichiometric number**
(6) $H_2O + S \leftrightarrow H_2O*$	6
(3) $C_3H_6 + S \leftrightarrow C_3H_6 *$	1
(8) $C_3H_6 * + S \leftrightarrow C_3H_5 * + H *$	1
(9) $C_3H_5 * + S \leftrightarrow C_2H_4 * + CH *$	1
(10) $C_2H_4 * + S \leftrightarrow 2 \cdot CH_2 *$	1
(11) $CH_2 * + S \leftrightarrow CH * + H *$	2
(-17) $H_2O * + S \leftrightarrow H * + OH *$	6
(22) $CH * + OH * + S \leftrightarrow CO * + 2 \cdot H *$	3
(21) $CO * + OH* \leftrightarrow COOH * + S$	3
(14) $COOH* \leftrightarrow CO_2 + H *$	3
(-4) $2 \cdot H* \leftrightarrow H_2 + 2 \cdot S$	9

Reaction 22 constitutes the only missing reaction in the steam reforming mechanism.

The thermodynamic consistency of the mechanism gives: $\frac{A_{r22}}{A_{f22}} = 1.68.10^{-8}$ and ΔH_{22}= -83.795 kJ/mol. In absence of any given data, we assumed $A_{f22}=10^{13}$ s^{-1} and E_{Af22}=30 kJ/mol.

Table 4.12 below summarizes the kinetic parameters of the forward and reverse reactions presented in Table 4.3. The units in this table are explained in the next section.

Table 4.12: *Kinetic parameters of the considered elementary reactions (see next section for explanation of the units)*

(for each reaction, the first line reports the forward parameters and the second the reverse parameters)

Reaction	A (Pa^{-1}.s^{-1} or s^{-1})*	E$_A$ (kJ/mol)	β
(1) $O_2 + 2 \cdot S \leftrightarrow 2 \cdot O*$	1.51.10^2	0	-1.987
	3.10^{13}	230	0
(2) $CO + S \leftrightarrow CO*$	2.12.10^3	0	-0.5
	10^{14}	126	0
(3) $C_3H_6 + S \leftrightarrow C_3H_6*$	4.10^3	0	0
	10^{13}	120	0
(4) $H_2 + 2 \cdot S \leftrightarrow 2 \cdot H*$	9.04.10^2	0	-0.5
	10^{13}	75	0
(5) $NO + S \leftrightarrow NO*$	10^3	0	0
	10^{13}	120	0
(6) $H_2O + S \leftrightarrow H_2O*$	10^3	0	-0.5
	10^{13}	45.1	0
(7) $CO* + O* \leftrightarrow CO_2 + 2 \cdot S$	4.5.10^{13}	101	0
	5.98.10^3	143.3	0
(8) $C_3H_6* + S \leftrightarrow C_3H_5* + H*$	8.10^{12}	50	0
	3.10^{10}	42	0
(9) $C_3H_5* + S \leftrightarrow C_2H_4* + CH*$	8.10^{13}	50	0
	10^{13}	115.09	0
(10) $C_2H_4* + S \leftrightarrow 2 \cdot CH_2*$	10^{12}	84.57	0
	10^{10}	57.48	0
(11) $CH_2* + S \leftrightarrow CH* + H*$	2.10^{12}	76	0
	3.10^{10}	29.2	0
(12) $CH* + O* \leftrightarrow COH* + S$	5.10^{13}	60	0
	7.83.10^{15}	211	0
(13) $COH* + O* \leftrightarrow COOH* + S$	10^{13}	60	0
	3.10^{13}	148.3	0

(14) $COOH^* \leftrightarrow CO_2 + H^*$	10^{13}	60	0
	10^{3}	47	0
(15) $O^* + H^* \leftrightarrow OH^* + S$	5.10^{13}	30	0
	$4.3.10^{13}$	90.17	0
(16) $2 \cdot OH^* \leftrightarrow O^* + H_2O^*$	10^{13}	63.2	0
	10^{12}	30	0
(17) $H^* + OH^* \leftrightarrow H_2O^* + S$	5.10^{13}	56	0
	$1.87.10^{11}$	97.37	0
(18) $NO^* + S \leftrightarrow N^* + O^*$	5.10^{13}	70	0
	$4.9.10^{15}$	163.02	0
(19) $NO^* + N^* \leftrightarrow N_2 + O^* + S$	10^{11}	76	-2.5
	10	153.78	0
(20) $N^* + N^* \leftrightarrow N_2 + 2 \cdot S$	$1.3.10^{11}$	84.4	0
	10	69.16	0
(21) $CO^* + OH^* \leftrightarrow COOH^* + S$	10^{13}	41.38	0
	$3.23.10^{11}$	36.5	0
(22) $CH^* + OH^* + S \leftrightarrow CO^* + 2 \cdot H^*$	10^{13}	30	0
	$1.68.10^{5}$	113.80	0

*the preexponentials of reactions involving a gaseous reactant are expressed in $Pa^{-1}.s^{-1}$, whereas those of reactions involving adsorbed reactants only are expressed in s^{-1}.

c) Units conversion

The kinetics constants reported in Table 4.12 are expressed in $Pa^{-1}.s^{-1}$ for adsorption and Eley-Rideal reactions and s^{-1} for surface reactions. They correspond to reaction rates over the active catalyst surface expressed in terms of the partial pressures of the gaseous reactants and coverages of the adsorbed species, as can be seen in Table 4.3.

To understand their meaning, let us first look at the example of surface reaction 15 between two adsorbed species: $O^* + H^* \leftrightarrow OH^* + S$. If we only consider the forward reaction, the rate of OH* production on the catalytic surface is: $\frac{d\tilde{c}_{OH^*}}{dt} = k'_{15} \cdot \tilde{c}_{O^*} \cdot \tilde{c}_{H^*}$, where $\tilde{c}_i$ is the concentration of adsorbed species i on the catalytic surface in mol/m^2 catalytic area and k'_{15} is the kinetic rate constant expressed in (m^2 catalytic area)/mol.s for the rate to be expressed in mol/(m^2 catalytic area.s). In terms of the adsorbed species coverages $\theta_i^* = \frac{\tilde{c}_i}{\tilde{c}s_0}$, the above expression becomes:

$\frac{d\theta_{OH}^*}{dt} = \left(k'_{15}\cdot\tilde{c}s_0\right)\cdot\theta_{O*}\cdot\theta_{H*} = k_{f15}\cdot\theta_{O*}\cdot\theta_{H*}$, where $k_{f15} = \left(k'_{15}\cdot\tilde{c}s_0\right)$ is the kinetic constant of reaction 15 given in Table 4.12 in s^{-1}. Note that k_{f15} depends on $\tilde{c}s_0$, the site surface density on the active catalyst materials. This density depends on the atomic arrangement of the surface. It is approximately $1.25.10^{19}$ sites/m^2, which corresponds to a site spacing of 2.8 angstroms.

For a reaction involving a gaseous reactant such as the adsorption of O_2, we shall measure the concentrations of gas species in mole/m^3 and those of surface concentrations in mole/m^2. Then: $\frac{d\tilde{c}_{O*}}{dt} = 2\cdot k'_1\cdot[O_2]\cdot\tilde{c}_S{}^2$, where $[O_2]$ is the concentration of O_2 and $\tilde{c}_S$ is the concentration of available catalytic sites per m^2 catalytic area. Or, in terms of the coverages and the partial pressure of O_2: $\frac{d\theta_O^*}{dt} = 2\cdot\left(\frac{k'_1\cdot\tilde{c}s_0}{R_g\cdot T}\right)\cdot p_{O_2}\cdot\theta_S{}^2 = 2\cdot k_{f1}\cdot p_{O_2}\cdot\theta_S{}^2$, where p_{O2} is the partial pressure of O_2 in Pa and $k_{f1} = \left(\frac{k'_1\cdot\tilde{c}s_0}{R_g\cdot T}\right)$ is the kinetic constant given in Table 4.12 in Pa^{-1}.s^{-1}.

Hence, for the rates in function of adsorbates concentrations $\tilde{c}_i$ to be expressed in mol/(m^2 catalytic area.s), the kinetic constants of surface reactions involving two reactants must be divided by $\tilde{c}s_0$, and the kinetic constants of dissociative adsorptions must be multiplied by $\frac{R_g\cdot T}{\tilde{c}s_0}$. The same approach shows that molecular adsorption kinetic constants must only be multiplied by $R_g.T$ and surface reactions involving only one adsorbed reactant do not require any conversion.

In these conversions, $\tilde{cs}_0$ depends on the atomic arrangement of the PGM particle microstructure, and is usually about constant. Hence, the constants given in Table 4.12 are fundamental numbers.

To apply the above rates, which are values on the active catalyst materials, on the gas species production/destruction rates in the monolith boundary layer, we need to convert them from mol/(m^2 catalytic area.s) to mol/(m^2 total internal area.s). Moreover, we want the rate expressions to be written in function of adsorbate concentrations based on the internal surface area and not on the catalytic area, as explained in section 4.4.3.

For a washcoat with an active catalytic area A_c and an internal surface area A^*, the adsorbate concentrations can be converted using the surface loading $\frac{A_c}{A^*}$: $[i]=\tilde{c}_i\cdot\frac{A_c}{A^*}$. Thus, for example, the fundamental rate for the dissociative adsorption of O_2 can be written: $\tilde{R}=k_{f1}\cdot\frac{R_g\cdot T}{\tilde{cs}_0}\cdot[O_2]\cdot\left(\frac{A^*}{A_c}\right)^2\cdot[S]^2$ mol/(m^2 catalytic area.s). Moreover, the fundamental rate can be converted to mol/(m^2 internal surface area.s) using the same surface loading: $R=\tilde{R}\cdot\left(\frac{A_c}{A^*}\right)=k_{f1}\cdot\frac{R_g\cdot T}{\tilde{cs}_0}\cdot[O_2]\cdot\left(\frac{A^*}{A_c}\right)\cdot[S]^2$. Therefore, the kinetic constant to use in the rate expression of reaction 1 as expressed in section 4.4.3 is: $k=k_{f1}\cdot\frac{R_g\cdot T}{\tilde{cs}_0}\cdot\frac{A^*}{A_c}=k_{f1}\cdot\frac{R_g\cdot T}{[S]_0}$, where $[S]_0$ is the average concentration of sites over the washcoat internal area.

To summarize, in the transport equations, the rates are written as described in section 4.4.3 and the kinetic constants to use in their expression must be converted from the numbers given in Table 4.12 as follows:

- *For molecular adsorptions and Eley-Rideal reactions with two reactants*

  Multiply the constant in the table by $R_g.T$

- *For dissociative adsorptions and Eley-Rideal reactions with one gaseous reactant and two adsorbed reactants*

  Multiply the constant in the table by $\frac{R_g \cdot T}{[S]_0}$
- *For surface reactions involving only one adsorbed reactant*

  No conversion is required
- *For surface reactions involving two adsorbed reactants*

  Divide the constant in the table by $[S]_0$
- *For surface reactions involving three adsorbed reactants*

  Divide the constant in the table by $[S]_0^2$

We computed $\tilde{c}s_0$ from the typical active material structure. As said earlier, the typical number of sites per m^2 of catalytic area is $1.25.10^{19}$. Then, we chose a typical catalytic area per m^3 monolith $\frac{A_c}{V} = 15000\, m^2/m^3$ -- which corresponds to a dispersion of 30% with a loading of 1.8 kg/m^3 monolith [11] -- and a typical internal area per m^3 monolith $\frac{A^*}{V} = 2 \cdot 10^7\ m^2/m^3$.

From these numbers, the average site density on the washcoat surface is $9.4.10^{15}$ /m^2. Dividing by the Avogadro's number, this value corresponds to $[S]_0 = 1.56.10^{-8}$ mol/m^2.

iii- Comparisons with global rate expressions

As explained in 4.4.4 ii-a), we used the global rate expressions given by *Koltsakis et al* [9] to discuss the consistency of the assembled set of kinetic data. The rates for the reduction of NO by CO and the steam reforming reaction require information that is not given in [9]; hence, only the expressions for the oxidation of CO, H_2, and HC were used.

$$R_{i,1-2} = \frac{A_i.\exp\left(-\frac{E_{Ai}}{R_g.T}\right) \cdot x_1 \cdot x_2}{T_s \cdot \left(1 + K_1 \cdot x_{CO} + K_2 \cdot x_{C_3H_6}\right)^2 \cdot \left(1 + K_3 \cdot x_{CO}^{\ 2} \cdot x_{C_3H_6}^{\ 2}\right) \cdot \left(1 + K_4 \cdot x_{NO}^{\ 0.7}\right)}$$

The above expression from [9] shows the Langmuir-Hinshelwood form as presented by *Voltz et al* [4]; $R_{i,1-2}$ is expressed in $mol/m^3.s$ and x_1 and x_2 are the molar fractions of the reactants (CO and O_2 for the oxidation of CO for example).

The pre-exponential and activation energy A_i and E_i were adapted experimentally and they depend on the reaction considered. As revealed by the above expression, all oxidation reactions are considered to be equally inhibited by CO, C_3H_6, and NO. The inhibition coefficients K_1, K_2, K_3, and K_4 are directly taken from *Voltz et al* [4].

Because they are experimentally fitted rate expressions, *Koltsakis et al*'s rates lump the internal diffusion process. Hence, they cannot be directly compared with our chemical mechanisms. On the other hand, as explained in section 4.3.1, the internal diffusion can be represented by an effectiveness factor, which leads to a lumped internal transport-chemical rate in the form: $R = \eta \cdot R_{intrinsic}$, where $R_{intrinsic}$ is the intrinsic chemical rate of the considered reaction. Therefore, to obtain an estimate of intrinsic global rates from *Koltsakis et al*'s expressions, we used the effectiveness factors for the CO oxidation reaction given by *Hayes and Kolaczkowski* [39]. Of course, the temperature dependence of the effectiveness factor we used is not the same as the lumped exponential dependence of the lumped expressions. Thus, we were not able to perform accurate comparisons between two intrinsic rate expressions. However, in absence of more accurate data, the estimations we made from *Koltsakis et al*'s rates enabled us to check if our kinetic parameters were of the right order of magnitude.

The kinetic simulation of the mechanisms was performed in Matlab assuming a batch reactor as represented on Figure 4.15. The reactor contains catalyst in a density of $[S]_0=1.56.10^{-8}$ mol/m^2, which is typical of automotive converters. Reactants are introduced in the reactor at t=0. The simulation reproduces the evolution of this system with time, at constant pressure and temperature. In fact, the evolution of the mixture composition with time is represented by a set of ordinary differential equations, solved using Matlab ode solver ode15S because of the stiffness of the differential equations for the detailed mechanisms. In the calculations, the external diffusion to the surface of the catalyst is neglected, and the evolution of the species concentrations is considered due to the chemical reactions only.

Since *Koltsakis et al*'s rate expressions are given in mol/m^3.s, we multiplied our rate expressions initially expressed in mol/m^2.s by $\frac{A^*}{V^*} = \frac{a_m}{\varepsilon_w \cdot (1-\varepsilon)} = \frac{2.10^7}{0.7 \cdot (1-0.7)}$ m^2/m^3.

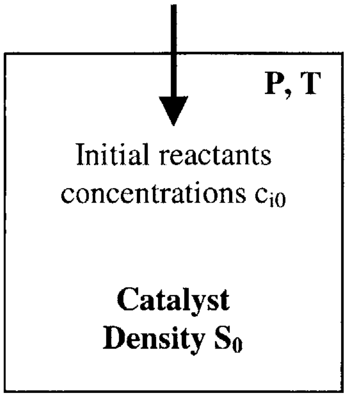

Fig. 4.15: *Batch reactor used in the chemical simulation*

We first compared the global and detailed data for the CO-O_2 mechanism. Since the detailed kinetic data for this mechanism are all confirmed, we used this reaction to determine under which conditions the comparison between the two cases appears legitimate. The agreement between the global and detailed data was then tested for the oxidation of H_2. We then studied the oxidation of C_3H_6 -- mechanism which required the largest number of assumptions in the determination of its kinetic constants -- to discuss the validity of the involved parameters.

a) Oxidation of CO

The global and detailed rate expressions were compared through the production of CO_2. Thus, the results are presented as the evolution of the CO_2 concentration with time. The resulting curves can be compared according to two criteria:

- The rate of production of CO_2, which graphically is the slope of the curve $[CO_2](t)$
- The "characteristic time" for CO_2 production, i.e. the time the system takes to reach steady state.

The global rate expression lumps the adsorption, desorption and surface reactions into one expression, whereas our rates account for all these elementary reactions. Thus, we cannot expect the production rates to be exactly the same. However, the time to reach steady-state characterizes the kinetics of the system, and is important in the prediction of the converter's behavior. Therefore, we compared the two expressions on their characteristic time.

To discuss the legitimacy of the comparison, we studied the effect of temperature and redox ratios on the computed characteristic time.

In this simulation, we did not account for C_3H_6 and NO inhibitions on the global rate expression. The mixture only includes CO, O_2, and CO_2. The initial CO level was taken as 1.1%, the initial CO_2 level as 14%, and the initial O_2 level was varied from 0.45 to 3% to affect the redox ratio (see 2).

1) Effect of the operating temperature

Figures 4.16(a) and (b) below show the characteristic time for CO_2 production as a function of temperature for the two considered rate expressions. As illustrated on Figure 4.16(a), the global rate expression is one to two orders of magnitude slower than the microkinetics mechanism at temperatures less than 850 K. In fact, *Koltsakis et al*'s rate expressions were experimentally fitted for mean operating temperatures of the converter (about 800-900 K), which explains why they cannot reproduce the actual chemical activity at low temperatures. Furthermore, the different temperature dependence between their expression and the effectiveness factor we use must accentuate this effect. The low rates predicted by *Koltsakis et al* at low temperatures may also be due to an overestimation of the inhibition of the rate by CO.

Figure 4.16(b) zooms on the 900 K region and reveals that the two characteristic times are of the same order of magnitude in this region. The microkinetic rate in this temperature range is limited by the O_2 adsorption rate, which is relatively insensitive to temperature.

Hence, our kinetic rates appear of the right order of magnitude. Moreover, the comparison between the two rate expressions appears to be valid above 800 K only.

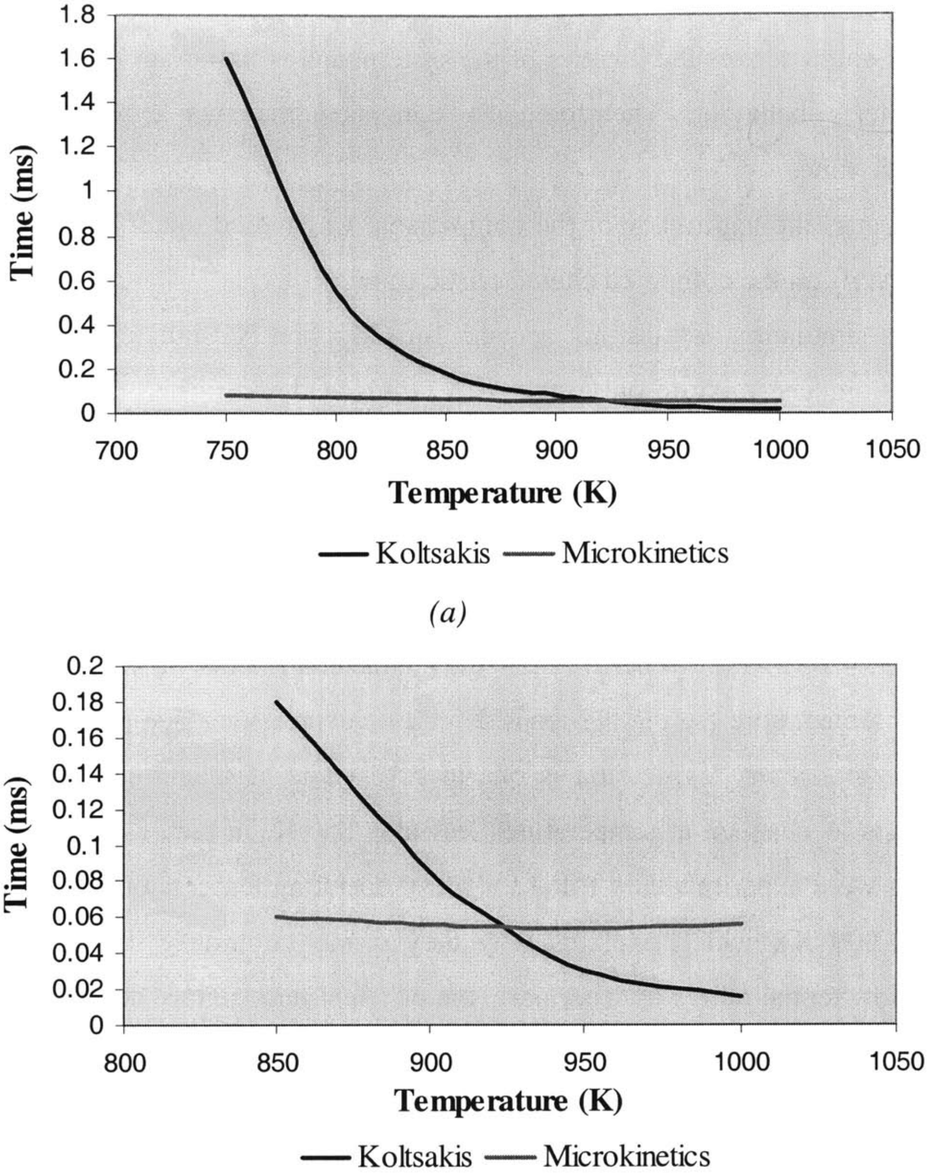

(b)

Fig. 4.16: *(a) Evolution of the characteristic time with temperature for the global and detailed mechanisms (redox=0.786); (b) same on an expanded scale*

Even when the characteristic times are the same, the rates of CO_2 production are different, *Koltsakis et al* predicting faster rates than the microkinetics model at early times (see Figure 4.17).

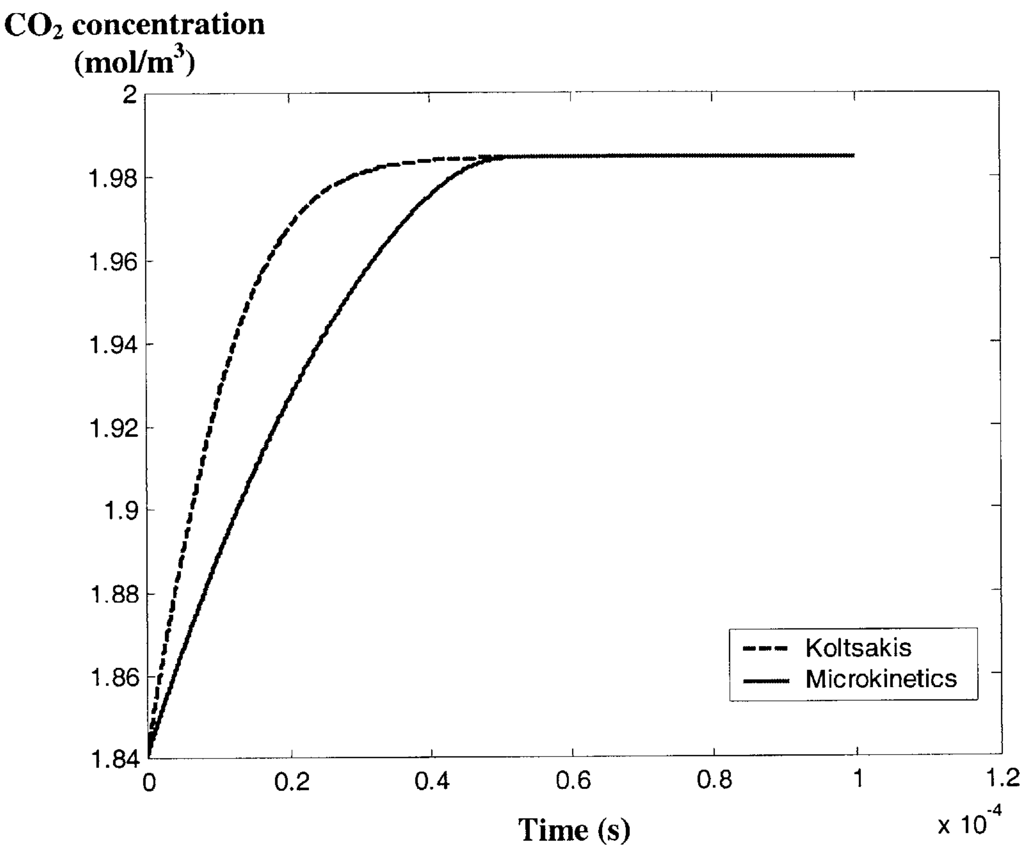

Fig. 4.17: *Evolution of the CO_2 concentration with time in the CO-O_2 mechanism for T=975 K and redox=0.786*

2) Effect of the redox ratio

The redox ratio is defined as follows: $\text{Redox} = \dfrac{x_{CO} + x_{H_2} + 6 \cdot \left(1 + \dfrac{\alpha}{4}\right) \cdot x_{HC}}{x_{NO} + 2 \cdot x_{O_2}}$, where

α is the hydrogen-to-carbon ratio of the considered hydrocarbon. We studied the effect of the redox ratio on the characteristic time to determine at which redox ratio we would perform the comparison. The redox ratio was varied by changing the O_2 level in the mixture like in [9].

As shown on Figure 4.18 at 975 K, the characteristic times of the two expressions stay close to each other whatever the redox ratio if we stay close to stoichiometry. On the contrary, we observe large discrepancies in the lean region, as illustrated on Figure 4.19. Indeed, as we operate with leaner mixtures, the rate increases, and *Koltsakis et al* seem to overestimate this increase. The exponent of the O_2 concentration in the global rate expression should probably depend on the redox ratio, which is not accounted for by *Koltsakis et al* and may be responsible for the observed difference between the two rates.

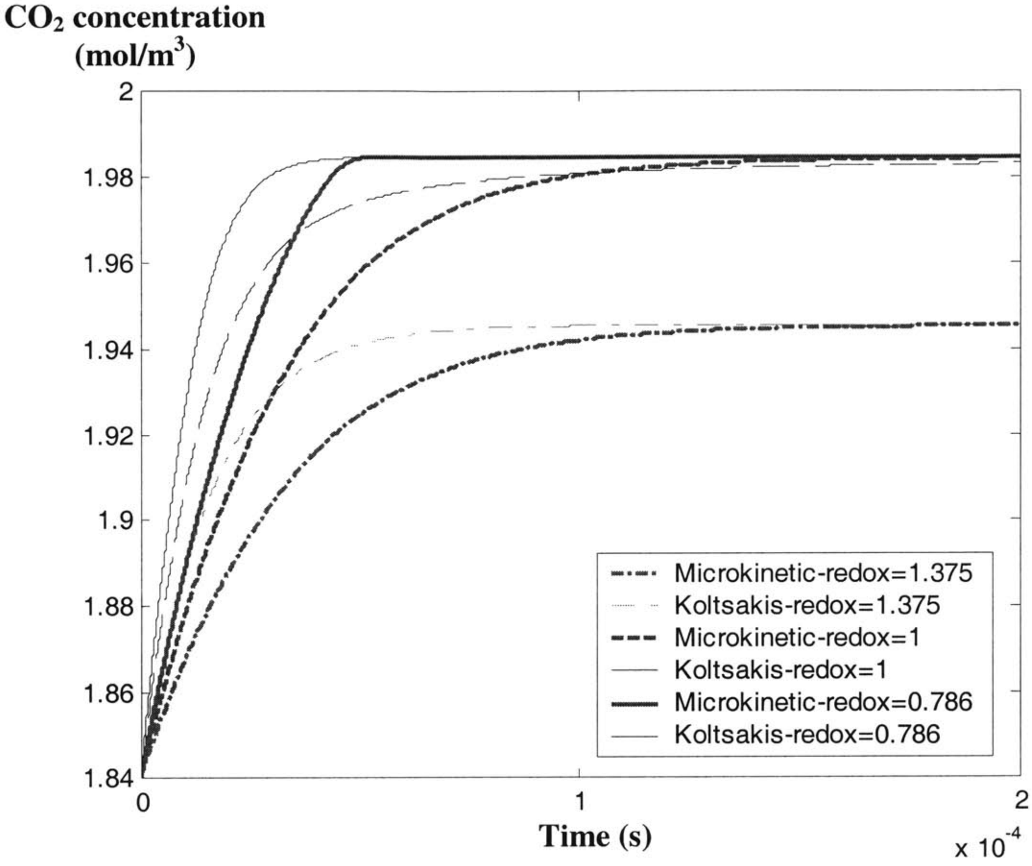

Fig. 4.18: *Evolution of the CO_2 concentration with time in the CO-O_2 mechanism for different redox ratios near stoichiometry (T=975 K)*

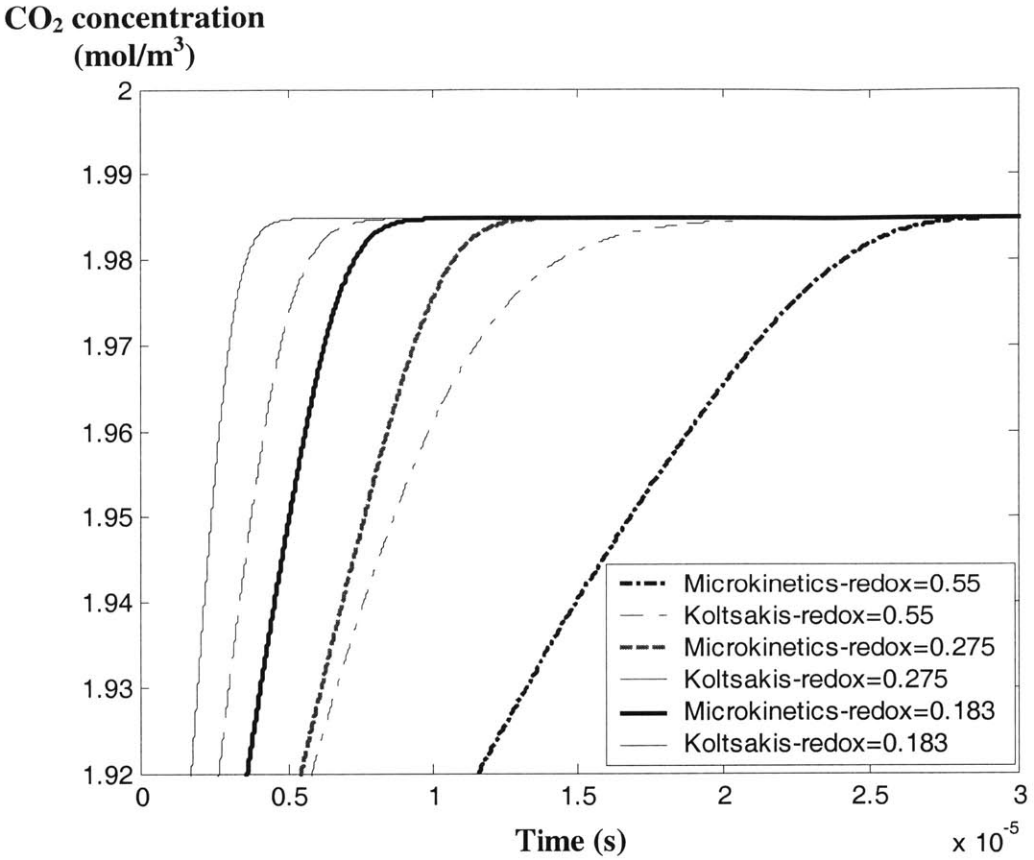

Fig. 4.19: *Evolution of the CO_2 concentration with time in the CO-O_2 mechanism for different redox ratios in the lean region (T=975 K)*

Therefore, we chose to compare the rate expressions close to stoichiometry. Nevertheless, we did not perform the simulation at stoichiometry because the global rate expression becomes very slow once the two reactant concentrations are almost zero, whereas the microkinetics model does not (see Figure 4.18, redox=1). This phenomenon appears as a limitation of the global rate expression. Thus, we used a redox ratio of 0.786 (level of CO=1.1% and level of O_2=0.7%).

b) Oxidation of H_2

The simulation was performed with an initial mixture containing 1.1% H_2, 0.7% O_2, and 10% H_2O. The inhibitions of the global rate by CO, C_3H_6, and NO were thus not considered.

The global and microkinetics rate expressions predict the same characteristic time for T=840 K, as illustrated on Figure 4.20 below.

However, in this particular case, the two rate expressions do not lead to the same steady-state level. This difference is due to the easy H_2O adsorption and the resulting surface reactions the adsorbed H_2O^* undergoes on the surface. We did not observe such a phenomenon for the CO-O_2 reaction since CO_2 adsorption on the surface is negligible. This prediction of the detailed microkinetics mechanism will be further discussed in section 5.3.

If we consider the characteristic time as the time required to reach the maximum level of H_2O concentrations, the two approaches agree for a higher temperature T=930 K.

Hence, the global and detailed rate expressions for the oxidation of H_2 agree with each other in the same range of temperatures as for the CO-O_2 mechanism.

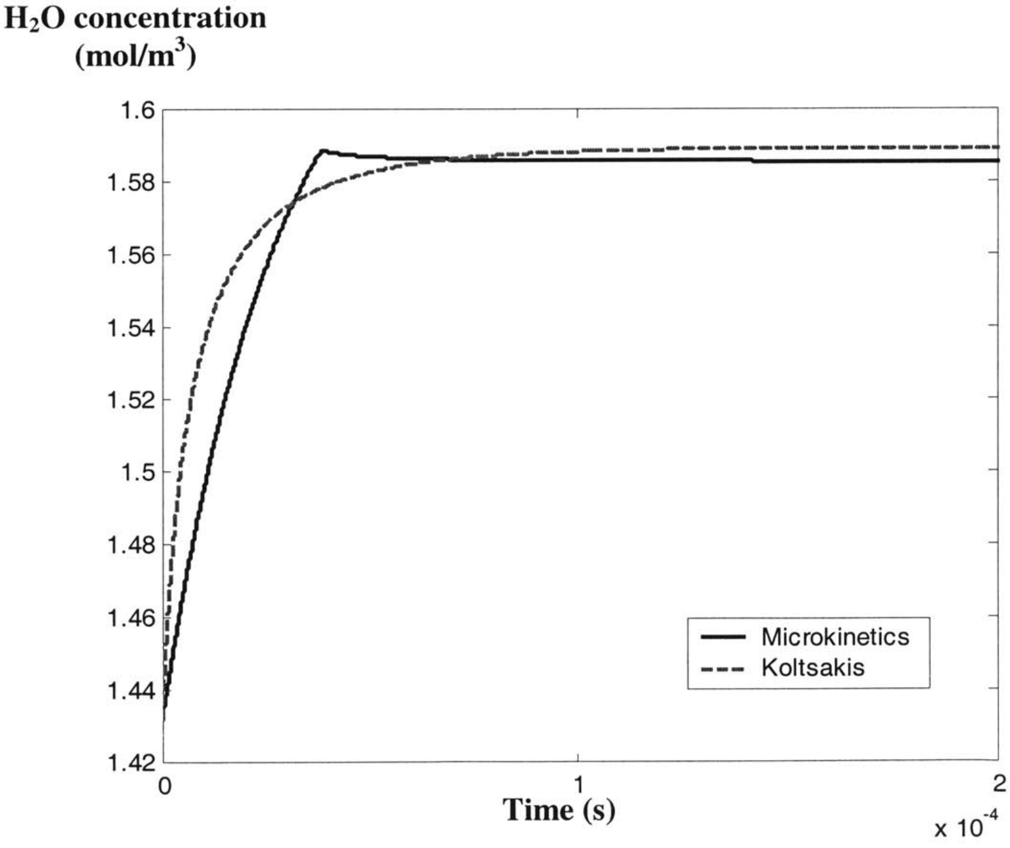

Fig. 4.20: *Evolution of the H_2O concentration with time in the H_2-O_2 mechanism at 840 K.*

c) Oxidation of C_3H_6

The determination of the required kinetic parameters for the oxidation of C_3H_6 required several assumptions. In particular, we qualitatively assumed the adsorption and desorption energies. We compared the obtained set of kinetic data to the corresponding global rate expression to check if all these assumptions resulted in acceptable kinetic predictions.

As previously said, we assumed an activation energy for C_3H_6 adsorption of 0 kJ/mol and an activation energy for its desorption of 120 kJ/mol. With these numbers, the global reaction and the microkinetics mechanism show comparable kinetics for temperatures about 900 K (the characteristic times are exactly the same for T=878 K), as illustrated on Figure 4.21. Thus, the characteristic times agree in the same range of temperatures as for the CO-O_2 and H_2-O_2 mechanisms. Hence, the assumptions we made seem acceptable.

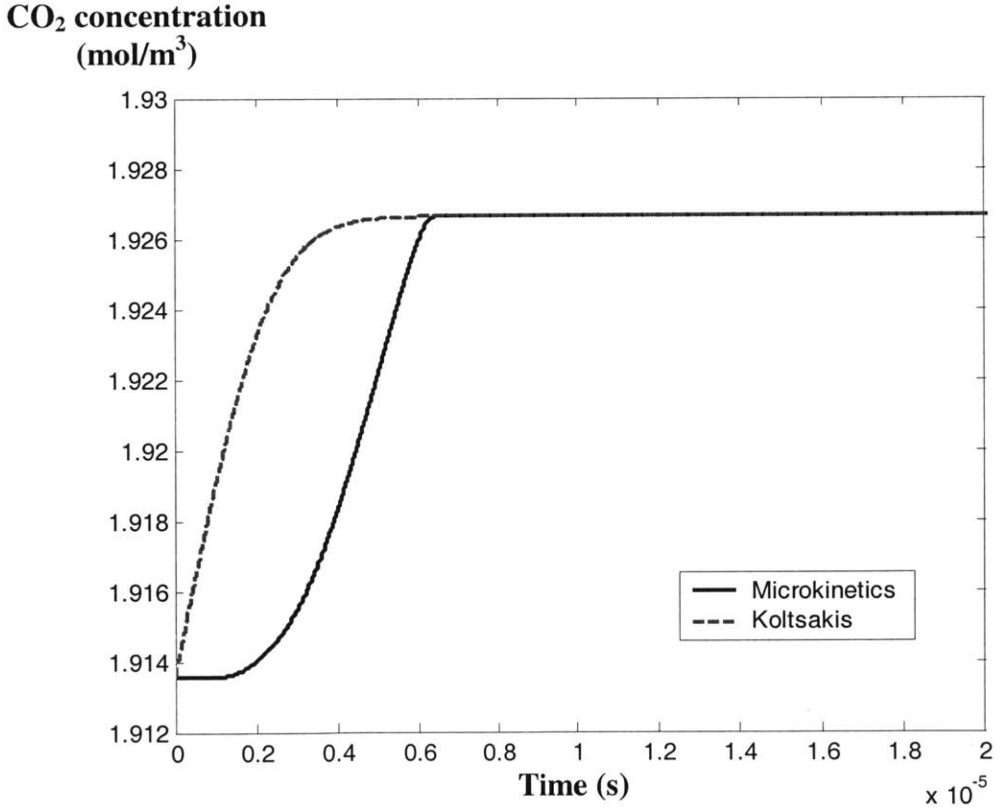

Fig. 4.21: *Evolution of the CO_2 concentration with time in the C_3H_6-O_2 mechanism (T=880 K, E_{Af3}=0 kJ/mol, E_{Ar3}=120 kJ/mol)*

Among the assumed numbers, the desorption activation energy of C_3H_6 was particularly uncertain. Thus, we varied it to see its impact on the global kinetics of the oxidation of propylene. Figure 4.22 shows the CO_2 production as a function of time at 880 K for E_{Ar3}=40 kJ/mol. The comparison between this figure and Figure 4.22 shows that, at high temperatures, the desorption activation energy has no effect on the global kinetics of the mechanism. At this temperature, the global mechanism is limited by O_2 adsorption. At lower temperatures (T=500 K), the desorption activation energy also shows no influence on the global kinetics of the mechanism. The formation of CO_2 is then limited by the surface reactions involving the intermediate hydrocarbons.

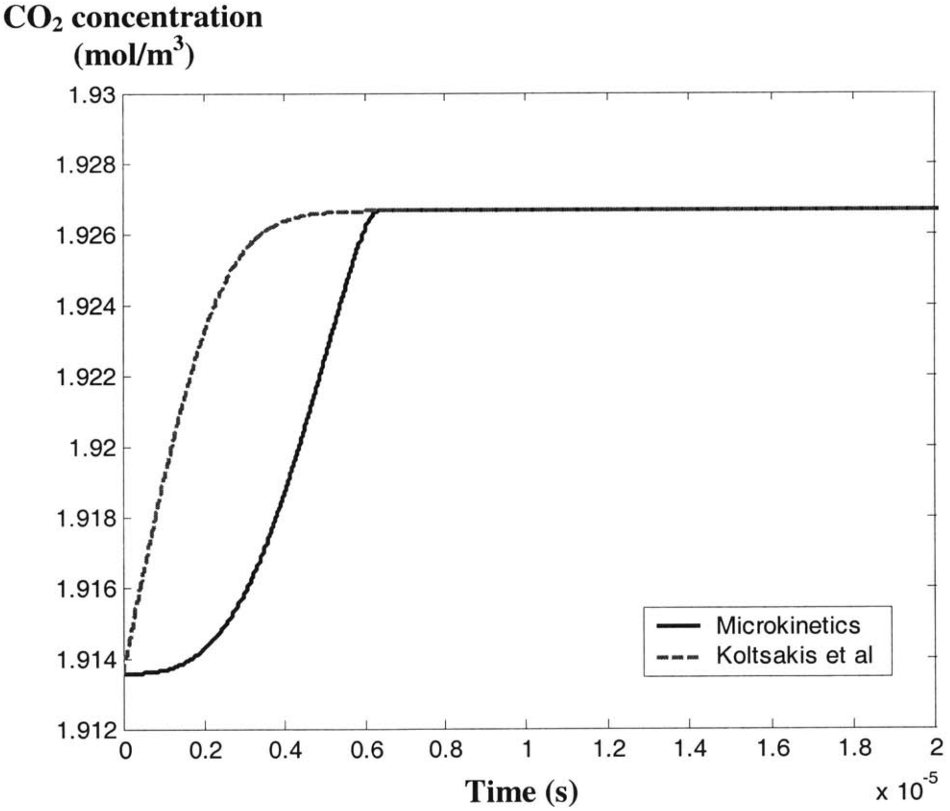

Fig. 4.22: *Evolution of the CO_2 concentration with time in the C_3H_6-O_2 mechanism (T=880 K, E_{Af3}=0 kJ/mol, E_{Ar3}=40 kJ/mol)*

4.5 Oxygen storage process

The oxygen storage process constitutes the only support-noble metals interaction accounted for in this model.

4.5.1 Modeling approach

As discussed in section 3.2.2 iii-, the oxygen storage process occurs under two forms:

- the ceria surface is oxidized and reduced by species initially adsorbed on the noble metals, which involves the spillover and reverse spillover phenomena
- the ceria surface is directly oxidized and reduced by gaseous species present in the environment.

According to experimental observations, the direct oxidation is possible only at high temperatures, above 350 C for the oxidation of ceria by O_2, whereas the spillover oxygen storage occurs under all temperatures encountered during the converter operation. We found no clear information on the relative importance of these two pathways when both are significant. We thus accounted for both to simulate the converter's behavior on the whole range of operating temperatures.

The reduced form of ceria Ce_2O_3 can be oxidized by O_2, NO, H_2O, and CO_2. Among those, O_2 and H_2O are the strongest oxidizing species [69]. However, by lack of information about the oxidation by H_2O, we only accounted for the oxidation of ceria by O_2. Thus, the oxidation of ceria was modeled by reactions (23) and (24) below:

$$(23)\ \mathrm{Ce_2O_3} + \mathrm{O}^* \rightarrow 2\cdot\mathrm{CeO_2} + \mathrm{S}$$

$$(24)\ \mathrm{Ce_2O_3} + 0.5\cdot\mathrm{O_2} \rightarrow 2\cdot\mathrm{CeO_2}$$

The oxidized form of ceria CeO_2 can be reduced by CO, H_2, and HC. In fact, H_2 is the best reducing species, then comes CO, and HC is last [24]. The interaction of propylene with ceria is indeed weak [69]. By lack of information on the reduction by H_2, the reduction of ceria was modeled by reactions (25) and (26) below:

$$(25)\ 2\cdot\mathrm{CeO_2} + \mathrm{CO}^* \rightarrow \mathrm{Ce_2O_3} + \mathrm{CO_2} + \mathrm{S}$$

$$(26)\ 2\cdot\mathrm{CeO_2} + \mathrm{CO} \rightarrow \mathrm{Ce_2O_3} + \mathrm{CO_2}$$

The four above equations are considered in their forward way only, the two first accounting for the oxidation and the two second for the reduction of ceria.

In fact, the noble metals are also responsible for a small fraction of the oxygen storage capacity of the catalyst ([24], [69]). Indeed, Pt adsorbs oxygen on its surface, and Pd and Rh can even form bulk oxides [70]. However, the loading of noble metals is small compared to the loading of ceria, and the participation of the noble metals in oxygen storage is rather low and can be neglected.

4.5.2 Kinetic constants

i- Assumptions

As for the main catalytic reactions, the kinetic constants are searched under the form $k = A \cdot \exp\left(-\frac{E_A}{R_g \cdot T}\right)$.

For spillover reactions, the surface diffusion is lumped into the kinetic constants. Indeed, the diffusion of the adsorbate from the noble metal to the ceria surface is fast compared to the chemical oxidation or reduction reactions.

ii- Determination of the kinetic constants

a) Approach

A_{25}, E_{A25}, and E_{A26} were taken from [57]. E_{A23} and E_{A24} were adapted from the previous numbers, whereas A_{26}, A_{23}, and A_{24} were adapted by comparing the microkinetics mechanism to the oxygen storage submodel proposed by *Koltsakis et al* and using [69].

We compared the global and microkinetics reduction and oxidation rates using the same type of simulation as explained in section 4.4.4 iii-. To compare the reduction rates, we chose an initial reactor mixture containing CO only with an initially all oxidized ceria surface. The oxidation rates were compared with an initial mixture containing O_2 only and an initially all reduced ceria surface.

Koltsakis et al consider that the oxygen storage of the catalyst occurs according to the following reaction: $2\,CeO_2 \leftrightarrow Ce_2O_3 + 0.5.O_2$. Although CO does not appear responsible for the reduction of ceria in this equation, the reduction rate they propose depends on the CO mole fraction: $R_{red,K} = k_{red}(T) \cdot x_{CO} \cdot OSC \cdot \psi$, where ψ is the extent of oxidation of ceria or auxiliary number defined as $\psi = \frac{2 \cdot \text{moles}\, CeO_2}{2 \cdot \text{moles}\, CeO_2 + \text{moles}\, Ce_2O_3}$, and OSC is the total oxygen storage capacity of the catalyst in mol/m^3. Their global oxidation rate linearly depends on the oxygen mole fraction as follows: $R_{ox,K} = k_{ox}(T) \cdot x_{O_2} \cdot OSC \cdot (1-\psi)$. The variation of the oxidation extent ψ follows the equation $\frac{d\psi}{dt} = -\frac{R_{red}}{OSC} + \frac{R_{ox}}{OSC}$.

Therefore, the simulation of *Koltsakis et al*'s oxygen storage submodel includes five differential equations, accounting for the variation of [CO], [O_2], the concentration of stored oxygen [<O>] --equivalent to 0.5 [CeO_2]--, the concentration of available storage sites [< >] -- equivalent to [Ce_2O_3]--, and ψ.

In the expressions of the microkinetics rates, 2.CeO_2 was also represented by a stored oxygen atom <O> and Ce_2O_3 by a vacant oxygen storage site < >. The microkinetics rates thus are:

$$R_{red,m} = k_{26} \cdot [<O>] \cdot [CO] + k_{25} \cdot [<O>] \cdot [S]_0 \cdot \theta_{CO}^*$$

$$R_{ox,m} = k_{24} \cdot [<>] \cdot [O_2] + k_{23} \cdot [<>] \cdot [S]_0 \cdot \theta_O^*.$$

In the oxidation rate, we chose a linear dependence on the O_2 concentration according to *Koltsakis et al* and other previously developed oxygen storage submodels [7]. Indeed, reactions 24 and 26 are not elementary reactions and the exponents of the reactants concentrations are thus not necessarily their stoichiometric coefficients.

The microkinetics oxygen storage submodel is thus represented by four differential equations, accounting for the variation of [CO], [O_2], [<O>], and [< >].

The concentrations of stored oxygen <O> and vacant sites < > are expressed in mol/m^2 surface area in our model. However, they are expressed in mol/m^3 in *Koltsakis et al*'s submodel. To compare the results of the two simulations, our surface concentrations were converted to volume concentrations using the same conversion factor as before $\frac{A^*}{V^*} = \frac{a_m}{\varepsilon_w \cdot (1-\varepsilon)} = \frac{2.10^7}{0.7 \cdot (1-0.7)}$ m^2/m^3 (see next section).

b) Reduction reactions

According to [57], the rate of CO_2 formation by reaction 25 on a pelleted supported platinum catalyst is:

$$r_{CO_2,Pt-ceria} = A'_{25} \cdot \exp\left(-\frac{E_{A25}}{R_g \cdot T}\right) \cdot \theta_{CO}{}^* \cdot \theta_O \text{ mol/(s - m Pt perimeter)}$$

where $\theta_{CO}{}^*$ is the fractional coverage of CO* on the active catalytic surface

θ_O is the fractional coverage of oxygen on the available oxygen storage sites

A'_{25}=1.455.10^{-14} mol/(s-m Pt perimeter) where the unit is mole per sec per meter of Pt perimeter

E_{A25}= 1000 J/mol.

The unusual units for this rate are fundamental units for such a spillover reaction.

First, the above rate corresponds to a pelleted catalyst and not to a monolith. *Voltz et al* [4] studied the difference in kinetic behavior between monoliths and pelleted catalysts and concluded that kinetic constants determined from pelleted catalysts need to be multiplied by a factor 1.5 to apply to monolithic catalysts. We used this conversion factor here, and thus considered as our fundamental pre-exponential for reaction 25 A_{25}=2.1825 mol/(s - m Pt perimeter).

From this fundamental number, the rate can be converted to mol/(s.m^2 internal area) using formula (4.28) computing the Pt perimeter per m^2 support for a given catalyst:

$$I_0 = \frac{5 \cdot 10^{14} \cdot x_{Pt} \cdot Disp^2}{BET_{ceria}} \tag{4.28}$$

where I_0 is the Pt perimeter in m/m^2 support

x_{Pt} is the noble metal loading

Disp is the metal dispersion

BET_{ceria} is the ceria surface area in m^2/kg; the term BET stands for Brunauer-Emmett-Teller and refers to the method used to measure the surface area.

Furthermore, the above reaction rate is expressed in terms of the coverages of CO* and <O> instead of their concentrations.

Therefore, the rate to be used in any converter simulation is:

$$R_{25} = \frac{A_{25} \cdot I_0}{[S]_0 \cdot OSC} \cdot \exp\left(-\frac{E_{A25}}{R_g \cdot T} \right) \cdot [CO^*] \cdot [<O>] \, \text{mol}/\left(\text{s.m}^2 \text{ internal area}\right)$$

where $[S]_0$ is the surface density of catalytic sites in mol/m^2 internal area and OSC is the oxygen storage capacity or total concentration of available storage sites in mol/m^2 internal area. In the computation of the perimeter I_0, we used a typical ceria surface area of 17 m^2/g catalyst [12].

In our simulation, for the rates to be expressed in mol/m^3.s as in *Koltsakis et al*, we converted $[S]_0$ and OSC to mol/m^3, as well as the rate expressions, using $\frac{A^*}{V^*}$ as the conversion factor. The oxygen storage capacity of the catalyst was taken as the value given by *Koltsakis et al*: OSC=10 mol/m^3.

[57] also gives the pre-exponential and activation energy for the reaction: $CO + 2 \cdot CeO_2 \leftrightarrow Ce_2O_3 + CO_2 \text{ -ceria}$. In our model, CO_2 is directly formed under the gaseous form by the direct exchange between CO and oxidized ceria. Hence, reaction 26 does not exactly correspond to the above reaction. Nevertheless, we assumed the activation energy to be of the same order of magnitude: E_{A26}=100 kJ/mol.

Comparing the reduction rate obtained by reaction 25 only to *Koltsakis et al*'s reduction rate, we observed that these two rates are exactly the same at T=629 K=356 C. R_{25} is slower than $R_{red,K}$ above this temperature and faster under. This behavior, as well as the high activation energy for reaction 26, agrees with previously reported experimental observations: under a low temperature of about 350 C, the oxygen storage process only occurs through a noble-metal assisted spillover reaction, whereas above this temperature, the direct pathway becomes important.

We fitted A_{26} for R_{25}+R_{26} to be of the same order of magnitude than *Koltsakis et al*'s rate at 850 K: A_{26}=5.10^5 Pa^{-1}.s^{-1} (see Figure 4.23).

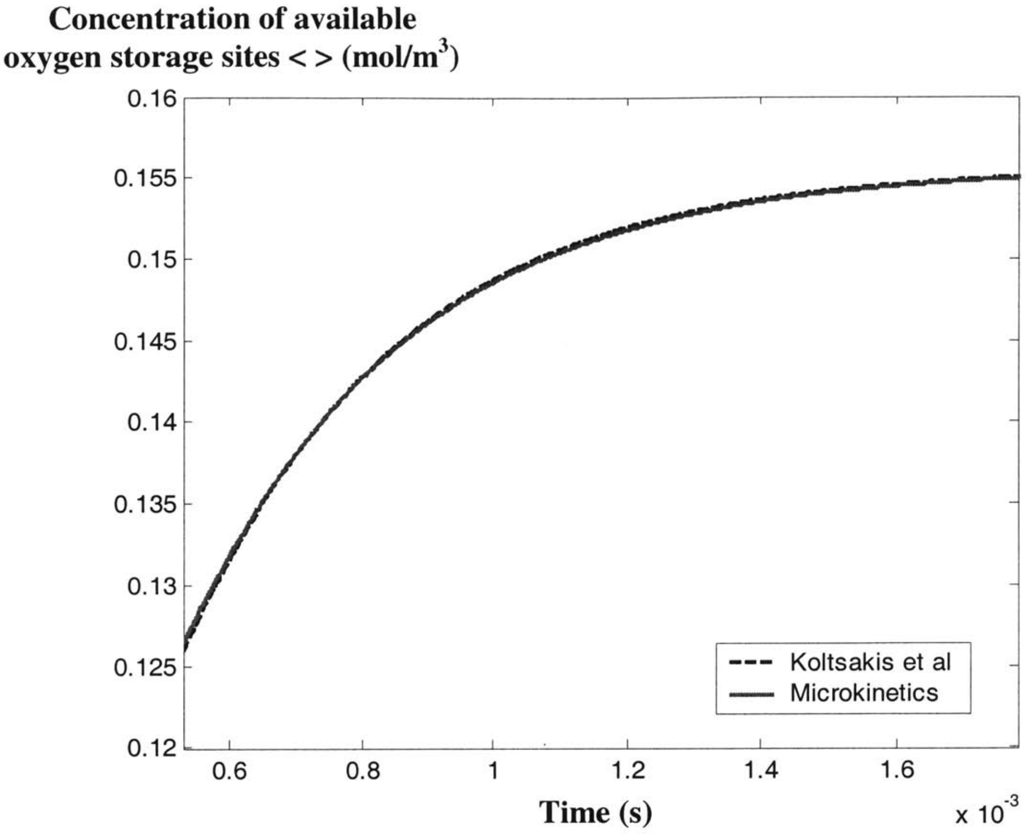

Fig. 4.23: *Evolution of the concentration of available storage sites with time for Koltsakis et al's and the microkinetics ceria reduction at 850 K*

Knowing all the kinetic parameters of the microkinetics mechanism, we have been able to study its behavior and to compare it to *Koltsakis et al*'s submodel on the whole range of temperatures. At low temperatures (below 356 C), the reduction of ceria occurs through the spillover pathway only and the resulting reduction rate is higher than the one predicted by *Koltsakis et al*, as illustrated on Figure 4.24.

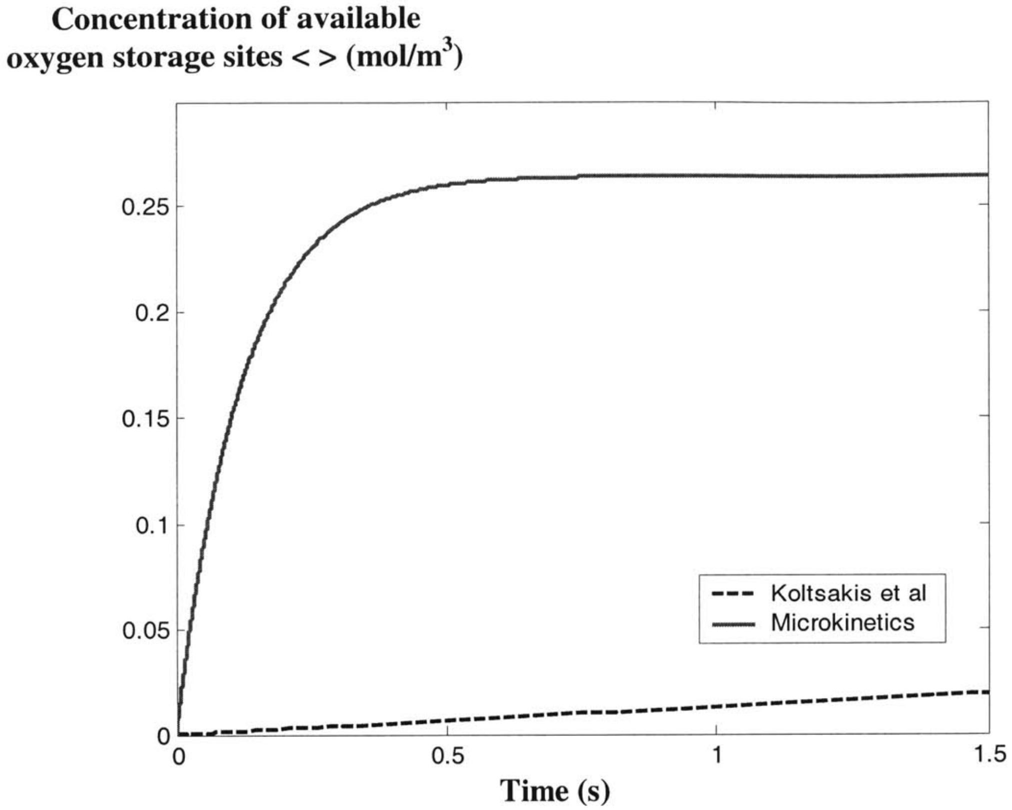

Fig. 4.24: *Evolution of the concentration of available storage sites with time for Koltsakis et al's and the microkinetics ceria reduction at 500 K*

As the temperature increases, the spillover rate stays of the same order of magnitude due to its low activation energy whereas R_{26} increases exponentially. Hence, we observe an intermediate range of temperatures (about 650-700 K) in which the spillover rate and the direct reduction rate are of the same order of magnitude, and as the temperature further increases, the direct reduction pathway becomes the dominant reduction pathway. Figure 4.25 reveals the difference between the two pathways at 750 K. As the temperature further increases (above 800 K), the spillover pathway becomes insignificant, and microkinetics and *Koltsakis et al* predict rates of the same order of magnitude (see Figure 4.23).

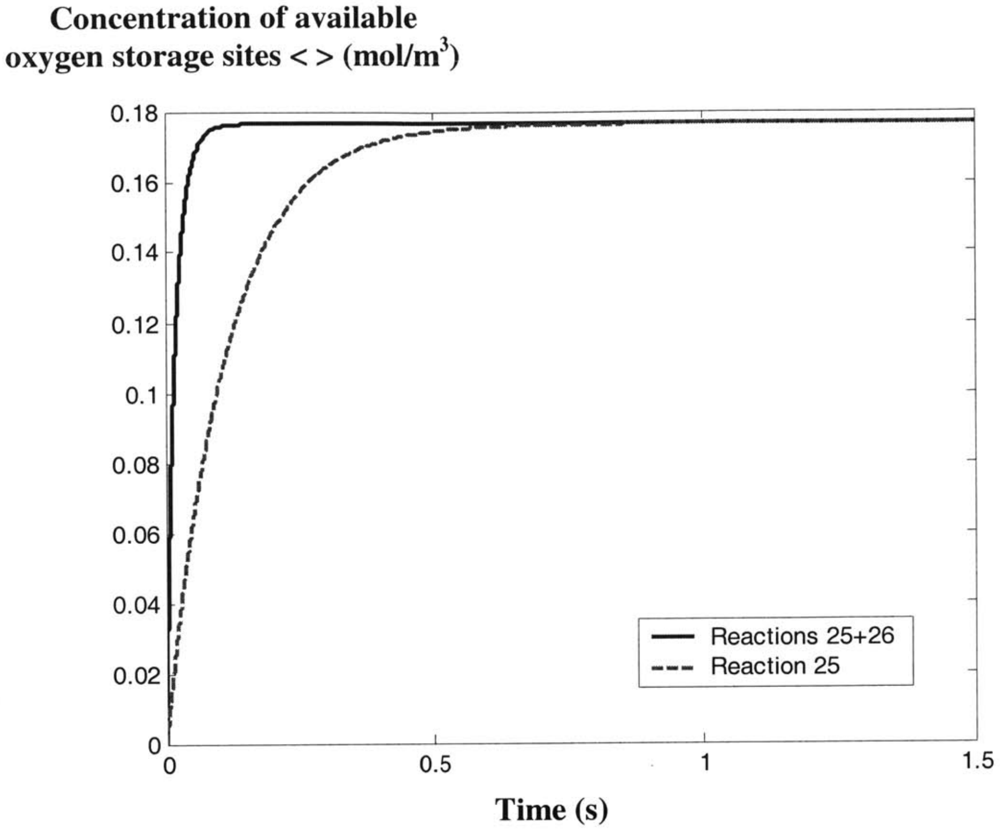

Fig. 4.25: *Relative importance of reactions 25 and 26 on the reduction of ceria at 850 K*

Therefore, the microkinetics submodel for the reduction of ceria leads to two conclusions:

- Global rate expressions that have been used in previous models were fitted on experimental data at temperatures above 800 K and do not account for the oxygen storage function of the catalyst at low temperatures.
- At temperatures higher than about 350-400 C, the direct reduction pathway dominates even though both spillover and direct pathways occur.

The latter behavior is probably observed because we only consider the spillover reduction of ceria by CO*, which is not a very fast diffusing species. On the contrary, H* is a fast diffusing species, and therefore the spillover reduction by H* probably dominates the direct reduction by H_2 at any temperature. The difference between these two behaviors highlights the need to include the reduction of ceria by H* in the model.

c) Oxidation reactions

E_{A23} was taken as 1 kJ/mol by analogy with reaction 25. Indeed, as a spillover reaction, reaction 23 must occur over the whole range of operating temperatures. On the contrary, according to physical observations, reaction 24 only occurs above a temperature of about 350 C [25]. Therefore, we chose E_{A24}=100 kJ/mol.

The two remaining parameters A_{23} and A_{24} were determined according to the following criteria:

- The microkinetics mechanism must predict an evolution of the concentration of stored oxygen with time of the same shape as the one predicted by Koltsakis et al (see below).
- The microkinetics mechanism must predict an evolution of the concentration of stored oxygen with time of the same order of magnitude as the one predicted by *Koltsakis et al* for temperatures about 800 K (like for the other mechanisms).
- The oxidation of the reduced ceria surface must be faster than the reduction of the oxidized ceria surface, according to *Herz* [69]. *Herz* studied the time the catalyst needed to be oxidized and reduced with rich-to-lean and lean-to-rich step experiments at 770 K, respectively. These experiments showed that the washcoat surface is completely oxidized after 1 s, whereas it is only 36% reduced after 0.5 s. In other words, the oxidation of the ceria surface is about 5 times faster than its reduction.

We first assumed A_{23} =2.1825.10^{-14} mol/mPt perimeter.s, like A_{25}. We then tried to fit the pre-exponential A_{24} for the microkinetics and global rates to agree at T=850 K, like for the reduction reactions. However, increasing A_{24} to get the right characteristic time introduced an unlikely behavior illustrated on Figure 4.26.

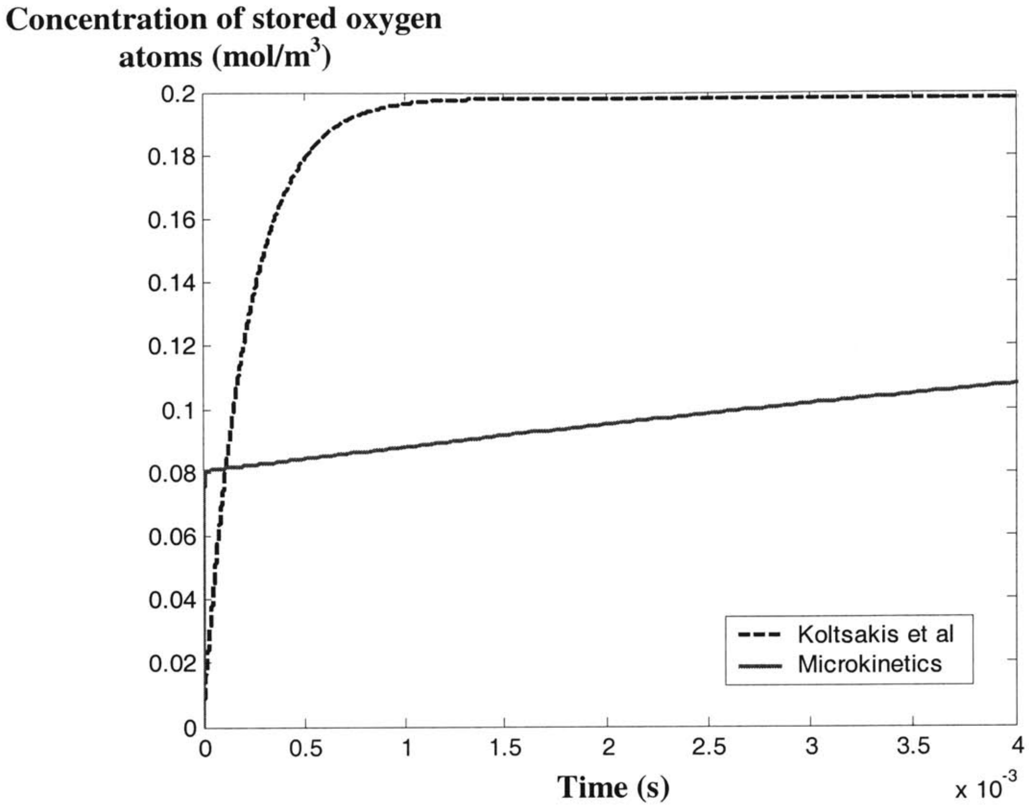

Fig. 4.26: *Evolution of the concentration of stored oxygen atoms with time at 800 K with* $A_{23}=A_{25}$ *and* $A_{24}=5.10^6\ Pa^{-1}.s^{-1}$

As can be seen, if reaction 24 is too fast compared to reaction 23, the oxidation of ceria occurs in two phases: first, part of the oxygen present in the ambient rapidly reacts with ceria directly while the remaining oxygen adsorbs on the catalytic surface. The desorption of O_2 being negligible on the noble metals, the adsorbed oxygen atoms slowly undergo the spillover reaction, which corresponds to the second part of the oxidation and limits the whole process. This behavior is unlikely compared to the behavior predicted by *Koltsakis et al.* Hence, we chose $A_{24}=10^5\ s^{-1}$ and adapted A_{23} to get an acceptable characteristic time as well as a faster oxidation than reduction of ceria, as described below.

The reduction and oxidation rates were compared at 770K. The reduction was simulated with a completely oxidized ceria surface exposed to an initial mixture containing 1.4% CO. The oxidation was simulated with a completely reduced ceria surface exposed to an initial mixture containing 0.7% O_2. As previously said, according to *Herz*'s experiments, the oxidation is about 5 times faster than the reduction of ceria at 770K. Even though our simulation does not correspond exactly to *Herz*'s experiments, we fitted A_{23} for the reduction characteristic time to be about 5 times larger than the oxidation characteristic time. We obtained these proportions for $A_{23}=2.619.10^{-13}$ mol/(mPt perimeter.s), as shown on Figure 4.27 below. With this number, *Koltsakis et al*'s rate expression and the microkinetics modeling predict the same characteristic time for T=800 K, which is of the same order as for the other mechanisms.

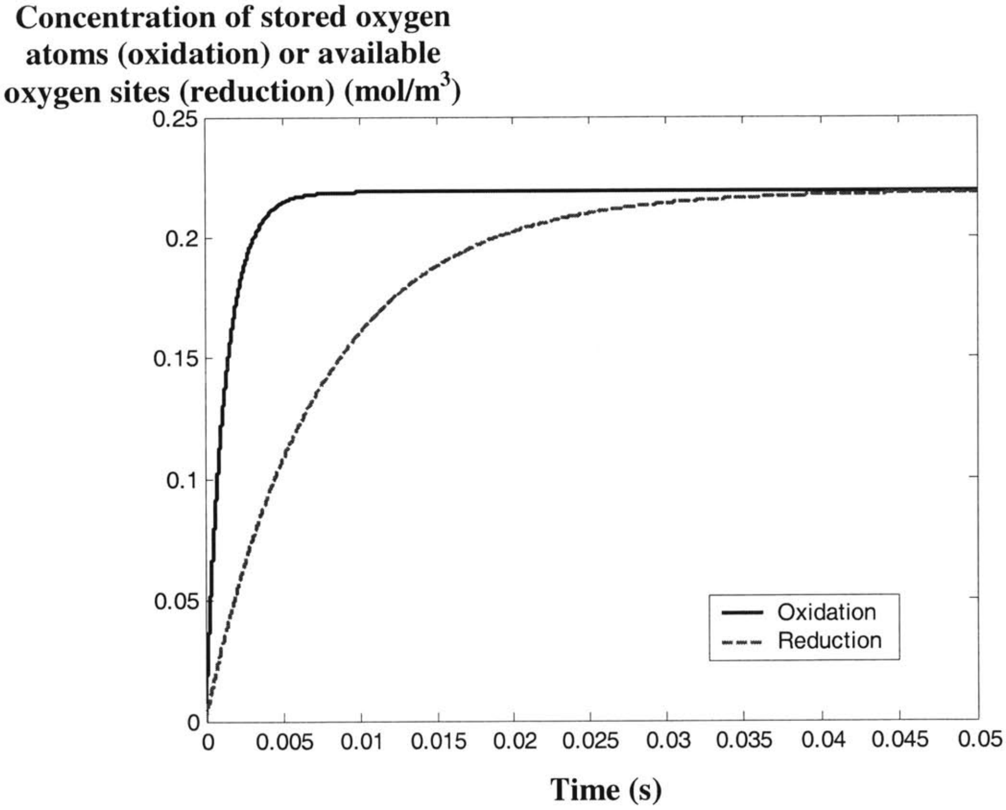

Fig. 4.27: *Comparison of the oxidation and reduction rates of ceria at 770 K*

Like for the reduction of ceria, the microkinetics model predicts a fast rate of oxidation even at low temperatures, unlike the global modeling (see Figure 4.28).

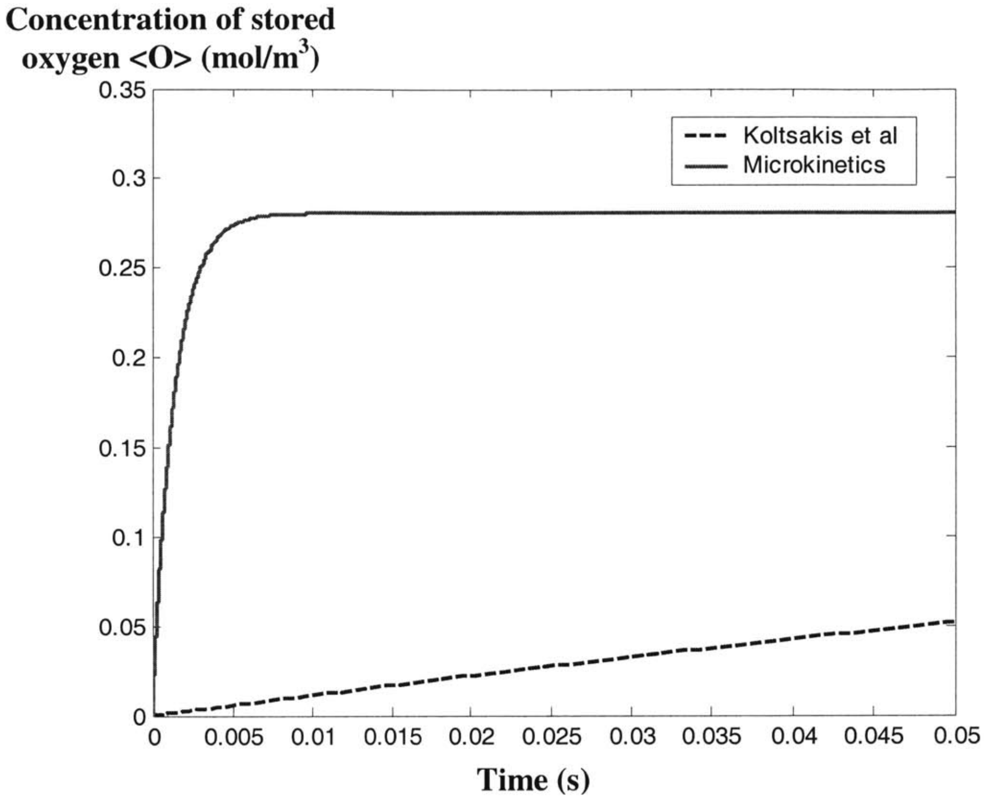

Fig. 4.28: *Evolution of the concentration of stored oxygen atoms with time at 600 K*

Moreover, in our model, the oxidation of ceria is determined by the spillover pathway on the whole range of temperatures unlike the reduction of ceria. Indeed, the direct pathway does not occur below about 400 C, and the overall oxidation reaction is limited by the spillover reaction at higher temperatures, due to the rapid adsorption of O_2 compared to reaction 24. In fact, reaction 24 appears as a minor pathway to the oxidation of ceria: Figure 4.29 shows that even at relatively high temperatures, reaction 24 is negligible.

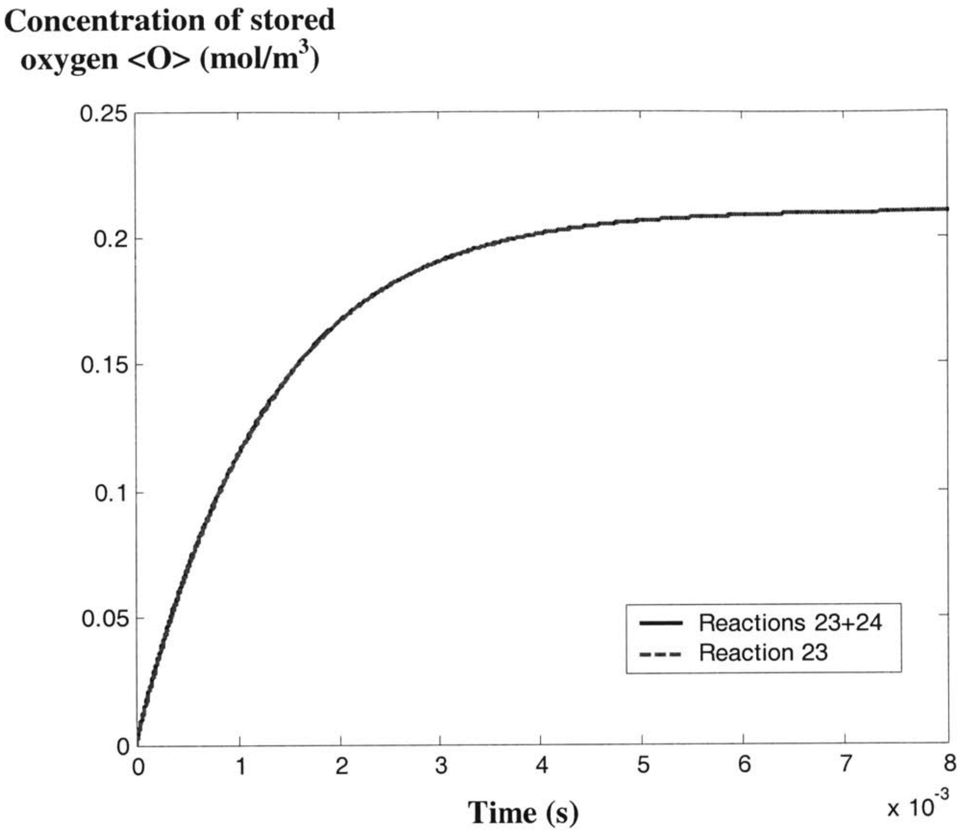

Fig. 4.29: *Relative importance of reactions 23 and 24 on the oxidation of ceria at T=800 K*

Chapter 5: Physical understanding of converters chemical processes

We performed Matlab simulations like the ones described in section 4.4.4 iii- to check that the assembled chemical data were in agreement with physical expectations. These simulations also enabled us to identify qualitative trends that are not predicted by global rate expressions and thus show the importance of accounting for the detail of the elementary reactions.

5.1 The chemical limiting process

As demonstrated in section 4.2, the overall chemical process (including chemical reactions only and not transport processes) is limited by the surface reactions at low temperatures and by the adsorption reactions at high temperatures. The simulation of the CO-O_2 mechanism at different temperatures further illustrates this behavior (see Figure 5.1 and 5.2 at 450 and 900 K, respectively).

In this simulation, we considered an initial mixture containing 1.1% CO, 0.7% O_2, and 14% CO_2.

At 900 K, the coverage of O* stays low until no more CO* is present on the surface. Indeed, at this temperature, CO adsorption and the surface reaction between O* and CO* are fast, and O_2 adsorption limits the heterogeneous process. Thus, as soon as some O* form on the surface, they immediately react due to the high rate of the CO*-O* reaction and the high CO* coverage. As CO* disappears, the rate of the surface reaction decreases, enabling the adsorbed O* to stay longer on the surface without reacting, and thus to accumulate.

At 450 K, the coverage of O* no longer stays low until the reaction reaches its steady-state. On the contrary, O* accumulates on the surface even as the reaction proceeds because the surface reaction now limits the heterogeneous process. This is traduced by the presence of a maximum on the O* coverage curve, as can also be observed on the curve of CO* coverage at 450 K, as well as 900 K.

The different chemical regimes also appear on the CO_2 production curve: at 450 K, the $[CO_2]$ curve presents an important delay at early times before the rate becomes significant, which we do not observe at higher temperatures.

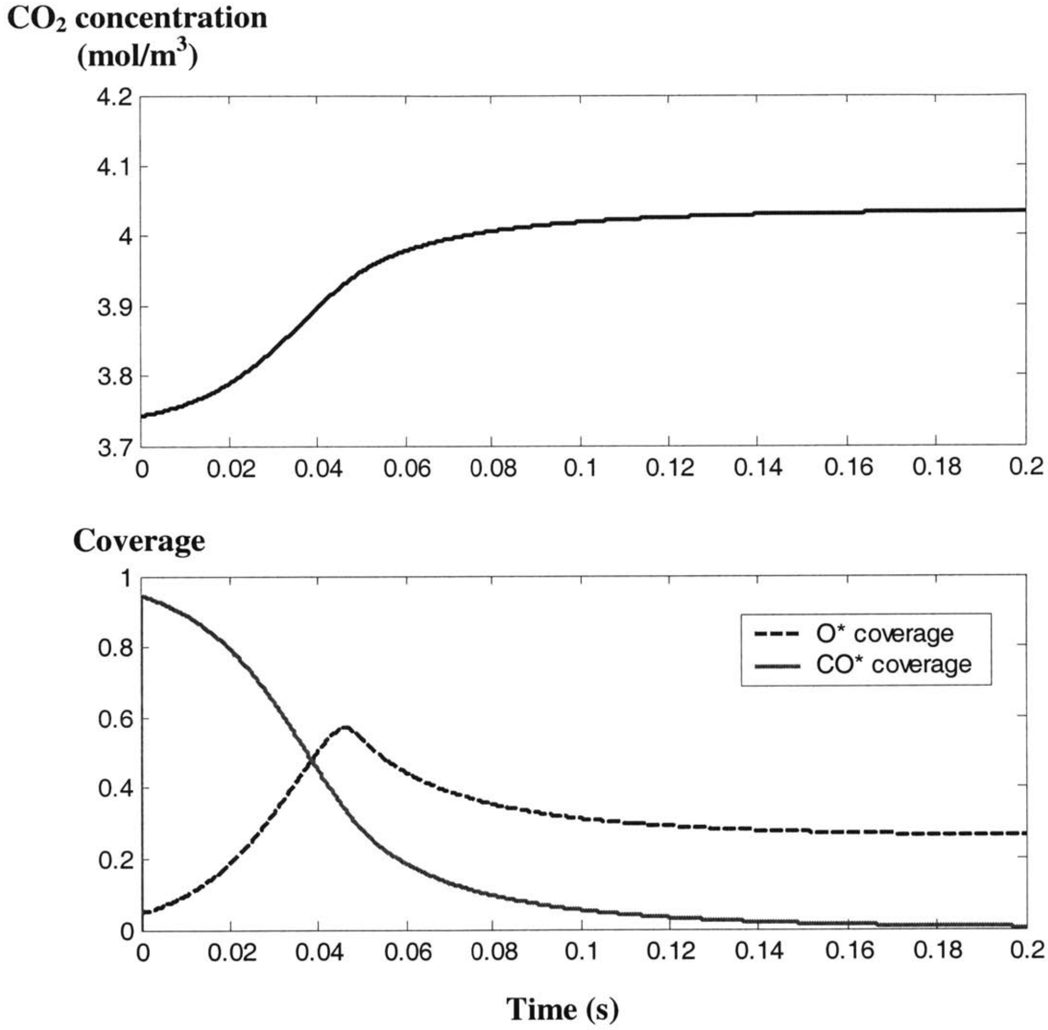

Fig. 5.1: *CO_2 production and adsorbate coverages in the CO-O_2 reaction at 450 K*

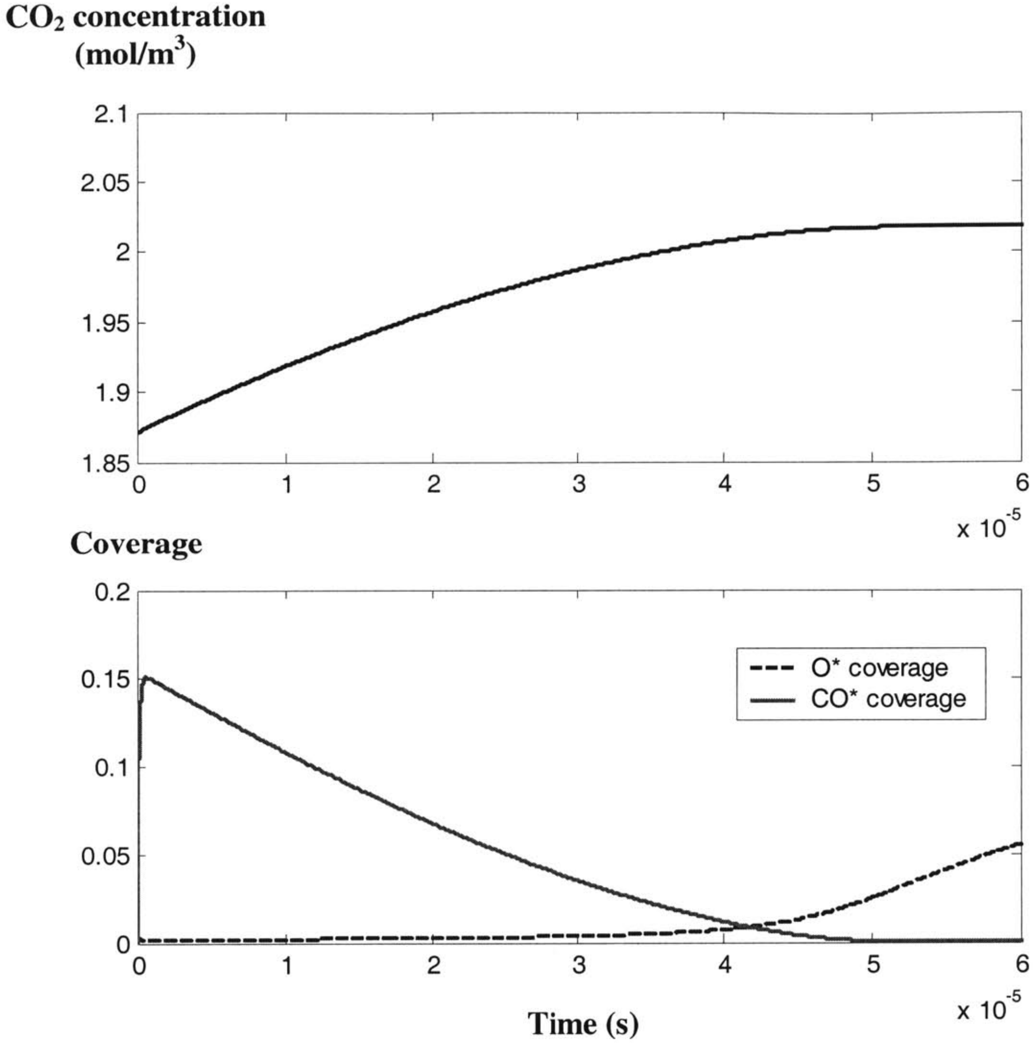

Fig. 5.2: *CO_2 production and adsorbate coverages in the CO-O_2 reaction at 900 K*

Global rate expressions do not traduce this change in kinetic regime. In fact, in most encountered models of catalytic converters, they are fitted for high temperature ranges and thus well reproduce the high temperature regime in which adsorption reactions are rate limiting. On the contrary, theoretically determined Langmuir-Hinshelwood rate expressions assume the adsorption reactions to be in equilibrium and one of the surface reactions (CO*-O* for the CO-O_2 mechanism) to be irreversible and rate limiting. Thus, they correspond to the low temperature regime.

5.2 Similar chemical behavior of the CO-O_2 and H_2-O_2 mechanisms

All the previous models of catalytic converters use the same global rate expressions for the CO-O_2 and H_2-O_2 mechanisms. For example, *Koltsakis et al* [9] use:

$$R_{CO-O_2} = \frac{k \cdot x_{CO} \cdot x_{O_2}}{\left(1 + K_1 \cdot x_{CO} + K_2 \cdot x_{C_3H_6}\right)^2 \cdot \left(1 + K_3 \cdot x_{CO}{}^2 \cdot x_{C_3H_6}{}^2\right) \cdot \left(1 + K_4 \cdot x_{NO}{}^{0.7}\right)}$$
$$R_{H_2-O_2} = \frac{k \cdot x_{H_2} \cdot x_{O_2}}{\left(1 + K_1 \cdot x_{CO} + K_2 \cdot x_{C_3H_6}\right)^2 \cdot \left(1 + K_3 \cdot x_{CO}{}^2 \cdot x_{C_3H_6}{}^2\right) \cdot \left(1 + K_4 \cdot x_{NO}{}^{0.7}\right)}$$

where x_i refers to the mole fraction of species i.

For mixtures containing only the reactants of the considered reaction, the two rates become:

$$R_{CO-O_2} = \frac{k \cdot x_{CO} \cdot x_{O_2}}{\left(1 + K_1 \cdot x_{CO}\right)^2}$$
$$R_{H_2-O_2} = k \cdot x_{H_2} \cdot x_{O_2}$$

Hence, the two rates only differ by the CO inhibition term in the rate expression for the CO-O_2 mechanism. On the other hand, the inhibition term becomes negligible at high temperatures as illustrated by *Koltsakis et al*'s expression $K_1 = 65.5 \cdot \exp\left(\frac{961}{T}\right)$. Therefore, we can expect the two rates to be the same at high temperatures, and/or at very low CO levels.

We checked for this behavior with the microkinetics mechanisms. In the simulation, we assumed the same initial level of CO and H_2, and compared the production of H_2O and CO_2. The H_2-O_2 mechanism was simulated with an initial mixture containing H_2 and O_2 only, and the CO-O_2 mechanism with an initial mixture containing CO and O_2 only. The initial levels of H_2O and CO_2 were set to 0.

As illustrated on Figure 5.3 (top curve), the two rates are indeed close to each other at high temperatures (T=900 K on the figure), especially at early times when the level of CO in the mixture decreases slowly. Moreover, the bottom curve on Figure 5.3 reveals that as the initial reactant level is reduced, the two rates become even closer, as expected.

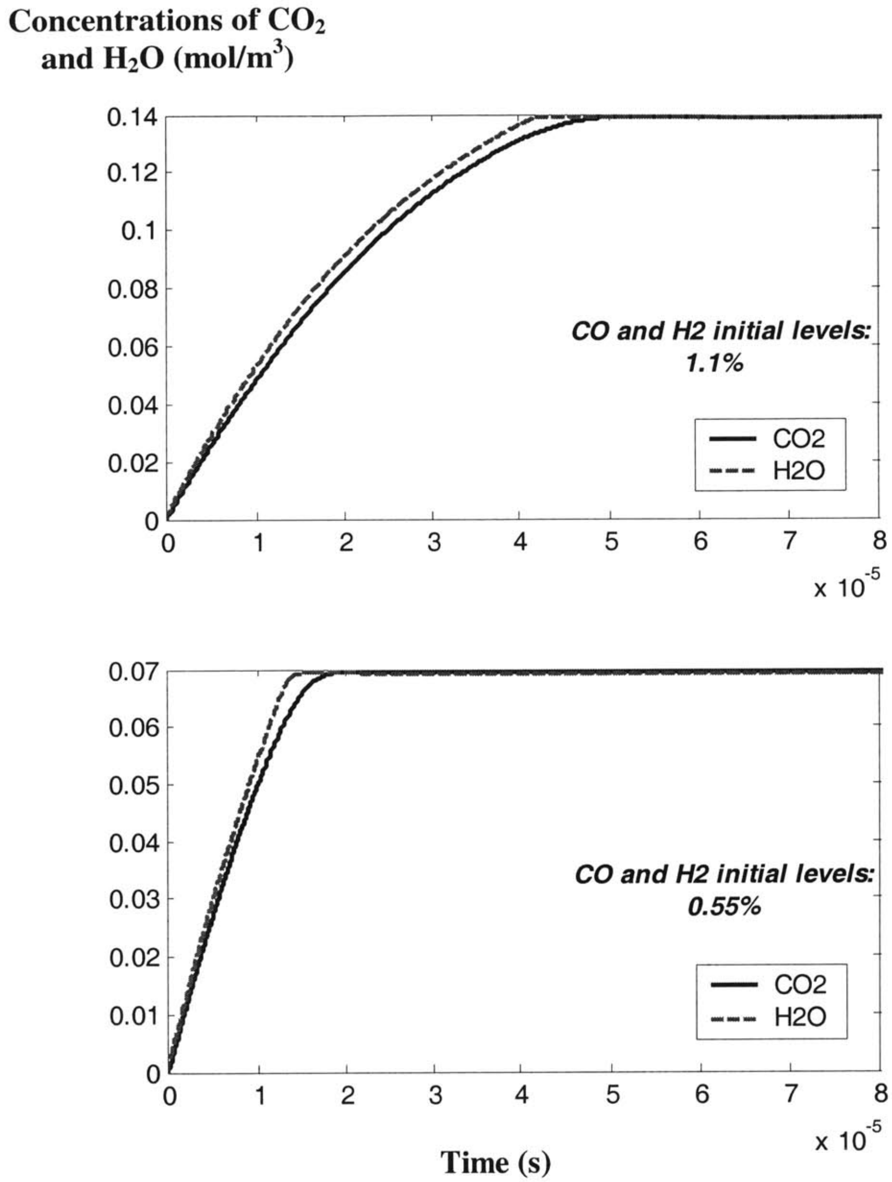

Fig. 5.3: *Evolution of the CO_2 and H_2O concentrations with time in the CO-O_2 and H_2-O_2 mechanisms for two CO and H_2 levels: 1.1% and 0.55% (T=900 K)*

5.3 H_2-O_2 mechanism

As explained in section 4.4.4 iii-, the microkinetics rate expressions for the H_2-O_2 mechanism predict a different steady state level than the global rate expression from *Koltsakis et al* (see Figure 4.20). Figure 5.4 below gives more explanations for the microkinetics equilibrium.

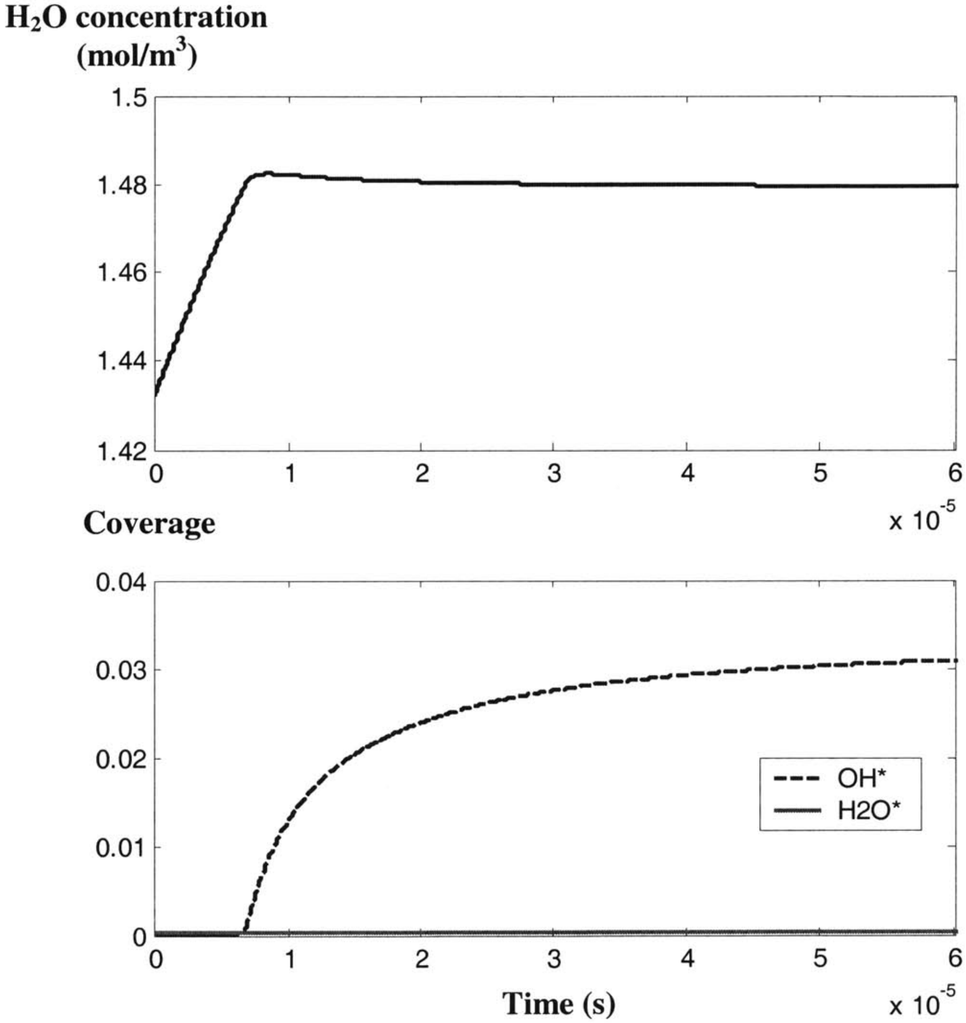

Fig. 5.4: *Evolution of the H_2O concentration and surface coverages with time in the H_2-O_2 mechanism at 840 K (H_2 level=0.37 %)*

As illustrated by the bottom curve, the new equilibrium corresponds to the equilibrium of OH* on the surface. Thus, as soon as the H_2-O_2 reaction is over (because one of the reactants is extinguished), some H_2O adsorb on the catalytic surface and undergo reverse reactions 16 and 17 to form OH*. The equilibrium constant of reaction 16 is then rapidly reached and OH* reaches the corresponding equilibrium concentration. Indeed, Figure 5.5 below plotted with a modified activation energy E_{Af16}=40 kJ/mol instead of the determined 63.2 kJ/mol reveals that reaction 16 is responsible for the predicted microkinetics equilibrium.

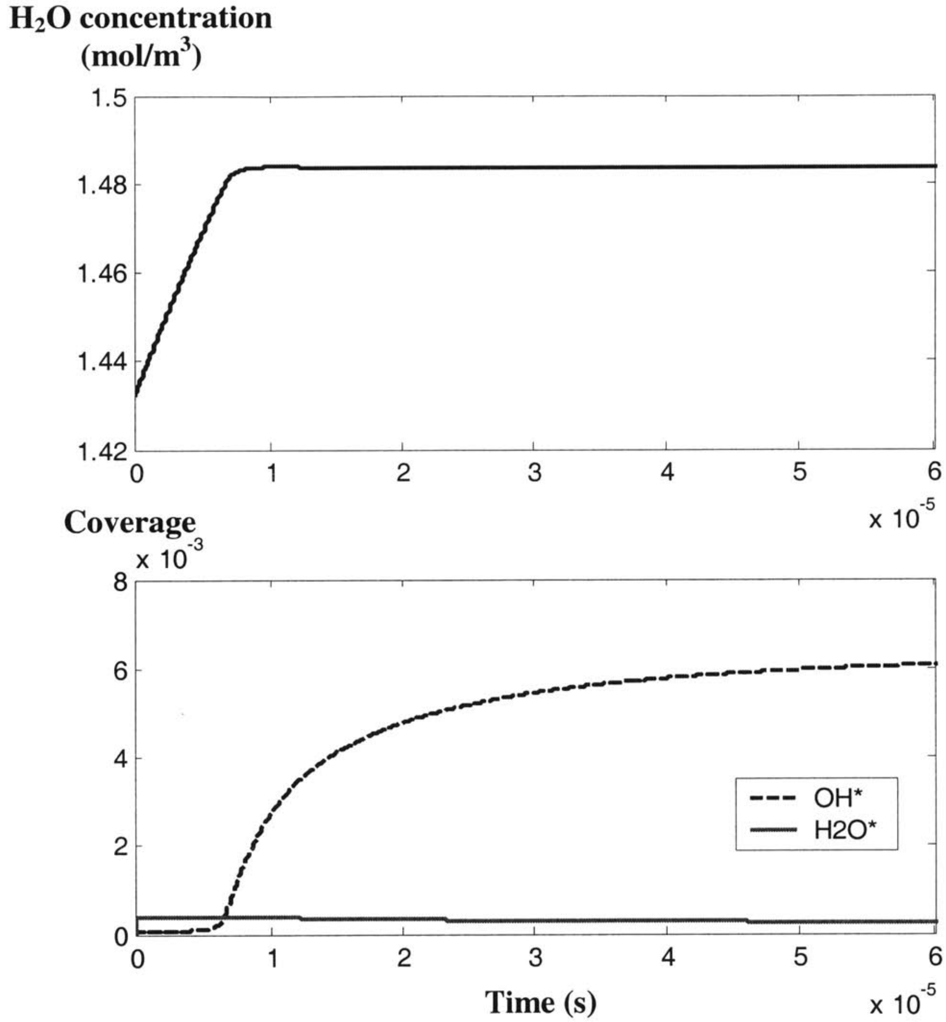

Fig. 5.5: *Evolution of the H_2O concentration and surface coverages with time in the H_2-O_2 mechanism at 840 K with modified E_{Af16} (H_2 level=0.37%)*

The global rate expressions lump all the details of the surface reactions in their expression and are thus not able to represent this behavior.

Chapter 6: Conclusions and future work

6.1 Conclusions

Based on a detailed review of the microscopic chemical processes occurring on the catalytic surface, we developed a one-dimensional microkinetics model for monolithic three-way catalytic converters. The model accounts for the internal and external transport processes and includes the oxidation of CO, H_2, C_3H_6, the reduction of NO by CO and H_2, the water-gas shift and the steam reforming reactions, as well as an oxygen storage submodel. We assembled the kinetic parameters for the corresponding 26 elementary reactions.

Even though the model was not entirely tested, part of the assembled kinetic parameters was validated by comparison of the microkinetics mechanisms to the global reactions (represented by the global rates of *Koltsakis et al* [9]). This comparison led to the following conclusions:

- *The tested microkinetics mechanisms show adequate kinetics.*

  Indeed, they predict comparable kinetics to the global rate expressions for mean operating temperatures (T about 800-900 K), temperatures for which the global rate expressions were experimentally fitted.
- *A microkinetics modeling of the chemical processes is essential to correctly represent the catalyst behavior on its whole range of operating temperatures.*

  All the global rate expressions used so far in previously developed models were experimentally fitted for mean operating temperatures or steady-state operation. Hence, they do not represent the catalytic behavior on the whole range of operating temperatures and especially fail at low temperatures. The oxygen storage submodel particularly highlighted this limitation.

Furthermore, we simulated the microkinetics mechanisms to study their qualitative behavior. This study had two objectives: check for the consistency of the mechanisms with known trends and identify new trends, not predicted by global rate expressions. This study led to the following conclusions:

- *The microkinetics mechanisms show good agreement with the known trends*
  In particular, the overall chemical process is limited by surface reactions at low temperatures and adsorption reactions at high temperatures.
- *A microkinetics model is essential to accurately predict the performance of the converter.*

  The microkinetics mechanisms for which the products are easily adsorbed lead to different equilibriums than the lumped global rate expressions (H_2-O_2 mechanism for example).

6.2 Future work

6.2.1 Model validation

The model requires further testing to be validated. In particular, the entire model can be numerically simulated using a one-dimensional code representing a monolith channel. The following series of numerical tests could be performed:

- Quasi-steady state simulation to check for the predicted conversion at mean operating temperatures
- Light-off tests to check for the predicted conversion during warm-up

The validation of the model then requires adequate experimental data to which the results of the simulations can be compared.

6.2.2 Further improvements to the model

The microkinetics modeling could be further improved by accounting for the oxidation of C_3H_8. Indeed, the slow-oxidizing hydrocarbons are responsible for global conversions of the hydrocarbons of the order of 97 % (100% conversion is achieved for C_3H_6).

The oxygen storage submodel could also be improved by accounting for the oxidation of ceria by H_2O and its reduction by H_2. Indeed, atomic hydrogen is a very active species, as illustrated in the review we made, and H_2 is thus the strongest ceria reducing agent. H_2O plays an important role in the water-gas shift and steam reforming reactions.

We principally focused our attention on the chemical processes to develop a detailed microkinetics model. To improve the global accuracy of the model, other processes could be more closely looked at:

- *Internal diffusion process*

  An internal transport submodel adapted to the set of elementary reactions needs to be developed to correctly evaluate the impact of internal diffusion on the overall heterogeneous process.

- *External diffusion process*

  The used Nusselt and Sherwood correlations could be improved by looking more closely into the behavior of the flow inside the monolith channels. In particular, accounting for the spatial dependence of these non-dimensional numbers would enable us to assess the impact of the entrance region on the performance of the converter.

Bibliography

[1] Otto, N.C. and LeGray, W.J., "Mathematical Models for Catalytic Converter Performance", *SAE paper 800841*, 1980.

[2] Oh, S.H. and Cavendish, J.C., "Transients of Monolithic Catalytic Converters: Response to Step Changes in Feedstream Temperature as Related to Controlling Automobile Emissions", *Ind. Eng. Chem. Prod. Res. Dev.*, 21, pp. 29-37, 1982.

[3] Chen, D.K.S., Bissett, E.J., Oh, S.H., and Van Ostrom, D.L., "A Three-Dimensional Model for the Analysis of Transient Thermal and Conversion Characteristics of Monolithic Catalytic Converters", *SAE paper 880282*, 1988.

[4] Voltz, S.E., Morgan, C.R., Liederman, D., and Jacob, S.M., "Kinetic Study of Carbon Monoxide and Propylene Oxidation on Platinum Catalysts", *Ind. Eng. Chem. Prod. Res. Dev.,* 12, No 4, pp. 294-301, 1973.

[5] Shamim, T., Shen, H., and Sengupta, S., "Comparison of Chemical Kinetic Mechanisms in Simulating the Emission Characteristics of Catalytic Converters", *SAE paper 2000-01-1953.*

[6] Montreuil, C.N., Williams, S.C., and Adamczyk, A.A., "Modeling Current Generation Catalytic Converters: Laboratory Experiments and Kinetic Parameter Optimization- Steady State Kinetics", *SAE paper 920096*, 1992.

[7] Pattas, K.N., Stamatelos, A.M., Pistikopoulos, P.K., Koltsakis, G.C., Konstandinis, P.A., Volpi, E., and Leveroni, E., "Transient modeling of Three-Way Catalytic Converters", *SAE paper 940934*, 1994.

[8] Brinkmeier, C., Eigenberger, G., Buchner, S., and Donnerstag, A., "Transient Emissions of a SULEV Catalytic Converter System Dynamic Simulation versus Dynamometer Measurements", *SAE paper 2003-01-1001.*

[9] Koltsakis, G.C., Konstandinis, P.A., and Stamatelos, A.M., "Development and Application Range of Mathematical Models for Three-Way Catalytic Converters", *Applied Catalysis B*, 12, pp. 161-191, 1997.

[10] Sriramulu, S., Moore, P.D., Mello, J.P., and Weber, R.S., "Microkinetics Modeling of Catalytic Converters", *SAE paper 2001-01-0936.*

[11] Ertl, G., Knozinger, H., and Weitkamp, J., *Environmental Catalysis*, 1999.

[12] Heck, R. and Farrauto, R.J., *Catalytic Air Pollution Control*, 1994.

[13] Cybulski, A. and Moulijn, J.A., "Monoliths in Heterogeneous Catalysis", *Catalysis reviews*, 36 (2), pp. 179-270, 1994.

[14] Yuetao Zhang, experimental data, Personal Communication.

[15] Ponec, V. and Bond, G.C., *Catalysis by metals and alloys, Studies in Surface Science and Catalysis*, 95, 1995.

[16] Powell, B.R. and Chen, Y.L., "Analytical Electron Microscopy of a Vehicle-Aged Automotive Catalyst", *Applied Catalysis*, 53, pp. 233-250, 1989.

[17] "Coadsorption, Promoters, and Poisons", *The Chemical Physics of Solid Surfaces*, volume 6, Chapter 6 , edited by King, D.A. and Woodruff, D.P., 1993.

[18] http://www.chem.qmw.ac.uk/surfaces/scc/scat2_4.htm, "PE Curves and Energetics of Adsorption".

[19] http://www.chem.qmw.ac.uk/surfaces/scc/scat2_5.htm, "Adsorbate Geometries and Structures on Metals"

[20] Hahn, J.R. and Ho, W., *Physical Review Letters*, 15, October 2001
or http://www.aip.org/mgr/png/2001/139.htm

[21] Grenoble, D.C. and Estadt, M.M., "The Chemistry and Catalysis of the Water Gas Shift Reaction. The Kinetics over Supported Metal Catalysts", *Journal of Catalysis*, 67, pp. 90-102, 1981.

[22] Martin, D. and Duprez, D., "Surface Migration of Oxygen and of Hydrogen in Supported Metal Catalysts", *New Aspects of Spillover, Effect in Catalysis, Studies in Surface Science and Catalysis*, 77, p. 201, Elsevier Science Publishers, 1993.

[23] Rozanov, V.V. and Krylov, O.V., "Hydrogen Spillover in Heterogeneous Catalysis", *Russian Chemical Reviews*, 66(2), pp. 107-119, 1997.

[24] Holmgren, A., "Catalyst for Car Exhaust: Oxygen Storage in Platinum/Ceria and Mass Transfer in Monoliths", PhD thesis, Chalmers University of Technology, Sweden, http://sune2.cre.chalmers.se/externt/anna/avh/avh3.pdf

[25] Li, C., Chen, Y., Li, W., and Xin, Q., "Spillover of Atomic Oxygen and Reverse Spillover of Dioxygen Species on Pt/CeO_2 Catalysts", *New aspects of spillover, Effect in Catalysis*, p. 217, Elsevier Science Publishers, 1993.

[26] Nunan, J.G., Robota, H.J., Cohn, M.J., and Bradley, S.A., "Physicochemical Properties of Ce-containing Three-Way Catalysts and the Effect of Ce on Catalyst Activity", *Journal of Catalysis*, 133, pp. 309-324, 1992.

[27] Yamada, T., Kayano, K., and Funabiki, M., "Platinum Metals-Ceria Synergism in Autoexhaust Catalysts", *New Aspects of Spillover, Effect in Catalysis, Studies in Surface Science and Catalysis*, 77, p. 329, Elsevier Science Publishers, 1993

[28] Masel, R.L., *Chemical Kinetics and Catalysis*, 2002.

[29] Guimaraes, A.L., Dieguez, L.C., and Schmal, M., "Effects of Ceria on Propane Reforming over Alumina Supported Palladium Catalysts", *Spillover and Mobility of Species on Solid Surfaces, Studies in Surface Science and Catalysis*, 138, p. 395, Elsevier Science Publishers, 2001.

[30] Oh, S.H., "Effects of Cerium Addition on the CO-NO Reaction Kinetics over Alumina-Supported Rhodium Catalysts", *Journal of Catalysis*, 124, pp. 477-487, 1990.

[31] Koltsakis, G.C. and Stamatelos, A.M., "Catalytic Automotive Aftertreatment", *Prog. Energy Comb. Sci.*, 23, pp. 1-39, Elsevier Science, 1997.

[32] Yuetao Zhang, Personal Communication.

[33] Kummer, J.T., "Catalysts for automobile emission control", *Prog. Energy Comb. Sci.*, 6, pp. 177-199, 1980.

[34] Punke, A., Dahle, U., Tauster, S.J., Rabinowitz, H.N., and Yamada, T., "Trimetallic Three-Way Catalysts", *SAE paper 950255*, 1995.

[35] http://lamar.colostate.edu/~rwu4451/massman/coef_diff.htm,
Massman, W., "Coefficients of molecular diffusivities"

[36] Carberry, J.J., *Chemical and Catalytic Reaction Engineering*, McGraw Hill Chemical Engineering Series, 1976.

[37] *Handbook of Heat and Mass Transfer*, vol. 2, Houston, Gulf Pub. Co., 1986.

[38] Satterfield, C.N., *Mass Transfer in Heterogeneous Catalysis*, Robert E. Krieger Publishing Company, New York, 1981.

[39] Hayes, R.E. and Kolaczkowski, S.T., "Mass and Heat Transfer Effects in Catalytic Monolith Reactors", *Chemical Engineering Science*, Vol.49 (21), pp. 3587-3599, 1994.

[40] Kuo, J.C.W., Morgan, C.R., and Lassen, H.G., "Mathematical modeling of CO and HC catalytic converter systems", *SAE paper 710289*, 1971.

[41] Cai, W. and Collings, N, "Mathematical models of the catalytic oxidation sensor and the monolith catalytic converter", October 30, 1991.

[42] Edvinsson, R.K. and Cybulski, A., "A Comparative Analysis of the Trickle-Bed and the Monolithic Reactor For Three-Phase Hydrogenations", *Chemical Engineering Science*, Vol. 49 (24B), pp. 5653-5666, 1994.

[43] Oh, S.H. and Cavendish, J.C., "Design Aspects of Poison-Resistant Automobile Monolith Catalysts", *Ind. Eng. Chem. Prod. Res. Dev.*, 22, pp. 509-518, 1983.

[44] Taylor, K.C., "Simultaneous NO and CO Conversion over Rhodium", *The Catalytic Chemistry of Nitrogen Oxides*, Plenum Press, New York, 1975.

[45] Yao, H.C., Sieg, M., and Plummer, H.K.Jr, "Surface Interactions in the Pt/γ-Al_2O_3 System", *Journal of Catalysis*, 59, pp. 365-374, 1979.

[46] Campbell, C.T., Ertl, G., Kuipers, H., and Segner J., "A Molecular Beam Study of the Adsorption and Desorption of Oxygen From a Pt(111) Surface", *Surface Science*, 107, pp. 220-236, 1981.

[47] Anton, A.B. and Cadogan, D.C., "The Mechanism and Kinetics of Water Formation on Pt(111)", *Surface Science Letters*, 239, L548-L560, North-Holland, 1990.

[48] Williams, W.R., Marks, C.M., and Schmidt, L.D., "Steps in the Reaction $H_2 + O_2 \leftrightarrow H_2O$ on Pt: OH Desorption at High Temperatures", *J. Phys. Chem.*, 96, pp. 5922-5931, 1992.

[49] Schwartz, A, Holbrook, L.L., and Wise, H, "Catalytic Oxidation Studies with Platinum and Palladium", *Journal of Catalysis*, 21, pp. 199-207, 1971.

[50] Gorte, R. and Gland, J.L., "Nitric oxide adsorption on the Pt(110) surface", *Surface Science*, 102, pp. 348-358, 1981.

[51] Hirano, H., Yamada, T., Tanaka, K.I., Siera, J., Cobden, P., and Nieuwenhuys, B.E., "Nitric Oxide Reduction Reactions on $Pt_{0.25}$-$Rh_{0.75}$ (100)", *Surface Science*, 262, pp. 97-112, 1992.

[52] Shido, T. and Iwasawa, Y., "Reactant-Promoted Reaction Mechanism for the Water-Gas Shift Reaction on Rh-doped CeO_2", *Journal of Catalysis*, 141, p. 71, 1993.

[53] *Catalysis, Science and Technology*, ed. by Anderson, J.R and Boudart, M., Berlin, New York, Springer-Verlag, 1981-1996.

[54] Grenoble, D.C., "The Chemistry and Catalysis of the Water/Toluene Reaction", *Journal of Catalysis*, 51, pp. 212-220, 1978.

[55] Duprez, D., Pereira, P., Miloudi, A., and Maurel, R., "Steam dealkylation of aromatic hydrocarbons", *Journal of Catalysis*, 75, pp. 175-163, 1982.

[56] Dumesic, J.A., Rudd, D.F., Aparicio, L.M., Rekoske, J.E., and Trevino, A.A., *The Microkinetics of Heterogeneous Catalysis*, The American Chemical Society, 1993.

[57] Holmgren, A. and Andersson, B., "Oxygen Storage Dynamics in $Pt/CeO_2/Al_2O_3$ Catalysts", *Journal of Catalysis*, 178, pp. 14-25, 1998.

[58] Engel, T. and Ertl, G., "Elementary Steps in the Catalytic Oxidation of Carbon Monoxide on Platinum Metals", *Advances in Catalysis*, 28, p. 1, 1979.

[59] http://firebrand.me.berkeley.edu/cpchou/catalysis/surf.html, "Surface Reaction Mechanism of Methane Oxidation on Platinum"

[60] Chase, M.W., *NIST-JANAF Thermochemical Tables*, *Journal of Physical and Chemical Reference Data*, Monograph No 9, 1998.

[61] Barin, I., *Thermochemical data of pure substances*, Third Edition, 1995.

[62] Yeo, Y.Y., Vattuone, L., and King, D.A., "Calorimetric Heats for CO and Oxygen Adsorption and for the Catalytic CO Oxidation Reaction on Pt(111)", *J. Chem. Phys.*, 106 (1), pp. 392-401, January 1997.

[63] Kwasniewski, V.J. and Schmidt, L.D., "Steps in the Reaction $H_2 + O_2 \leftrightarrow H_2O$ on Pt(111): Laser-Induced Thermal Desorption at Low Temperature", *J. Phys. Chem*, 96, pp. 5931-5938, 1992.

[64] Fink, Th, Dath, J.P., Bassett, M.R., Imbihl, R., and Ertl, G., "The Mechanism of the "explosive" NO+CO Reaction on Pt(100): Experiments and Mathematical Modeling", *Surface Science*, 245, pp. 96-110, 1991.

[65] Zeppenfeld, P., David, R., Ramseyer, C., Girardet, C., and Hoang, P.N.M., "Adsorption and structure of N_2 on Pt(111)", *Surface Science*, 444, p. 163, 2000.

[66] Ovesen, C.V., Stoltze, P., Norskov, J.K., and Campbell, C.T., "A Kinetic Model of the Water Gas Shift Reaction", *Journal of Catalysis*, 134, pp. 445-468, 1992.

[67] Ovesen, C.V., Clausen, B.S., Hammershoi, Steffensen, G., Askgaard, T. Chorkendoff, I., Norskov, J.K., Rasmussen, P.B., Stoltze, P., and Taylor, P.A., "A Microkinetics Analysis of the Water-Gas Shift Reaction under Industrial Conditions", *Journal of Catalysis*, 158, pp. 170-180, 1996.

[68] Hei, M.J., Chen, H.B., Yi, J. Lin, Y.J., Lin, Y.Z., Wei, G., and Liao, D.W., "CO_2 reforming of methane on transition metal surfaces", *Surface Science*, 417, pp. 82-96, 1998.

[69] Herz, R.K., "Dynamic Behavior of Automotive Catalysts. 1. Catalyst Oxidation and Reduction", *Ind. Eng. Chem. Prod. Res. Dev.*, 20, pp. 451-457, 1981.

[70] Frennet, A. and Bastin, J.M., "How a Three-Way Catalyst is Affected under Transient Conditions: A Study of Pt-Rh/Al_2O_3 Catalyst", *Catalysis and Automotive Pollution Control III, Studies in Surface Science and Catalysis*, 96, Elsevier Science, 1995.

Appendix A: Computation of the characteristic times of the transport and chemical processes for CO oxidation

A.1 External transport

As explained in Chapter 4, CO is the slowest diffusing species between CO and O_2 and thus limits the external diffusion process. The CO molecular diffusivity in N_2 (dominant species in the monolith mixture) is given by: $D_{m,CO} = 0.1804 \cdot 10^{-4} \cdot \frac{P_o}{P} \cdot \left(\frac{T}{T_o}\right)^{1.81}$ [35], where P_o and T_o are the standard pressure and temperature, respectively, and with $D_{m,CO}$ in m^2/s. The pressure P was taken as the standard pressure.

As said in Chapter 2, a typical monolith channel is about 1 to 2 mm in diameter; we assumed d=1.5 mm in the calculations.

Thus, at 1000 K, the external transport characteristic time for CO is 3.5 ms.

A.2 Internal transport

A.2.1 Effective diffusivity

As said in chapter 4, the effective diffusivity depends on the pore diameter and structure. Indeed, the pore diameter defines two main diffusing zones [36]:

- The Knudsen diffusion region, for pore diameters less than the mean free path. In this region, the effective diffusivity is given by (in m^2/s):

$$D_{K,eff} = 1.94 \cdot \frac{\nu^2}{\tau \cdot S_g \cdot \rho_p} \cdot \sqrt{\frac{T}{M}}$$

Where: ν is the porosity of the pores of the washcoat under consideration

τ is the tortuosity factor characterizing the pore shape

ρ_p is the density of the porous material in g/cm^3

S_g is the total surface of the porous material in cm^2/g
M is the molecular weight of the diffusing species in g/mol
T is the temperature in K.

- The ordinary diffusion region or continuum region, for pore diameters greater than the mean free path. In this region, the effective diffusivity is computed from $D_{m,eff} = \frac{D_m \cdot \nu}{\tau}$, where D_m is the molecular diffusivity of the diffusing species.

The limit between the two regimes is usually considered at a pore-radius-to-mean-free-path-ratio of 1.

In fact, the two above regions are separated by a transition region which prevails for a pore-radius-to-mean-free-path ratio ranging from 0.1 to 10 [37]. In this transition region, the effective diffusivity can be computed from both the Knudsen and ordinary effective diffusivities as follows:

$$\frac{1}{D_{eff}} = \frac{1}{D_{K,eff}} + \frac{1}{D_{m,eff}} \tag{A.1}$$

A.2.2 Time calculations

For the calculations, a bimodal micro-macro pore distribution was assumed. The percentage of pore volume contributed by the micropores is usually larger than that by the macropores [37, 38]. Indeed, at the peak of the micropores distribution, the cumulative volume is about 60-70 % of the total pore volume; the pore diameter is less than 150 angstroms at this point. These numbers correspond to pelleted catalysts. However, they are also representative of porous catalyst structures in general, including the material used in monolithic catalysts. In our time scale calculations, we chose a bimodal pore volume distribution with a peak at 100 angstroms and one at 3000 angstroms. This distribution is shown on Figure A.1 below.

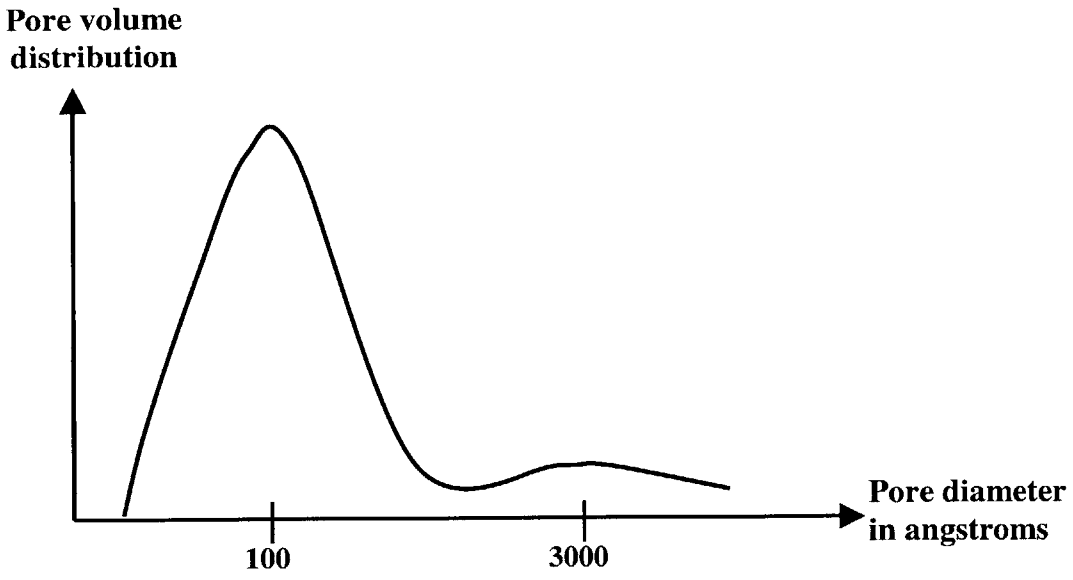

Fig. A.1: *Assumed typical bimodal pore distribution*

i- Effective diffusivity

The mean free path for a molecule of diameter d is $\text{MFP} = \dfrac{R_g.T}{\sqrt{2}\cdot\pi\cdot d^2\cdot N_A\cdot P}$, where R_g is the universal gas constant, N_A Avogadro's number, and P the operating pressure. Hence, for CO, $\text{MFP (m)} = 1.72\cdot10^{-10}.\text{T (K)}$. Thus, at 300 K, the assumption of a continuum is justified for pore radii greater than MFP=517 angstroms. We can see from the bimodal pore distribution presented in Figure A.1 that this condition is not satisfied for all pores.

The time across the pores was computed for the 3000 angstroms diameter macropores. These pores are in the continuum region, and the effective diffusivity can thus be calculated from the molecular diffusivity.

The choice of the pore size for the "time-along-the-pore" calculations was more difficult. Since about 70% of the total pore volume corresponds to micropores operating in the Knudsen diffusion regime or in the transition regime, we chose to compute the effective diffusivity by the general formula (A.1). We assumed a total surface of the porous material of 10^6 cm^2/g and a density of the porous material of 1.616 g/cm^3 [9].

In these calculations, we assumed a washcoat porosity of 0.7 and a tortuosity factor of 3.7 ([37], [38]).

ii- Characteristic time across the pore

The macroscopic pores have the largest diameter and thus limit the diffusion across the pores. Hence, the characteristic time across the pore was computed for the pores of 3000 angstroms in diameter.

Thus, the characteristic time across the pores at 1000 K is $2.95.10^{-15}$ s.

iii- Characteristic time along the pore

A pore length of 100 μm was used. By considering the largest possible length as the typical thickness of the washcoat in the corners of square channels, we neglected the possibility of highly tortuous pores.

Thus, the characteristic time along the pores at 1000 K is 10.8 ms.

A.3 Catalytic reactions

A.3.1 Characteristic time for the adsorption of O_2

Due to adsorption, the concentration of O_2 decreases according to the following partial differential equation $\frac{d[O_2]}{dt} = -k_{f1} \cdot [O_2] \cdot [S]^2$.

By conservation of mass, the concentration of vacant sites [S] can also be written: $[S] = [S]_0 - [O^*] - [CO^*]$.

Thus, $\frac{d[O_2]}{dt} = -k_{f1} \cdot [O_2] \cdot ([S]_0 - [O^*] - [CO^*])^2$.

Hence, at early times, the equation becomes $\frac{d[O_2]}{dt} = -k_{f1} \cdot [O_2] \cdot [S]_0{}^2$, and the characteristic time constant for O_2 adsorption is $\tau_{ads} = \frac{1}{k_{f_1}.[S]_0{}^2}$.

A.3.2 Time scale for the CO- O* surface reaction*

The equilibrium constants of the adsorption of O_2 and CO were computed from their forward and reverse kinetic constants (see section 4.4.4) as follows: $K_i = \frac{k_{fi}}{k_{ri}}$ (i=1 for O_2 adsorption and i=2 for CO adsorption). On the other hand, the equilibrium constants are linked to the concentrations of the reactants by: $K_1 = \frac{[O^*]^2}{[O_2]\cdot[S]^2}$ and $K_2 = \frac{[CO^*]}{[CO]\cdot[S]}$, where [S] is the concentration of available sites on the surface.

Or, introducing the partial coverages of the surface (see section 4.4.3):

$$K_1 = \frac{\theta_O^{*2}}{[O_2]\cdot(1-\theta_O^* - \theta_{CO}^*)^2} \tag{A.2}$$

$$K_2 = \frac{\theta_{CO}^*}{[CO]\cdot(1-\theta_O^* - \theta_{CO}^*)} \tag{A.3}$$

Knowing the values of K_1 and K_2, equations (A.2) and (A.3) can be solved to find the equilibrium partial coverages of O* and CO*:

$$\theta_O^* = \frac{\sqrt{K_1\cdot[O_2]}}{1+\sqrt{K_1\cdot[O_2]}+K_2.[CO]}$$

$$\theta_{CO}^* = \theta_O^* \cdot \frac{K_2.[CO]}{\sqrt{K_1\cdot[O_2]}}$$

In these calculations, we assumed stoichiometric concentrations of CO and O_2 with a percentage level of CO of 0.01%.

From the calculations, the coverage of CO* appears smaller than the coverage of O*. The time scale for the CO*-O* reaction was thus computed as: $\tau = \frac{1}{k_{f_3}.[CO^*]}$. The total concentration of catalytic sites was taken as $[S]_0=1.56.10^{-8}$ mol/m^2 (see section 4.4.4 ii-c).

The results of the calculations are summarized in Table A.1.

Table A.1: *Characteristic times of the transport and chemical processes at different temperatures*

T	External transport time (s)	Time along the pores (s)	Time across the pores (s)	Time for CO adsorption (s)	Time for O_2 adsorption (s)	Surface reaction time (based on CO*) (s)	Surface reaction time (based on O*) (s)	Reaction time (s)
300	0.030805479	0.022110767	2.60526E-14	6.08096E-07	8.53751E-06	255075.1851	8870.141145	255075.1851
320	0.027409175	0.021181433	2.31803E-14	5.88787E-07	9.09904E-06	25717.69597	700.8383304	25717.69597
340	0.024560692	0.020358242	2.07713E-14	5.71207E-07	9.66012E-06	3394.7895	74.7423314	3394.7895
360	0.022146745	0.019622846	1.87298E-14	5.55114E-07	1.02208E-05	560.7534331	10.23026746	560.7534331
380	0.0200821	0.01896097	1.69837E-14	5.40308E-07	1.0781E-05	111.8573569	1.727274697	111.8573569
400	0.018301591	0.018361338	1.54779E-14	5.26627E-07	1.13409E-05	26.19188702	0.348539135	26.19188702
420	0.016754683	0.017814917	1.41697E-14	5.13935E-07	1.19004E-05	7.03590235	0.081932557	7.03590235
440	0.01540168	0.017314383	1.30254E-14	5.02119E-07	1.24595E-05	2.128067511	0.021973849	2.128067511
460	0.014211037	0.01685373	1.20185E-14	4.91082E-07	1.30183E-05	0.713586128	0.00660869	0.713586128
480	0.013157422	0.016427985	1.11274E-14	4.80742E-07	1.35768E-05	0.261883643	0.002197109	0.261883643
500	0.012220296	0.016032992	1.03349E-14	4.71029E-07	1.4135E-05	0.104057604	0.000797779	0.104057604
520	0.01138286	0.01566525	9.62665E-15	4.61882E-07	1.46929E-05	0.044357689	0.000313173	0.044357689
540	0.01063126	0.015321784	8.99101E-15	4.53248E-07	1.52505E-05	0.020128389	0.000131761	0.020128389
550	0.010283974	0.015158345	8.6973E-15	4.49109E-07	1.55293E-05	0.013851136	8.75082E-05	0.013851136
560	0.009953988	0.015000052	8.41823E-15	4.45081E-07	1.58079E-05	0.009658133	5.89742E-05	0.009658133
580	0.009341417	0.014697868	7.90017E-15	4.3734E-07	1.6365E-05	0.004872151	2.79016E-05	0.004872151
600	0.008785443	0.014413338	7.42997E-15	4.29989E-07	1.69219E-05	0.002571132	1.38764E-05	0.002571132
620	0.008279202	0.014144813	7.00184E-15	4.22997E-07	1.74785E-05	0.001413242	7.21943E-06	0.001413242
640	0.007816848	0.013890852	6.61082E-15	4.16335E-07	1.80348E-05	0.000806021	3.91269E-06	0.000806021
660	0.007393378	0.013650187	6.25269E-15	4.09979E-07	1.8591E-05	0.000475403	2.2008E-06	0.000475403
680	0.007004486	0.013421701	5.92379E-15	4.03904E-07	1.91469E-05	0.000289125	1.28055E-06	0.000289125
700	0.006646454	0.0132044	5.621E-15	3.98093E-07	1.97026E-05	0.000180837	7.6854E-07	0.000180837
720	0.006316051	0.012997402	5.34157E-15	3.92525E-07	2.02582E-05	0.000116054	4.74544E-07	0.000116054
740	0.006010464	0.012799918	5.08314E-15	3.87184E-07	2.08135E-05	7.6264E-05	3.00772E-07	7.6264E-05

T	**External transport time (s)**	**Time along the pores (s)**	**Time across the pores (s)**	**Time for CO adsorption (s)**	**Time for O_2 adsorption (s)**	**Surface reaction time (based on CO*) (s)**	**Surface reaction time (based on O*) (s)**	**Reaction time (s)**
760	0.005727233	0.012611242	4.8436E-15	3.82055E-07	2.13686E-05	5.12236E-05	1.95286E-07	5.12236E-05
780	0.005464195	0.012430737	4.62115E-15	3.77125E-07	2.19235E-05	3.51084E-05	1.29656E-07	3.51084E-05
800	0.005219448	0.012257829	4.41416E-15	3.72382E-07	2.24783E-05	2.45199E-05	8.78841E-08	2.45199E-05
820	0.004991308	0.012092001	4.22122E-15	3.67812E-07	2.30328E-05	1.74281E-05	6.07315E-08	2.30328E-05
840	0.004778284	0.011932781	4.04106E-15	3.63407E-07	2.35872E-05	1.25928E-05	4.27336E-08	2.35872E-05
860	0.004579048	0.011779742	3.87257E-15	3.59157E-07	2.41414E-05	9.24128E-06	3.05853E-08	2.41414E-05
880	0.004392419	0.011632492	3.71473E-15	3.55052E-07	2.46955E-05	6.88221E-06	2.22459E-08	2.46955E-05
900	0.004217339	0.011490676	3.56666E-15	3.51085E-07	2.52493E-05	5.19794E-06	1.64309E-08	2.52493E-05
920	0.004052859	0.011353966	3.42756E-15	3.47248E-07	2.58031E-05	3.97947E-06	1.23164E-08	2.58031E-05
940	0.003898127	0.011222063	3.2967E-15	3.43534E-07	2.63566E-05	3.08713E-06	9.3656E-09	2.63566E-05
960	0.003752377	0.011094691	3.17344E-15	3.39936E-07	2.691E-05	2.42623E-06	7.22253E-09	2.691E-05
980	0.003614916	0.010971596	3.05719E-15	3.3645E-07	2.74633E-05	1.93164E-06	5.64791E-09	2.74633E-05
1000	0.003485118	0.010852543	2.94741E-15	3.33068E-07	2.80164E-05	1.558E-06	4.47851E-09	2.80164E-05
1020	0.003362413	0.010737315	2.84364E-15	3.29787E-07	2.85694E-05	1.27332E-06	3.60148E-09	2.85694E-05
1040	0.003246288	0.010625712	2.74543E-15	3.266E-07	2.91222E-05	1.05477E-06	2.93784E-09	2.91222E-05
1060	0.003136273	0.010517545	2.65239E-15	3.23504E-07	2.96749E-05	8.85867E-07	2.43163E-09	2.96749E-05